


2013

# The development of optical microscopy techniques for the advancement of single-particle studies

Kyle Marchuk  
*Iowa State University*

Follow this and additional works at: <https://lib.dr.iastate.edu/etd>

 Part of the [Chemistry Commons](#), and the [Nanoscience and Nanotechnology Commons](#)

## Recommended Citation

Marchuk, Kyle, "The development of optical microscopy techniques for the advancement of single-particle studies" (2013). *Graduate Theses and Dissertations*. 13275.  
<https://lib.dr.iastate.edu/etd/13275>

This Dissertation is brought to you for free and open access by the Iowa State University Capstones, Theses and Dissertations at Iowa State University Digital Repository. It has been accepted for inclusion in Graduate Theses and Dissertations by an authorized administrator of Iowa State University Digital Repository. For more information, please contact [digirep@iastate.edu](mailto:digirep@iastate.edu).

**The development of optical microscopy techniques for the advancement of single-particle studies**

by

**Kyle Marchuk**

A dissertation submitted to the graduate faculty in  
partial fulfillment of the requirements for the degree  
of  
DOCTOR OF PHILOSOPHY

Major: Analytical Chemistry

Program of Study Committee:

Ning Fang, Major Professor

Javier Vela

Emily Smith

Robert S. Houk

Edward Yu

Iowa State University

Ames, Iowa

2013

Copyright © Kyle Marchuk, 2013. All rights reserved.

## TABLE OF CONTENTS

ABSTRACT.....	v
CHAPTER 1: GENERAL INTRODUCTION .....	1
Dissertation Organization .....	1
Introduction.....	2
Recent Advances in Instrumentation .....	3
Recent Applications in Membrane Studies and Plant Cell Imaging.....	7
Total Internal Reflection Scattering Microscopy.....	9
Differential Interference Contrast Microscopy .....	10
Dissertation Focus.....	11
References.....	13
Figures.....	18
CHAPTER 2: HIGH-PRECISION TRACKING WITH NON-BLINKING QUANTUM DOTS RESOLVES NANOSCALE VERTICAL DISPLACEMENT .....	21
Abstract.....	21
Introduction.....	21
Results and Discussion .....	23
Conclusion .....	26
Methods.....	26
References.....	32
Figures.....	35
CHAPTER 3: THREE-DIMENSIONAL HIGH-RESOLUTION ROTATIONAL TRACKING WITH SUPER-LOCALIZATION REVEALS CONFORMATIONS OF SURFACE-BOUND ANISOTROPIC NANOPARTICLES.....	42
Abstract.....	42

Introduction.....	42
Results and Discussion .....	44
Conclusion .....	48
Methods.....	48
References.....	51
Figures.....	53
<b>CHAPTER 4: THREE-DIMENSIONAL ORIENTATION DETERMINATION OF STATIONARY ANISOTROPIC NANOPARTICLES WITH SUB-DEGREE UNCERTAINTY UNDER TOTAL INTERNAL REFLECTION SCATTERING MICROSCOPY.....</b>	
Abstract.....	66
Introduction.....	66
Results and Discussion .....	67
Conclusion .....	71
Acknowledgements.....	71
Methods.....	72
References.....	76
Figures.....	79
<b>CHAPTER 5: LASER NOMARSKI DIFFERENTIAL INTERFERENCE CONTRAST MICROSCOPY FOR THE INVESTIGATION OF NANOPARTICLES AND NANOSTRUCTURES ON REFLECTIVE SURFACES .....</b>	
Abstract.....	89
Introduction.....	89
Results and Discussion .....	91
Conclusions.....	96
References.....	96

Figures.....	100
CHAPTER 6: GENERAL CONCLUSIONS.....	105
Future Work.....	106
ACKNOWLEDGEMENTS.....	108

## ABSTRACT

Single particle orientation and rotational tracking (SPORT) has recently become a powerful optical microscopy tool that can expose many molecular motions. Unfortunately, there is not yet a single microscopy technique that can decipher all particle motions in all environmental conditions, thus there are limitations to current technologies. Within, the two powerful microscopy tools of total internal reflection and interferometry are advanced to determine the position, orientation, and optical properties of metallic nanoparticles in a variety of environments.

Total internal reflection is an optical phenomenon that has been applied to microscopy to produce either fluorescent or scattered light. The non-invasive far-field imaging technique is coupled with a near-field illumination scheme that allows for better axial resolution than confocal microscopy and epi-fluorescence microscopy. By controlling the incident illumination angle using total internal reflection fluorescence (TIRF) microscopy, a new type of imaging probe called “non-blinking” quantum dots (NBQDs) were super-localized in the axial direction to sub-10-nm precision. These particles were also used to study the rotational motion of microtubules being propelled by the motor protein kinesin across the substrate surface.

The same instrument was modified to function under total internal reflection scattering (TIRS) microscopy to study metallic anisotropic nanoparticles and their dynamic interactions with synthetic lipid bilayers. Utilizing two illumination lasers with opposite polarization directions at wavelengths corresponding to the short and long axis surface plasmon resonance (SPR) of the nanoparticles, both the in-plane and out-of-plane movements of many particles could be tracked simultaneously. When combined with Gaussian point spread function (PSF) fitting for particle super-localization, the binding status and rotational movement could be resolved without degeneracy.

TIRS microscopy was also used to find the 3D orientation of stationary metallic anisotropic nanoparticles utilizing only long-axis SPR enhancement. The polarization direction of the illuminating light was rotated causing the relative intensity of p-polarized and s-polarized light within the evanescent field to change. The interaction of the evanescent field with the particles is dependent on the orientation of the particle producing an intensity curve. This curve

and the in-plane angle can be compared with simulations to accurately determine the 3D orientation.

Differential interference contrast (DIC) microscopy is another non-invasive far-field technique based upon interferometry that does not rely on staining or other contrast enhancing techniques. In addition, high numerical aperture condensers and objectives can be used to give a very narrow depth of field allowing for the optical tomography of samples, which makes it an ideal candidate to study biological systems. DIC microscopy has also proven itself in determining the orientation of gold nanorods in both engineered environments and within cells.

Many types of nanoparticles and nanostructures have been synthesized using lithographic techniques on silicon wafer substrates. Traditionally, reflective mode DIC microscopes have been developed and applied to the topographical study of reflective substrates and the imaging of chips on silicon wafers. Herein, a laser-illuminated reflected-mode DIC was developed for studying nanoparticles on reflective surfaces.

## CHAPTER 1: GENERAL INTRODUCTION

### Dissertation Organization

This dissertation is organized in a manner similar to a scientific peer-reviewed journal article. There is an introduction of the pertinent background followed by the scientific investigations and the resulting conclusions. Within each chapter are the necessary cited literature, figures, and tables.

The first chapter is a general introduction that gives a brief overview of microscope development followed by the introduction of the three optical microscope configurations used for the majority of the research presented within. These configurations include total internal reflection fluorescence (TIRF) microscopy, total internal reflection scattering (TIRS) microscopy, and differential interference contrast (DIC) microscopy.

The second chapter describes the integration of a new type of fluorescent probe into super-localization and high-precision tracking through optical microscopy. The probe is used to investigate the high interest motor protein kinesin within a microtubule gliding assay.

Chapter three is dedicated to the introduction of a new optical microscopy technique that can track the dynamic three-dimensional (3D) rotational movement of anisotropic nanoparticles while simultaneously super-localizing their lateral position. Gold nanorods were studied interacting with a phospholipid bilayer surface.

The determination of the 3D orientation for stationary anisotropic nanoparticles using TIRS microscopy is described in Chapter 4. Instead of using two-color illumination with opposing polarizations, a single wavelength technique is explored.

The description of a bench top laser-illuminated reflected-mode DIC can be found in chapter five. Nanoparticles and nanostructures on reflective surfaces were imaged giving insight into lithographic modes for nanoparticle synthesis. The system is also capable of long-term observation for dynamic processes.

The final chapter summarizes the content of the thesis and provides insight into possible avenues for future research.



## Introduction

Of the five senses humans perceive, sight is often heralded as the most magnificent; the one we would last like to live without. With our eyes we are able to observe our surroundings, and with those observations we can start to investigate natural phenomena. From birth our natural instincts are to start making sense of the universe we live in. This starts with the most basic observations; what is around the corner, what is outside this room? Eventually our curiosity leads us to peering up into space straining to see the farthest out we can, or staring down into our world, squinting trying to resolve the most detail we can. Though they are amazing products of evolution, our eyes have significant limitations.

Our eyes are limited to detecting a very small region of the electromagnetic spectrum we called the “visible region” consisting of the wavelengths between 400 nm and 700 nm. To overcome this limitation we developed sensors to collect information outside this region that can translate it into something we can comprehend. We are also limited on our ability to resolve objects that are far away and very small. For this limitation we have developed optics to aid us such as telescopes and microscopes.

Although there are three main modern types of microscopy (optical,<sup>1</sup> electron,<sup>2</sup> and scanning probe microscopy<sup>3</sup>), optical microscopy is what commonly comes to mind first. The invention of the first compound microscope (consisting of two or more lenses) has some controversy surrounding it, but is generally given to Zacharias Janssen (1580-1638) of the Netherlands around the year of 1595.<sup>4</sup>

Early microscopes suffered from two significant limitations typically referred to as aberrations.<sup>5</sup> The first is what is called the spherical aberration, which results from the axial and peripheral rays having different focal planes. The second is chromatic aberration, which is due to the extent of refraction from different wavelengths of light. Both of these aberrations result in the blurring of the image and the loss of resolution.

It was not until the German mechanic Carl Zeiss (1816-1888) started producing microscopes in the late 19<sup>th</sup> century that these limitations were overcome.<sup>5</sup> At the time, producing quality optics was performed by trial and error. To establish a more reliable method, Carl Zeiss employed the mathematician and physicist Ernst Abbe who eventually came up with the original formula for the calculation of the maximal resolution achievable from an optical microscope. The formula for resolution  $d$  is seen in equation 1 below

$$d = \frac{1.22\lambda}{NA_{obj} + NA_{cond}} \quad 1$$

where  $\lambda$  is the wavelength of the light,  $NA_{obj}$  is the numerical aperture of the objective, and  $NA_{cond}$  is the numerical aperture of the condenser. Numerical aperture is defined as the refractive index of the imaging medium ( $n$ ) multiplied by the sine of the aperture angle ( $\alpha$ ):  $N.A. = n \cdot \sin(\alpha)$ .

While there are many types of optical techniques including bright field, dark field, phase contrast, *etc.*<sup>1</sup> the majority of this dissertation focuses around the technique of using totally internally reflected light to produce either fluorescent light or scattered light that is imaged by the objective.

Total internal reflection fluorescence microscopy (TIRFM) is an optical sectioning technique that has excelled in the study of molecular dynamics at solid/liquid interfaces and the study of cellular organization and dynamic processes within and near cellular membranes. Light propagating through a transparent medium will undergo total internal reflection (TIR) when it encounters an interface of a second medium with a lower index of refraction at an angle greater than the critical angle ( $\theta_c$ ) (from the normal of the interface). When TIR occurs, an evanescent field (EF) is generated at the interface of the two media characteristic of the reflected light beam that exponentially decays as distance increases from the surface. This EF can be used to excite fluorophores at a distance of a few hundred nanometers from the interface while essentially eliminating the out-of-focus fluorescence background.

After nearly three decades of intense research, TIRFM has already morphed into a mature technique for biological imaging by the time Axelrod published his last comprehensive review on TIRFM in 2008.<sup>6</sup> In this section, we will focus on the applications and techniques pertinent to single cell imaging published since 2008.

### Recent Advances in Instrumentation

*Automated Prism-Based System for High-Precision Imaging.* There are two basic types of TIRFM as determined by the optics that produce TIR. The first is objective-based TIRFM where the laser beam is directed off-center down a high NA objective. The optics within the objective produce a reflected beam at an angle equal to or greater than the critical angle, and TIR occurs at

the coverslip/sample interface. The emission signal is then directed back through the objective to the signal recorder. The second type of TIRFM is prism-based. Laser illumination is directed through the prism on which the sample lies. TIR occurs at the coverslip/sample interface, and emission is collected by an objective located on the opposite side of the prism. Various configurations of these two types of TIRFM have been discussed in a previous review.<sup>6</sup>

Each type of TIRFM holds its own advantages and drawbacks. The objective-based TIRFM is compact and commercially available as a module for standard light microscopes. Its main drawbacks include excitation light scattered within the objective, the difficulty in determining the incident angle, and the limitation on the range of achievable incident angles due to the geometry of the objective. These drawbacks can negatively influence the detection sensitivity and axial localization precision of fluorescent probes. All of these drawbacks can be avoided in prism-based TIRFM, which makes it an attractive technique for high-precision tracking applications. However, the performance of the prism-based system largely depends on the accuracy, precision, and reproducibility of the tedious, time-consuming calibration procedure to find the ideal illumination conditions at different incident angles.

To harvest the full benefits of the prism-based TIRFM and reduce the burden on the operator, an automated prism-based TIRFM was developed recently with the capability to accurately determine the ideal illumination conditions for a wide range of angles.<sup>7</sup> Once calibrated, the system can scan reliably and reproducibly through a wide range of incident angles with intervals as small as  $0.1^\circ$ . The unbiased calibration procedure ensures that the measured fluorescence intensities at tens to over a hundred different incident angles are consistent so that the data sets can be nonlinear least-squares fit with the decay functions to achieve high precision axial localization and better practical axial resolution.<sup>7</sup> It should be pointed out that this improvement is only achievable with a homogeneous liquid sample above the TIR surface. For a heterogeneous sample, such as cells, there is still no good way of accurately measuring the local EF field depth and profile.

Combined with the continuous fluorescent emission from nonblinking QDs,<sup>8</sup> the automated TIRFM can locate and track events taking place within the EF with exceptionally high precision.<sup>9</sup> The use of nonblinking QDs is necessary to avoid erratic fluorescence intensity curves due to conventional fluorescent probes' tendency to blink during system calibration and data acquisition. The axial distances of nonblinking QDs attached to stationary microtubules can

thus be determined with sub-10 nm precision, and the rotation of microtubules driven by kinesin motors can be detected in real time by resolving the movement of nonblinking QDs within a small vertical distance of  $\sim 50$  nm near the surface.<sup>9</sup>

Using a similar variable angle approach, Yang et al. reconstructed 3D microtubules within PtK2 cells using a Bayesian framework and quantified the lateral and axial curvatures of single microtubules by comparing their data to the computer simulations and electron microscopy images.<sup>10</sup>

*New Illumination Schemes.* The EF generated in TIRFM is no more than a few hundred nanometers in depth at the interface, which has limited the applicability of TIRFM to biological imaging. To work around this hindrance, the strategy of imaging at subcritical angles that are smaller than yet still close to the critical angle was proposed. At a subcritical incident angle, the excitation laser beam is refracted to produce a slanted illumination path; thus, it is possible to extend the thin illumination layer several micrometers into the cell body. The narrow field of illumination results in higher S/N than epi-fluorescence microscopy. This technique was coined variable-angle epi-fluorescence microscopy (VAEM),<sup>11</sup> highly inclined thin illumination (HILO),<sup>12</sup> or simply known as pseudo-TIRFM. The emitted light as a consequence of angled illumination, if collected directly, would appear tilted at the angle the sample is illuminated. By using a series of objectives and additional optics, oblique plane microscopy (OPM) can translate the image to be collected “flat” on the CCD.<sup>13</sup> All of these early implementations of pseudo-TIRFM were objective-based (Figure 1B). More recently, the same automation strategy described in the previous section was employed for prism-based pseudo-TIRFM (Figure 1D).<sup>14</sup>

Another improvement on illumination scheme was intended to remove the effect of interference fringes at different incident angles. The intensity profile of the incident laser can be negatively affected by scattering in the imperfect light path to give rise to interference fringes, resulting in a nonuniform illumination of the sample. Built upon the idea of azimuthal spinning of the incident laser beam,<sup>15</sup> Fiolka et al. used a piezo mirror to conveniently control the incident angle while producing an even sample illumination.<sup>16</sup>

In yet another effort to obtain both high S/N offered by prism-based TIRFM and the versatility of objective-based TIRFM in choosing thick sample substrates such as perfusion chambers and microarrays, a lightguide (LG)-based TIRFM has been constructed that bypasses excitation/emission interference while allowing applications requiring large sample holders and

large uniform evanescent fields.<sup>17</sup> Multicolor LG-TIRFM has been demonstrated for tracking dynamic lipids rafts on living cells cultured in perfusion chambers.<sup>17</sup> The fixed incident angle is considered a major drawback of LG-TIRFM.

*New Substrates.* Typical microscope slides and coverslips are usually chosen as the sample substrate for cell imaging because they allow for TIR and cell adhesion to the surface. Unfortunately, this can limit chemical access to the cell membrane due to cell surface contact. By using silica colloidal crystals as a porous substrate, researchers were able to allow ligand access to the cell membrane while still producing TIR angles in a wide range.<sup>18</sup> In another study, by changing the substrate to which the cells adhered to a subwavelength nanograting, fluorescence detection sensitivity was improved by coupled plasmon excitation.<sup>19</sup>

*Integration with Other Techniques.* To selectively monitor the dynamics between membrane bound proteins and a functionalized surface, a combination of TIRFM and optical trap was developed to “drop” a cell onto the surface under the objective.<sup>20</sup> This trap allows precise control of the initiation of interactions between a cell and a surface of interest, while the TIRFM could continuously monitor the surface interaction from the moment on onset. While an optical trap may be useful for single cell analysis, sometimes a high-throughput device is wanted for examining large batches of cells. To test the heterogeneity in a population of cells, TIRFM was combined with flow cytometry to examine cells at rates of 100–150 cells/s with single cell resolution.<sup>21</sup> The hydrodynamic focusing of the cells to the objective-based TIRFM allowed for the high-throughput sorting of cells based on their fluorescent signal. This signal can help determine how a large population of cells responds to certain conditions.

*Super-Resolution under TIRFM.* The intrinsic background reduction and high accessibility found in TIRFM make it a quality stepping point for super-resolution techniques. In stochastic optical reconstruction microscopy (STORM) or photoactivated localization microscopy (PALM), the decreased background associated with the optical sectioning allows for localization of the stochastically blinking fluorophores with fewer recorded photons than other wide-field methods. A prism-based setup also allows for the easy integration of multiple laser lines needed for the excitation and activation of the fluorophores, making STORM or PALM an accessible method for those needing to improve the lateral resolution in TIRFM.

A stimulated emission depletion (STED) microscope setup has been coupled to a TIRFM.<sup>22</sup> The advantage of this integration is that the STED system provides subdiffraction

lateral resolution while TIRFM limits the illumination depth, allowing for optical tomography. The authors were able to image immuno-stained microtubules within PtK2 cells at STED resolution while minimizing the penetration depth of the illumination source, thus reducing photo bleaching and phototoxicity.

Structured illumination microscopy (SIM) has also been coupled with TIRFM for the imaging of single cells in the past few years.<sup>23-26</sup> The easy integration with an inverted objective-based TIRF microscope allows for increased accessibility for researchers. While the resolution is not as good as stochastic techniques or STED, SIM-TIRFM has been able to break the 100 nm resolution barrier, and with the addition of a ferroelectric liquid crystal on silicon spatial light modulator, it is now possible to take images at video rate.<sup>23</sup>

### **Recent Applications in Membrane Studies and Plant Cell Imaging**

*Membrane Studies.* While the variability within the TIRFM technique is considered a reason for its successful implementation in many studies, simple unadulterated TIRFM can reveal much information about cellular membrane processes. Recent membrane investigations include the use of TIRFM to document real-time trafficking of a dopamine transporter (DAT) in response to the substrates, amphetamine, and dopamine,<sup>27</sup> and to study the purinergic-signaling cascade by directly visualizing ATP-loaded vesicles and their fusion to the plasma membrane.<sup>28</sup> Also, cancer screening agents such as QDs doped with ORMOSIL, which were stained on the cell membrane, were tested as optical probes.<sup>29</sup>

Another group used TIRFM to propose a fibroblast reorientation scheme.<sup>30</sup> They mapped the spatio-temporal dynamics of cell protrusion/retraction and PI3K signaling, which lead them to determine that randomly migrating fibroblasts reorient polarity through PI3K-dependent branching and pivoting of protrusions.

TIRFM has also recently been used to study the dynamic coordinated cytoskeletal rearrangements in drosophila by visualizing the cortical events with better spatial and temporal resolution,<sup>31</sup> and to study Eg5, a member of the kinesin-5 family, and its spatial-temporal distribution in mitosis.<sup>32</sup> The TIRFM results demonstrated that Eg5 dynamics within the mammalian spindle are region-specific, that the motor reorganizes at the different stages of mitosis, and that its dynamic reorganization is mediated by dynein and TPX2.<sup>32</sup>

Förster resonance energy transfer (FRET) benefits from the background reduction associated with TIRFM. TIRFM has been employed to visualize the real-time conformational changes in the actin transformation and correlate these changes to the presence of myosin.<sup>33</sup> FRET has been used on the plasma membrane to study SNARE interactions in living cells<sup>34</sup> and has been extended to the investigations of apoptosis by monitoring caspase activities.<sup>35</sup> The same authors have designed a FRET-based TIRF reader taking advantage of multiple TIR reflections for detection of apoptosis, drug screening, or in vitro diagnosis.<sup>36</sup>

Controlling the polarization of the incident illumination in TIRFM can divulge information about the fluorescent probe orientation and concentration. Two polarizations are commonly utilized: s-pol (perpendicular to the plane of incidence and parallel to the TIR surface) and p-pol (parallel to the plane of incidence and perpendicular to the TIR surface). Oriented fluorescent probes will fluoresce accordingly to the incident polarization. The simple ratio of p-pol/s-pol (P/S) images will mark deviations from sample uniformity, while P+2S is proportional to the effective concentration. Recently, the topological changes of chromaffin cells were monitored through the process of exocytosis.<sup>37</sup> As exocytosis occurs, the orientation of the labels attached to the membrane changes before resuming their original conformation.

*Plant Cell Imaging.* While TIRFM has a long-standing history in imaging and molecular tracking in animal cells, historically, applications have been limited involving plant cells. The single-most restricting factor to plant cell imaging is the thickness of the cell wall, which varies widely between species but is typically several hundreds of nanometers thick (>250 nm). Unsurprisingly, this has limited the use of TIRFM to in vitro investigations of actin cytoskeleton,<sup>38,39</sup> or to investigations near new growth where the cell wall is still relatively thin.<sup>40</sup> VAEM has been demonstrated to circumvent the challenges posted by cell walls in plant cell imaging.<sup>11</sup> While not truly TIRFM, the thin stepwise sample penetration keeps the advantages of optical sectioning, low background, and reduced photobleaching of the sample.

In 2011, two groups both found they could produce TIR at the inner boundary of the cell wall.<sup>41,42</sup> As previously mentioned, TIR occurs when light passing through one medium reaches the interface of second medium of a lower  $n$ . A typical cell wall has  $n$  between 1.42 and 1.48 bordering the cytosol, which has  $n$  of 1.38. Using variable angle systems with fine angle control allowed the researchers to move between glass slide TIRFM, VAEM, and cell wall TIRFM. Both groups were able to produce high-quality images of cytoskeleton and organelle markers. Wan et



al. were able to track a membrane-associated receptor and GFP labeled clathrin light chains with both VAEM and TIRFM observing different intensity traits.<sup>41</sup> Vizcay-Barrena et al. concluded single-molecule analysis of EGFP is possible within root cells using TIRFM (Figure 2).<sup>42</sup> Observing these events under TIRFM laid to rest the commonly held belief that TIRFM has little value in plant cell imaging.

### **Total Internal Reflection Scattering Microscopy**

Total internal reflection scattering (TIRS) microscopy is a technique where, similar to TIRFM, the illumination light undergoes total internal reflection at the sample-substrate interface. Instead of a fluorescent signal, the collected light is scattered from the sample. Originating as total internal reflection microscopy (TIRM), the technique was used to inspect surfaces for damage induced by lasers.<sup>43</sup> Since then TIRS microscopy has been used to measure colloidal and hydrodynamic forces,<sup>44-46</sup> and eventually became used to monitor the cellular uptake of sub-micron non-fluorescent particles.<sup>47</sup>

Recently TIRS microscopy has been applied to single metallic nanoparticle orientation determination.<sup>48, 49</sup> Metallic nanoparticles placed near a dielectric surface with high permittivity and illuminated with a frequency of light that aligns with the surface plasmon resonance of the particle will undergo coupling of the collective plasmon modes with the induced image charge.<sup>50-52</sup> This effect is reliant on the polarization of the incident light. If the light is s-pol, the induced image charge will negate the plasmon resonance of the particle, and no scattering enhancement will be seen. If the light is p-pol, the image charge will couple and enhance the plasmon resonance producing an image that is “doughnut” in shape.

An anisotropic particle that has an out-of-plane (tilt) angle with respect to the substrate plane will induce an image charge based on the 3D orientation of the particle.<sup>48</sup> A gold nanorod (AuNR) lying flat upon the surface will produce a “doughnut” shape with an intensity profile that alludes the direction of the long axis. If the AuNR is tilted the image produced has a “pacman” shape. The image profile will eventually become Gaussian in shape when the AuNR is oriented perpendicular to the surface. Through simulations of these interactions it is possible to match patterns to estimate the 3D orientation of the dielectric anisotropic nanoparticle.



## Differential Interference Contrast Microscopy

Differential interference contrast (DIC) microscopy is a technique typically used to enhance the contrast of unstained samples. Also known as Nomarski interference contrast or Nomarski microscopy, it was invented by Georges Nomarski in 1955. Compared to bright field microscopy, the optical components are decisively more complex. A schematic of the light path can be found in Figure 3.

A polarizer is first used to produce a polarized illumination source, which is then split into two orthogonally polarized wavefronts by a Normaski prism. These wavefronts are separated by what is called the sheer distance. This causes the two wavefronts to pass through a slightly different portion of the sample, thus being affected by the sample to different extents resulting in a phase delay. A second Nomarski prism is then used to recombine the orthogonal wavefronts. The phase delay will cause either constructive or destructive interference resulting in an image consisting of a gray background with signal either being lighter or darker than the background.

DIC microscopy produces characteristic images that appear as though they are being illuminated by a point source. Features within the image have a bright and dark side and appear to be three-dimensional. The high NA condenser and objectives that are used enables the DIC to image a very thin section of the sample due to the depth of focus. This leads to an improved image quality due to little out of focus light being captured.<sup>53</sup>

Since DIC microscopy does not require the staining of the specimens, it is commonly used in cell imaging. The technique can resolve features as small as the microtubules that make up the cytoskeleton of the cell (25 nm in diameter)<sup>54-56</sup> and has been used to monitor cell functions such as the motility of bacterial flagella,<sup>57</sup> and the assembly of sickle cell hemoglobin filaments<sup>58</sup>. DIC microscopy has even been used to differentiate between either gold or silver metallic nanoparticles as small as 10 nm, and has been used to follow the real-time particle endocytosis in HeLa cells.<sup>59</sup> Recently, the shadow-effect patters intrinsic to DIC microscopy have been utilized to resolve the orientation information of anisotropic nanoparticles in controlled environments<sup>60</sup> and within cells.<sup>61</sup>

## Dissertation Focus

This dissertation focuses mainly on the application and advancement of TIRF, TIRS, and DIC microscopy. TIRF and TIRS microscopy were used for investigating single-particle motion and rotation on biologically relevant systems, while a homebuilt Nomarski DIC microscope was built in reflection-mode to study nanoparticles and nanostructures on reflective surfaces. The work was carried out in three main directions:

(1) **Implementation of “non-blinking” CdSe/CdS nanocrystal quantum dots to investigate biological systems.** Semiconductor quantum dots (QDs) are fluorescent particles that have intrinsic properties that hold advantage compared to organic fluorophores such as broad absorption and narrow size-tunable emission spectra<sup>62, 63</sup> and increased photostability.<sup>64</sup> Despite all these advantages, QDs have the intrinsic trait of fluorescence intermittency commonly referred to as “blinking”. This is a significant drawback in single-particle tracking (SPT) experiments when trying to continuously determine their absolute positions. While some methods have been established to reduce fluorescence intermittency by modifying the surrounding environment,<sup>65, 66</sup> a new type of core/shell QD has been introduced that has drastically improved blinking statistics.<sup>67-69</sup>

The new QDs, referred to as “non-blinking” QDs (NBQDs), have enough fluorescent stability to be implemented as single-particle probes for investigating the movement of molecular motors and the nanometer vertical displacements they can induce by scanning-angle TIRF microscopy. Varying the angle of incident illumination directly affects the depth of the EF and therefore the intensity of the particle’s fluorescence.<sup>7</sup> The NBQDs were attached to stationary microtubules while the fluorescence intensity was recorded as a function of incident angle. The curve of the plot revealed the vertical position of the particle. Precise control of the EF can allow for the tracking of nanoscale vertical displacement of NBQDs as non-13-protofilament microtubules propelled by the motor protein kinesin rotated across the substrate surface.

In a separate experiment, the surface loading of NBQDs with a cholesterol derivative was controlled with respect to complete PEG coating. Cholestanone is known to incorporate itself with phospholipid membranes. Observations showed that movement of the particle across the lipid bilayer surface is directly related to the amount of particle surface occupied by cholestanone. Calculations of the number of cholestanone molecules infused with the surface creating a drag force opposite particle diffusion matched well with observations.

**(2) Advancing TIRS microscopy for the determination of the 3D orientation for dynamic and static nanoparticle.** Techniques under dark field (DF) microscopy have used AuNRs as orientation probes as these particles preferentially scatter light along their longitudinal axis.<sup>70-72</sup> Though DF is a convenient technique, it has only been able to resolve orientation in two dimensions. Intrinsic to the nanoparticle is the surface plasmon resonance (SPR), which is the oscillation of free electrons in the metal at a certain frequency. Because of the rod shape of AuNRs there is both a short and long axis SPR. When a polarized light source with the same frequency of the SPR illuminates the particles, an enhancement of the SPR will result in an increased scattering signal.

A dual-color TIRS microscope was constructed that can observe both SPR enhancements simultaneously using a dual-view system. By manipulating the polarization orientation of the incoming laser lines, in-plane and out-of-plane (tilt) orientation information of the AuNR could be resolved. The scattering profile produces a Gaussian point spread function profile that can be super-localized. Combining the orientation and location information, a study of particle-lipid membrane interaction was performed.

In a separate experiment, the 3D orientation of AuNRs was determined for stationary particles. By rotating the polarization direction of incoming linearly polarized light, different extents of s-pol and p-pol are produced in the evanescent field under TIR. The scattering intensity maximum for a particular AuNR is dependent upon the 3D orientation of the particle. By matching the scattering intensity profile of a particle with its in-plane orientation, the polar angle of the particle can be accurately determined.

**(3) Developing a reflected-mode Nomarski differential interference contrast microscope for the study of nanoparticle and nanostructures.** Traditionally, DIC microscopy has been used to study systems on transparent substrates using a second Nomarski prism after the sample to recombine the sheared light. In reflection mode, there is need for only one Nomarski prism placed in the back focal plane of the condenser as the condenser also acts as the objective. The single Nomarski prism both shears and recombines the light. Reflected DIC was developed in 1979 primarily for use in surface topography studies,<sup>73</sup> though it is currently a convenient method to inspect chips based on silica wafers.

A reflected-mode Nomarski DIC microscope with a laser illumination source was constructed to image nanoparticles and nanostructures developed on reflective surfaces. The

setup can distinguish 3D orientations of gold nanorods under the axial SPR excitation mode. The study was extended into imaging nanostructures created through lithography on silica wafers.

## References

1. Davidson, M. W.; Abramowitz, M., Optical Microscopy. In *Encyclopedia of Imaging Science and Technology*, 2002.
2. Williams, D. B.; Carter, C. B., *Transmission Electron Microscopy*. Plenum Press: New York, 1996.
3. Kalinin, S.; Gruverman, A., *Scanning Probe Microscopy*. Springer Science & Business Media: New York, 2007.
4. Schilling, G.; Christensen, L. L., *Eyes on the Skies: 400 Years of Telescopic Discovery*. Wiley-VCH: 2009.
5. Kapitza, H. G., Microscopy from the very beginning. In Zeiss, Ed. 1997.
6. Axelrod, D., Total Internal Reflection Fluorescence Microscopy. In *Biophysical Tools for Biologists, Vol 2: In Vivo Techniques*, Correia, J. J.; Detrich, H. W., Eds. 2008; Vol. 89, pp 169-221.
7. Sun, W.; Marchuk, K.; Wang, G. F.; Fang, N. *Analytical Chemistry* **2010**, 82, (6), 2441-2447.
8. Guo, Y.; Marchuk, K.; Sampat, S.; Abraham, R.; Fang, N.; Malko, A. V.; Vela, J. *The Journal of Physical Chemistry C* **2011**, 116, (4), 2791-2800.
9. Marchuk, K.; Guo, Y. J.; Sun, W.; Vela, J.; Fang, N. *Journal of the American Chemical Society* **2012**, 134, (14), 6108-6111.
10. Yang, Q.; Karpikov, A.; Toomre, D.; Duncan, J. S. *Ieee Transactions on Image Processing* **2011**, 20, (8), 2248-2259.
11. Konopka, C. A.; Bednarek, S. Y. *Plant Journal* **2008**, 53, (1), 186-196.
12. Tokunaga, M.; Imamoto, N.; Sakata-Sogawa, K. *Nature Methods* **2008**, 5, (2), 159-161.
13. Dunsby, C. *Optics Express* **2008**, 16, (25), 20306-20316.
14. Sun, W.; Xu, A. S.; Marchuk, K.; Wang, G. F.; Fang, N. *Jala* **2011**, 16, (4), 255-262.
15. Mattheyses, A. L.; Simon, S. M.; Rappoport, J. Z. *Journal of Cell Science* **2010**, 123, (21), 3621-3628.

16. Fiolka, R.; Belyaev, Y.; Ewers, H.; Stemmer, A. *Microscopy Research and Technique* **2008**, 71, (1), 45-50.
17. Asanov, A.; Zepeda, A.; Vaca, L. *Biochimica Et Biophysica Acta-Molecular and Cell Biology of Lipids* **2010**, 1801, (2), 147-155.
18. Velarde, T. R. C.; Wirth, M. J. *Applied Spectroscopy* **2008**, 62, (6), 611-616.
19. Kim, K.; Kim, D. J.; Cho, E. J.; Suh, J. S.; Huh, Y. M.; Kim, D. *Nanotechnology* **2009**, 20, (1).
20. Snijder-Van As, M. I.; Rieger, B.; Joosten, B.; Subramaniam, V.; Figdor, C. G.; Kanger, J. S. *Journal of Microscopy-Oxford* **2009**, 233, (1), 84-92.
21. Wang, J.; Bao, N.; Paris, L. L.; Geahlen, R. L.; Lu, C. *Analytical Chemistry* **2008**, 80, (24), 9840-9844.
22. Gould, T. J.; Myers, J. R.; Bewersdorf, J. *Optics Express* **2011**, 19, (14), 13351-13357.
23. Kner, P.; Chhun, B. B.; Griffis, E. R.; Winoto, L.; Gustafsson, M. G. L. *Nature Methods* **2009**, 6, (5), 339-U36.
24. Chung, E.; Kim, D.; Cui, Y.; Kim, Y. H.; Soy, P. T. C. *Biophysical Journal* **2007**, 93, (5), 1747-1757.
25. Gliko, O.; Reddy, G. D.; Anvari, B.; Brownell, W. E.; Saggau, P. *Journal of Biomedical Optics* **2006**, 11, (6).
26. Beck, M.; Aschwanden, M.; Stemmer, A. *Journal of Microscopy* **2008**, 232, (1), 99-105.
27. Furman, C. A.; Chen, R.; Guptaroy, B.; Zhang, M.; Holz, R. W.; Gnegy, M. *Journal of Neuroscience* **2009**, 29, (10), 3328-3336.
28. Akopova, I.; Tatur, S.; Grygorczyk, M.; Luchowski, R.; Gryczynski, I.; Gryczynski, Z.; Borejdo, J.; Grygorczyk, R. *Purinergic Signalling* **2012**, 8, (1), 59-70.
29. Qian, J.; Chen, Q. L.; Cai, F. H.; Kong, S. K.; Ho, H. P.; He, S. L. *Ieee Journal of Selected Topics in Quantum Electronics* **2009**, 15, (5), 1374-1379.
30. Welf, E. S.; Ahmed, S.; Johnson, H. E.; Melvin, A. T.; Haugh, J. M. *Journal of Cell Biology* **2012**, 197, (1), 105-114.
31. Webb, R. L.; Rozov, O.; Watkins, S. C.; McCartney, B. M. *Developmental Dynamics* **2009**, 238, (10), 2622-2632.

32. Gable, A.; Qiu, M. H.; Titus, J.; Balchand, S.; Ferenz, N. P.; Ma, N.; Collins, E. S.; Fagerstrom, C.; Ross, J. L.; Yang, G.; Wadsworth, P. *Molecular Biology of the Cell* **2012**, 23, (7), 1254-1266.
33. Kozuka, J.; Yokota, H.; Arai, Y.; Ishii, Y.; Yanagida, T. *Nature Chemical Biology* **2006**, 2, (2), 83-86.
34. Wang, L.; Bittner, M. A.; Axelrod, D.; Holz, R. W. *Molecular Biology of the Cell* **2008**, 19, (9), 3944-3955.
35. Angres, B.; Steuer, H.; Weber, P.; Wagner, M.; Schneckenburger, H. *Cytometry Part A* **2009**, 75A, (5), 420-427.
36. Bruns, T.; Angres, B.; Steuer, H.; Weber, P.; Wagner, M.; Schneckenburger, H. *Journal of Biomedical Optics* **2009**, 14, (2).
37. Anantharam, A.; Onoa, B.; Edwards, R. H.; Holz, R. W.; Axelrod, D. *Journal of Cell Biology* **2010**, 188, (3), 415-428.
38. Michelot, A.; Guerin, C.; Huang, S. J.; Ingouff, M.; Richard, S.; Rodiuc, N.; Staiger, C. J.; Blanchoin, L. *Plant Cell* **2005**, 17, (8), 2296-2313.
39. Michelot, A.; Derivery, E.; Paterski-Boujemaa, R.; Guerin, C.; Huang, S. J.; Parcy, F.; Staiger, C. J.; Blanchoin, L. *Current Biology* **2006**, 16, (19), 1924-1930.
40. Wang, X. H.; Teng, Y.; Wang, Q. L.; Li, X. J.; Sheng, X. Y.; Zheng, M. Z.; Samaj, J.; Baluska, F.; Lin, J. X. *Plant Physiology* **2006**, 141, (4), 1591-1603.
41. Wan, Y. L.; Ill, W. M. A.; Fan, L. S.; Hao, H. Q.; Kim, M. K.; Lin, J. X. *Plant Methods* **2011**, 7.
42. Vizcay-Barrena, G.; Webb, S. E. D.; Martin-Fernandez, M. L.; Wilson, Z. A. *Journal of Experimental Botany* **2011**, 62, (15), 5419-5428.
43. Temple, P. A. *Applied Optics* **1981**, 20, (15), 2656-2664.
44. Prieve, D. C.; Luo, F.; Lanni, F. *Faraday Discussions* **1987**, 83, 297-307.
45. Prieve, D. C.; Frej, N. A. *Langmuir* **1990**, 6, (2), 396-403.
46. Oetama, R. J.; Walz, J. Y. *Journal of Colloid and Interface Science* **2005**, 284, (1), 323-331.
47. Byrne, G. D.; Pitter, M. C.; Zhang, J.; Falcone, F. H.; Stolnik, S.; Somekh, M. G. *Journal of Microscopy* **2008**, 231, (1), 168-179.
48. Ha, J. W.; Marchuk, K.; Fang, N. *Nano Letters* **2012**, 12, (8), 4282-4288.

49. Koen, K. A.; Weber, M. L.; Mayer, K. M.; Fernandez, E.; Willets, K. A. *The Journal of Physical Chemistry C* **2012**, 116, (30), 16198-16206.
50. Swanglap, P.; Slaughter, L. S.; Chang, W. S.; Willingham, B.; Khanal, B. P.; Zubarev, E. R.; Link, S. *Acs Nano* **2011**, 5, (6), 4892-4901.
51. Mock, J. J.; Hill, R. T.; Degiron, A.; Zauscher, S.; Chilkoti, A.; Smith, D. R. *Nano Letters* **2008**, 8, (8), 2245-2252.
52. Chen, H. J.; Ming, T.; Zhang, S. R.; Jin, Z.; Yang, B. C.; Wang, J. F. *Acs Nano* **2011**, 5, (6), 4865-4877.
53. Tsunoda, M.; Isailovic, D.; Yeung, E. S. *Journal of Microscopy* **2008**, 232, (2), 207-211.
54. Allen, R. D.; Weiss, D. G.; Hayden, J. H.; Brown, D. T.; Fujiwake, H.; Simpson, M. *Journal of Cell Biology* **1985**, 100, (5), 1736-1752.
55. Salmon, E. D. *Trends in Cell Biology* **1995**, 5, (4), 154-158.
56. Cassimeris, L.; Pryer, N. K.; Salmon, E. D. *Journal of Cell Biology* **1988**, 107, (6), 2223-2231.
57. Block, S. M.; Fahrner, K. A.; Berg, H. C. *Journal of Bacteriology* **1991**, 173, (2), 933-936.
58. Samuel, R. E.; Salmon, E. D.; Briehl, R. W. *Nature* **1990**, 345, (6278), 833-835.
59. Sun, W.; Wang, G. F.; Fang, N.; Yeung, E. S. *Analytical Chemistry* **2009**, 81, (22), 9203-9208.
60. Wang, G. F.; Sun, W.; Luo, Y.; Fang, N. *Journal of the American Chemical Society* **2010**, 132, (46), 16417-16422.
61. Sun, W.; Gu, Y.; Wang, G.; Fang, N. *Analytical Chemistry* **2012**, 84, (2), 1134-1138.
62. Bruchez, M.; Moronne, M.; Gin, P.; Weiss, S.; Alivisatos, A. P. *Science* **1998**, 281, (5385), 2013-2016.
63. Han, M. Y.; Gao, X. H.; Su, J. Z.; Nie, S. *Nature Biotechnology* **2001**, 19, (7), 631-635.
64. Chan, W. C. W.; Nie, S. M. *Science* **1998**, 281, (5385), 2016-2018.
65. Hohng, S.; Ha, T. *Journal of the American Chemical Society* **2004**, 126, (5), 1324-1325.
66. Fomenko, V.; Nesbitt, D. J. *Nano Letters* **2008**, 8, (1), 287-293.
67. Wang, X. Y.; Ren, X. F.; Kahen, K.; Hahn, M. A.; Rajeswaran, M.; Maccagnano-Zacher, S.; Silcox, J.; Cragg, G. E.; Efros, A. L.; Krauss, T. D. *Nature* **2009**, 459, (7247), 686-689.

68. Mahler, B.; Spinicelli, P.; Buil, S.; Quelin, X.; Hermier, J. P.; Dubertret, B. *Nature Materials* **2008**, 7, (8), 659-664.
69. Chen, Y.; Vela, J.; Htoon, H.; Casson, J. L.; Werder, D. J.; Bussian, D. A.; Klimov, V. I.; Hollingsworth, J. A. *Journal of the American Chemical Society* **2008**, 130, (15), 5026-+.
70. Sonnichsen, C.; Alivisatos, A. P. *Nano Letters* **2005**, 5, (2), 301-304.
71. Xiao, L. H.; Qiao, Y. X.; He, Y.; Yeung, E. S. *Journal of the American Chemical Society* **2011**, 133, (27), 10638-10645.
72. Pierrat, S.; Hartinger, E.; Faiss, S.; Janshoff, A.; Soennichsen, C. *Journal of Physical Chemistry C* **2009**, 113, (26), 11179-11183.
73. Lessor, D. L.; Hartman, J. S.; Gordon, R. L. *Journal of the Optical Society of America* **1979**, 69, (2), 357-366.



## Figures

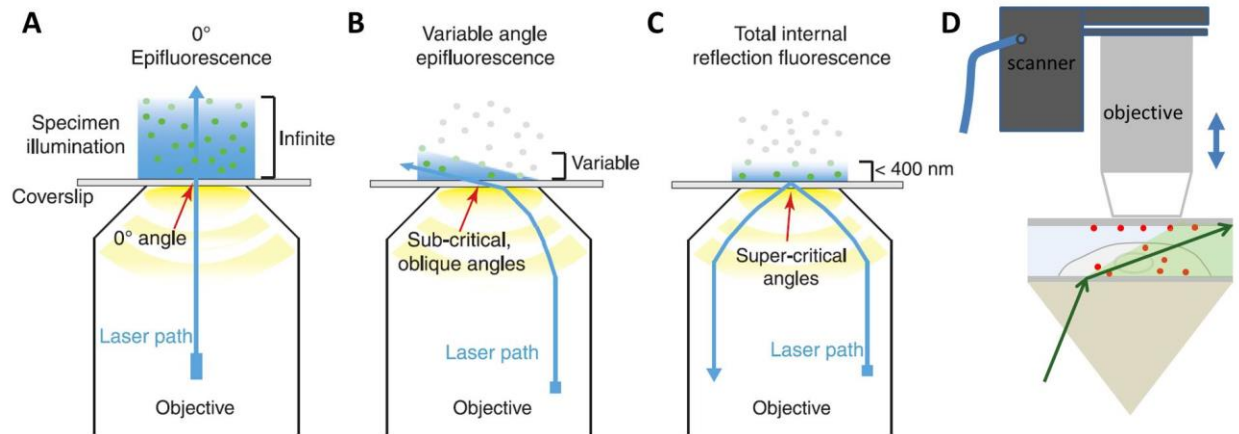


**Figure 1.** Various TIRFM and VAEM configurations. (A) Epi-fluorescence. (B) Objective-based VAEM. (C) Objective-based TIRFM. Reprinted with permission from ref 6. Copyright 2008 Blackwell Publishing Ltd. (D) Prism-based VAEM. The objective scanner facilitates vertical sectioning of the sample. Reprinted with permission from ref 9. Copyright 2011 Elsevier. The components are not drawn to scale.

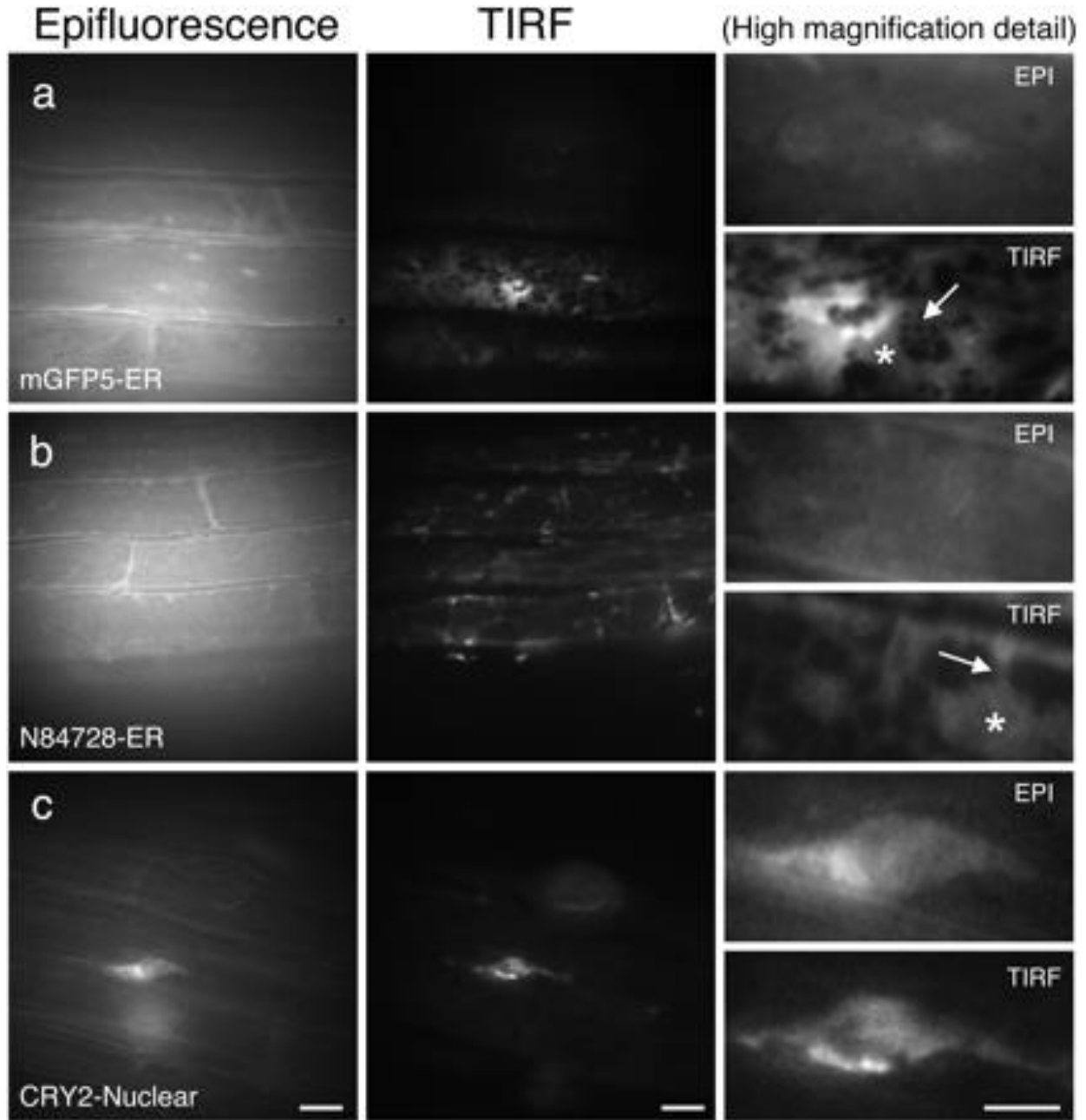


**Figure 2.** Analysis of subcellular organelle markers by epifluorescence and TIRFM in roots. Arabidopsis roots imaged using epifluorescence and TIRFM. (a) mGFP5-ER (ER marker); (b) N84728 (ER marker); individual ER structures and the presence of extended cisternal lamellae connected to a tubular ER network can only be distinguished in the TIRF images (asterisks, ER cisternae; arrow, ER tubules); (c) N84733 (chromosome marker). Scale bars in left and middle column represent 10  $\mu$  m. Scale bars in rightmost column represent 5  $\mu$  m. Reprinted with permission from ref 37. Copyright 2011 Oxford University Press.

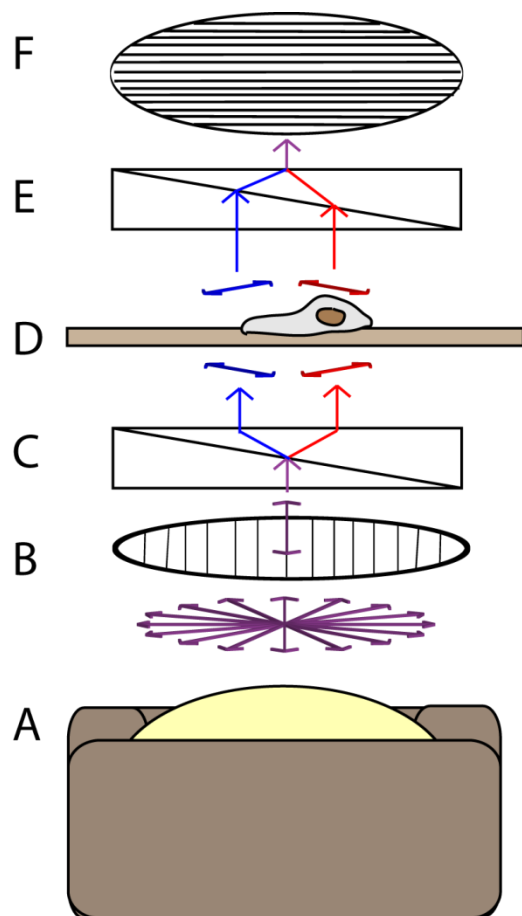


**Figure 3.** Representation of the light path in DIC microscopy. Light originates from the light source (A), passes first through a polarizer (B) followed by the first Nomarski prism (C) before reaching the sample (D). The then recombines in the second Nomarski prism (E), passes through the second polarizer (F) before reaching the detector.

## CHAPTER 2: HIGH-PRECISION TRACKING WITH NON-BLINKING QUANTUM DOTS RESOLVES NANOSCALE VERTICAL DISPLACEMENT

Kyle Marchuk, Yijun Guo, Wei Sun, Javier Vela, and Ning Fang

Published in Journal of the American Chemical Society<sup>§</sup>

### Abstract

Novel non-blinking quantum dots (NBQDs) were utilized in three-dimensional super-localization, high-precision tracking applications under an automated scanning-angle total internal reflection fluorescence microscope (SA-TIRFM). NBQDs were randomly attached to stationary microtubules along the radial axis under gliding assay conditions. By automatically scanning through a wide range of incident angles with different evanescent-field layer thicknesses, the fluorescence intensity decay curves were obtained. Fit with theoretical decay functions, the absolute vertical positions were determined with sub-10-nm localization precision. The emission intensity profile of the NBQDs attached to kinesin-propelled microtubules was used to resolve the self-rotation of gliding microtubules within a small vertical distance of ~50 nm. We demonstrate the applicability of NBQDs in high-precision fluorescence imaging experiments.

### Introduction

Tracking single molecule and nanoparticle probes with a precision of sub-nanometer to a few tens of nanometers is crucial for elucidating nanoscale structures and movements in biological systems. Semiconductor quantum dots (QDs) have intrinsic fluorescent properties that hold advantage over traditional organic fluorophores such as broad absorption and narrow size-

---

<sup>§</sup> Reprinted with permission from Journal of the American Chemical Society, **2012**, 134(14), 6108-6111. Copyright © American Chemical Society

tunable emission spectra<sup>1,2</sup> and increased photostability;<sup>3</sup> however, the use of QDs in high-precision single-particle tracking (SPT) applications has been greatly limited by their intrinsic trait of single-particle fluorescence intermittency commonly referred to as “blinking.” While mild reducing agents or electron donating environments can help suppress this trait,<sup>4,5</sup> these methods are not always applicable. These reagents can present problems for biological systems by causing interruptions to disulfide linkages and other redox-susceptible groups in biomolecules, or simply, methods such as these may not suppress intermittency enough to be useful in high-precision SPT experiments.

The introduction of a new type of core/shell semiconductor QDs<sup>6-8</sup> satisfies many of the needs for continuous emission single-fluorophore experiments. These QDs are referred to as “non-blinking” quantum dots (NBQDs) for their statistical supremacy in fluorescent intermittency behavior compared to conventional QDs. However, even with all the hype around NBQDs, to the best of our knowledge, there has not been any study that realizes the full potential of NBQDs for three-dimensional (3D) high-precision dynamic tracking.<sup>9</sup>

While super-localization in the horizontal (x-y) plane is now considered a routine procedure, super-localization in the axial (z) direction remains challenging and requires special techniques, including invoking optical astigmatism,<sup>10</sup> bipplane imaging,<sup>11,12</sup> temporal focusing,<sup>13</sup> or using a double-helix point spread function.<sup>14</sup> In the present study, we employed a fully automated prism-type scanning-angle total internal reflection fluorescence microscope (SA-TIRFM)<sup>15,16</sup> in combination with NBQDs for 3D dynamic tracking near the total internal reflection (TIR) interface with a sub-10-nm axial localization precision.

The use of TIR geometry holds many advantages in single particle localization and tracking experiments.<sup>17</sup> The generation of an exponentially decaying evanescent field (EF) at the surface of TIR allows for significant background reduction, while the depth of the EF can be adjusted with control of the incident illumination angle. Our SA-TIRFM uses an in-house computer program that can accurately determine the ideal illumination area under the objective and reliably reproduce the position for a wide range of angles.<sup>15,16</sup> Combined with the continuous fluorescent emission from the NBQDs, the SA-TIRFM can locate and track events taking place within the EF with exceptionally high precision. The use of NBQDs is necessary to avoid erratic fluorescent emission curves due to conventional QDs’ tendency to blink during system calibration and data acquisition.

The high axial localization precision of our imaging system was utilized to determine the absolute vertical positions of NBQDs attached to stationary microtubules and resolve the rotational motion of gliding microtubules, which takes place within a vertical distance of  $\sim 50$  nm near the substrate surface. Motor proteins, such as kinesin, are essential to cellular functions by transporting intracellular cargoes throughout the cell. This ability has illuminated the great potential of motor proteins to serve in engineered transport systems as components in nanomachines that sort and shuttle cargoes to designated locations. It has been found that by fixing kinesin to a surface followed by introducing solutions of microtubules and adenosine-5'-triphosphate (ATP), the microtubules will be propelled laterally.<sup>18-25</sup> The number of protofilaments composing the microtubule determines the particular motion the microtubule undertakes as it is propelled by kinesin. If a microtubule is composed of protofilament count differing from 13, the microtubule rotates around its longitudinal axis due to the step-wise motion of kinesin<sup>18</sup>. Using conventional QDs in fluorescence interference contrast (FLIC) microscopy<sup>24</sup> or plasmonic gold nanorods in single particle orientation and rotational tracking (SPORT) under a differential interference contrast (DIC) microscope,<sup>15</sup> the detection of the gliding self-rotating was successfully demonstrated. Herein, we present a novel approach to resolve the rotational motion by precisely following the vertical positions of the NBQDs attached to the self-rotating microtubules.

## Results and Discussion

Thick-shell NBQDs with a 4.7 nm diameter CdSe core surrounded by 17 atomic monolayers (MLs) of CdS (CdSe/17CdS) were synthesized following our recently published approach that utilizes an improved synthetic reliability and reproducibility compared to previous methods.<sup>26</sup> Comprehensive statistical analyses of the fluorescence intermittency for the NBQDs, thin-shell quantum dots (TSQDs), and commercial QDs (EviTag T2) were performed for a large sample size of individual particles (see Table 1 for detail). Without modification or a blinking suppressant environment, the NBQDs easily surpass the commercial QDs with regards to fluorescent intermittency. These statistics make the absolute positioning and 3D dynamic tracking of NBQDs possible.

Axial localization was accomplished by attaching the NBQDs through the biotin-neutravidin interaction under gliding assay conditions in quartz microscope slide chambers. The

microtubules were held static by withholding the final ATP rich gliding assay solution (see Methods for detail). The incident angle of the excitation laser was varied from the large angle of  $88.3^\circ$  to the critical angle of  $67.3^\circ$  in increments of approximately  $0.25^\circ$ , which expanded the EF deeper into the sample. Figure 1A shows the increase in fluorescent signal for two NBQDs attached to microtubules at different axial positions as the incident angle was varied. It can be easily seen that the relative vertical distances of the NBQDs labeled as 1 and 2 have a relationship of  $z_1 < z_2$ . Their *absolute* axial distances can be determined to be  $19.0 \pm 7.5$  nm and  $50.8 \pm 4.3$  nm, respectively, by nonlinear least squares (NLLS) fitting<sup>15</sup> of the intensity curves shown in Figure 1B. These measurements fall within the expected range of vertical distances dictated by the geometrical constraints of the system (Figure 1D), which include the size of the microtubule, length of kinesin, the biotin-neutravidin interaction, and the diameter of the NBQD.

A complete explanation of the error analysis used in the NLLS fitting can be found in the Methods section and a thorough uncertainty study can be found in our previous work.<sup>15</sup> Briefly, a  $\chi^2$  test was performed on the experimental and theoretical fluorescence values for each angle. A confidence interval for the calculated  $z$  was then determined using  $F_\chi$  statistics for the appropriate parameters and degrees of freedom. It should be emphasized that the high localization precision was realized with the ability of our instrument to find and replicate the optimal incident illumination light angles and the consistency of the NBQDs to stay in the fluorescent emission state for prolonged periods of time.

The NBQDs are ideal probes not only for axial localization in static systems but also for tracking 3D position changes in dynamic systems. The absolute position cannot be determined for dynamic systems using SA-TIRF due to the time needed to image multiple angles, however, our system allows for the relative axial changes to be idealized. Microtubules composed of 13 protofilaments do not rotate while moving laterally across a kinesin-coated surface. Therefore, the expected trace produced by a NBQD attached to a gliding microtubule would be a consistent signal as the microtubule travels along at the same depth in the EF. Figure 2 displays a trace produced by a NBQD attached to a microtubule propelled by kinesin.

As can be seen, the NBQD did not blink once during the entire acquisition, which allowed the determination of this non-rotating microtubule. Figure 4 portrays a comparison between NBQDs and TSQDs under gliding assay conditions both moving and stationary (without ATP). The protofilament count of the moving microtubule to which the TSQD is

attached is lost in the ambiguity of the emission profile. It is impossible to discern whether the fluctuations in emission intensity are due completely to the fluorescent intermittency or whether there is a change in the axial distance of the TSQD as the microtubule glided across the surface. It should be noted that an oxygen scavenging system (described in Supplementary Methods) is present for all examples of microtubule motion, but it is not present for stationary microtubules.

The self-induced longitudinal rotation of non-13-protofilament microtubules with attached NBQDs is confined to a  $z$ -depth of  $\sim 50$  nm. It is important to choose an incident angle that will most readily reveal this minimal axial translation. An advantage of the automated SA-TIRFM is the ability to easily select an ideal angle for a given set of experiments and reproduce it reliably. The depth  $d(\theta)$  of the EF propagating from the surface of TIR is directly related to the angle of incident light, which corresponds to the fluorescent intensity decay at various axial distances ( $z$ ). Thus, a larger angle equates to a thinner EF, which produces a greater relative change in fluorescent intensity as the axial position of the fluorophore changes. This relationship can be visualized in Figure 5.

The ideal angle for tracking the rotation of NBQDs attached to microtubules maximizes the change of fluorescence intensity as the NBQD moves toward and away from the TIR surface, while keeping the minimum emission intensity above the background noise. This aspect is also limited by other practical elements of the experiment such as the quantum efficiency of the probe and the intensity of the excitation source.

With the proper angle chosen, a vast amount of information was readily discernible by the intensity profiles produced in the NBQD traces. Figure 3 shows an example trace of an NBQD attached to a rotating microtubule followed for two full periods. It is easy to observe the maximum and minimum intensities as the microtubule travels laterally across the surface. The fluorescent intensity trace seen in Figure 3A was recorded using an incident angle of  $80.1^\circ$ , which produces an EF depth of 77 nm. The relative change in axial distance  $\Delta z$  was calculated<sup>27</sup> to be 49.5 nm, which translates to the axial distance traveled by the NBQD during microtubule rotation. This value aligns well with the estimated geometrical constraints previously mentioned.

Using a particle tracking plugin within the open-source program *ImageJ*, we tracked the lateral distance traveled during the periods of rotation. The distances were measured to be  $\sim 3.1$   $\mu\text{m}$  for both rotations. This corresponds to the super-twist length of a microtubule composed of 12 protofilaments.<sup>18</sup>



A second microtubule trace was analyzed, which can be seen in Supplementary Figure 6A. For this recording a smaller incident light angle of  $75.6^\circ$  was used, which produced an EF depth of 90 nm. The rotation curve is noticeably shallower than the one seen in Figure 2. Though this makes the determination on the fluorescence minimum slightly more difficult, the axial rotation distance of 45.6 nm was calculated and the lateral distance traveled was measured at 5.4  $\mu\text{m}$  and 5.7  $\mu\text{m}$  from the two rotations. These lateral distances correspond to a 14-protofilament microtubule.<sup>18</sup>

## Conclusion

In summary, novel QDs with suppressed fluorescence intermittency were used in 3D super-localization and dynamic tracking experiments to achieve exceptionally high precision. The combination of the fully automated SA-TIRFM and NBQDs enabled us to find the absolute vertical positions of NBQDs attached along the rotational axis of stationary microtubules. The ability to easily tune the incident illumination angle and the stable fluorescent signal of NBQDs allowed us to discern the self-rotation of kinesin-driven microtubules taking place within a limited axial width. Looking forward, as the understanding of fluorescence intermittency increases, QDs will continue to become more versatile in their applications. Already, prolate nanocrystals have been published that continuously fluoresce by utilizing a graded core/shell synthetic procedure.<sup>7</sup> As this and other techniques produce smaller and brighter “non-blinking” semiconductor probes with reduced cytotoxicity, opportunities will arise in such applications as intracellular multi-color single-molecule tracking, observing signal transduction pathways, and understanding membrane processes such as endocytosis, exocytosis, and the formation and function of membrane micro- and nanodomains.

## Methods

**SA-TIRF microscope.** The apparatus was built around a Nikon Optihot-2 microscope utilizing a Plan Fluor 100 $\times$ /NA 1.3 objective and Andor iXon<sup>EM</sup>+ 897 camera (Belfast, Northern Ireland; 512 x 512 imaging array, 16  $\mu\text{m}$  x 16  $\mu\text{m}$  pixel size). The original microscope stage was removed and replaced with a Sutter MP-285 motorized high precision three-dimensional translational stage (Novato, CA). A homemade prism holder was attached to the Sutter stage, which held an equilateral Bk7 prism (Melles Griot, Albuquerque, NM). An adjustable 75-mW

maximum 488-nm argon continuous wave (CW) laser (Uniphase, San Jose, CA) was used as the excitation source working at 20-mW output. A series of optics and motorized stages were set up to direct the laser path beneath the objective. First the laser beam was directed to a periscope and through a Uniblitz mechanical shutter (model LS2Z2, Vincent Associates, Rochester, NY). The beam then passed through a focusing lens (15-cm focal length) and on to the mirror of a galvanometer optical scanner (model 6220H, Cambridge Technology, Cambridge, MA). Two RazorEdge Long Pass 488 nm filters were placed in the optical path before the EMCCD.

The focusing lens was used to control the laser illumination size under the objective, which was adjusted to approximately 128  $\mu\text{m}$  in diameter. This area corresponds to twice the width of the viewing area under the objective (64  $\mu\text{m}$  x 64  $\mu\text{m}$ ) and allows for a less Gaussian energy distribution in the illumination area. The laser power at the surface of TIR was approximately 100  $\text{W}/\text{cm}^2$ . The mirror galvanometer was used in conjunction with a high precision motorized linear stage (model MAA-PP, Newport, Irvine, CA) to direct the laser beam through the equilateral prism to the solid-liquid interface at different incident angles. An in-house software program was utilized to optimize the laser spot under the objective during various angles of incident light.

**Non-blinking quantum dot (NBQD) and thin-shelled quantum dot (TSQD) synthesis.**<sup>28</sup> **Materials.** Cadmium oxide (CdO, 99.998%), sulfur ( $\text{S}_8$ , 99.999%), trioctylphosphine (TOP, 90%) and oleic acid (90%) were purchased from Alfa Aesar; selenium (Se, pellets,  $\geq 99.999\%$ ) and dioctylamine (98%) from Sigma-Aldrich; 1-octadecene (ODE) (90%) and oleylamine (80-90%) from Acros. Bis(2,2,4-trimethylpentyl)phosphinic acid (TMPPA) (CYANEX 272<sup>®</sup>) was obtained from Cytec Industries, Inc. Procedures were performed under dry inert gas atmosphere ( $\text{N}_2$  or Ar) in a glove box or a Schlenk line. **Precursor solutions.** *0.16M TOPSe/ODE.* Se (71.4 mg, 904  $\mu\text{mol}$ ), TOP (577 mg, 1.56 mmol) and ODE (4.00 g, 15.84 mmol) were stirred and heated until optically clear. *2.1M TOPSe.* Se (144 mg, 1.82 mmol) and TOP (797 mg, 2.15 mmol) were stirred and heated until optically clear. *0.2M Cd(oleate)<sub>2</sub>.* CdO (318 mg, 2.48 mmol), oleic acid (3.09 g, 10.94 mmol) and ODE (7.11 g, 28.16 mmol) were degassed under vacuum at 80°C for 60 min, refilled with Ar, and heated to 240°C until optically clear. *0.1M Cd(oleate)<sub>2</sub>-amine.* Dioctyl-amine (12.5 mL, 41.36 mmol) was degassed under vacuum at 80°C for 30 min, refilled with Ar, and transferred into another flask containing 0.2M Cd(oleate)<sub>2</sub> (12.5 mL). The mixture was stirred at 60°C for 20 min. *0.1M S<sub>8</sub>.* S<sub>8</sub> (79.0 mg, 2.47

mmol) and ODE (19.73 g, 78.13 mmol) were degassed under vacuum at 80°C for 30 min, refilled with Ar, heated to 180°C for 20 min until optically clear, and allowed to cool to room temperature. **CdSe cores.** *Small ca. 1.9nm±0.2nm CdSe cores.* CdO (15.0 mg, 117 µmol), TMPPA (304 mg, 1.05 mmol) and ODE (4.00 g, 15.84 mmol) were degassed under vacuum at 80°C for 30 min, refilled with Ar, and heated to 300°C for 6 h until optically clear. The solution was heated to 325°C and 0.16M TOPSe/ODE (5.7 mL, 904 µmol) swiftly injected. After ~5 s, the mixture was allowed to cool to room temperature. *Large ca. 4.7 nm ± 0.6 nm CdSe cores.* Dioctyl-amine (5 mL, 16.55 mmol) was degassed under vacuum at 80°C for 30 min, then refilled with Ar. 2.1M TOPSe (0.15 mL, 315 µmol) was added, and the temperature increased to 300°C. After 5 min, 0.2M Cd(oleate)<sub>2</sub> (1.5 mL, 300 µmol) was quickly injected and the temperature adjusted to 280°C. After 10 min, the mixture was allowed to cool to room temperature. Final CdSe cores were washed twice just prior to shell-growth by precipitation with 4:1 (v/v) acetone-methanol mixture and centrifugation at 4,200 rpm for 10 min. **CdSe/nCdS core/shells (n=1-20).** Freshly made CdSe was dissolved in hexane (5 mL, *ca.* 1.9nm cores) or toluene (5 mL, *ca.* 4.7nm cores). CdSe concentrations were determined from 1S peak at 490 nm (*ca.* 1.9nm cores) or 630 nm (*ca.* 4.7 nm cores) using updated extinction coefficients<sup>29</sup>. An aliquot containing  $7.5 \times 10^{-8}$  mol CdSe (10 µM initial concentration) was dried under vacuum at room temperature. ODE (4 mL, 12.5 mmol) and dioctyl-amine (3.8 mL, 12.57 mmol) were added. The mixture was degassed under vacuum at 80°C for 30 min, refilled with Ar, and heated to the necessary shell-growth temperature (*ca.* 1.9nm cores: 200°C 1-2 MLs, 230°C 3-6 MLs, 240°C 7-20 MLs; *ca.* 4.7 nm cores: 235°C 1-2 MLs, 245°C 3-20 MLs). Cd and S precursors were introduced in an alternating fashion using programmable syringe pumps, each followed by 15 min annealing or “wait” period. Cd precursor was injected first. The final mixture was allowed to cool to room temperature 15 min after last S injection. PL quantum yields (QY) were measured using well established procedures<sup>30</sup>.

**Non-blinking and thin-shelled QD modification.** Crude CdSe(1.9nm)/5CdS (**TSQD**, diameter = 4.8nm±0.8nm, PL<sub>max</sub> = 600nm, QY = 5%) and CdSe(4.7nm)/17CdS (**NBQD**, diameter = 14.5nm±1.6nm, PL<sub>max</sub> = 660nm, QY = 8.2%) were transferred to deionized water via surface ligand exchange with dihydrolipoic acid (DHLLA) following published protocol<sup>31</sup>, then washed once by precipitation with a 1:1 (v/v) acetone-methanol mixture and centrifugation at

4,200 rpm for 10 min. DHLA modified NBQDs and TSQDs were diluted in 10 mM borate buffer and placed under sonication for up to 1 h to reduce clustering. Neutravidin was then added to the DHLA modified NBQD and TSQD borate buffer solutions and incubated at room temperature for 1 h.

**Full-length kinesin motor proteins.** Dr. Will Hancock from The Pennsylvania State University kindly provided us the BL21 (DE3) *Escherichia coli* bacteria with the full-length His-tagged kinesin plasmid. Isopropyl B-D-1-thiogalactopyranoside (IPTG) was used to express kinesin in the *E. coli*. Kinesin was purified on a Ni column according to the published protocol.<sup>32</sup>

**Microtubule preparation.** Microtubules for NBQD studies were prepared in the following way. Taxol, GTP, and all tubulin were purchased from Cytoskeleton (Denver, CO). Tubulin aliquots were prepared with 86% natural bovine tubulin, 7% rhodamine tagged tubulin, and 7% biotinylated tubulin. Published protocol<sup>24,33</sup> was followed to produce microtubules biased with 12 protofilaments: 10  $\mu$ l BRB80 solution containing 4 mM MgCl<sub>2</sub>, 0.5 mM GTP, 10  $\mu$ M Taxol, and 9  $\mu$ M tubulin was incubated for 30 min at 37 C to produce microtubules of approximately 20  $\mu$ m in length. After 30 min, 100  $\mu$ l of BRB80 buffer with 10  $\mu$ M Taxol was added to stop microtubule nucleation. Microtubules were then resuspended in BRB0 solution supplemented with 10  $\mu$ M Taxol.

Microtubules for TSQD studies were prepared in the same manner with the exception of using 7% fluorescein tagged tubulin instead of 7% rhodamine tubulin. The fast photobleaching of the fluorescein allowed for a better signal to noise ratio with the diminished fluorescent signal associated with the TSQDs.

**Cover and microscope slide cleaning preparation.** New Corning (Lowell, MA) No.1 22x22 mm glass slides were cleaned following the described procedure. Slides were sonicated first in a solution of 18M $\Omega$  water and Conrad 70 detergent, twice in a solution of 18M $\Omega$ , and finally in 200 proof ethanol. Each sonication session lasted a minimum of 30 minutes.

The quartz microscope slides (SPI, West Chester, PA) were used for multiple gliding assay chambers. The slides were sonicated while submerged in toluene for 1 hour. The cover slides would then be removed using tweezers. The slides were again sonicated for 1 hour in toluene followed by 1 hour in ethanol. Final preparation was performed following the procedure for cleaning the Corning cover slides.

***In vitro* microtubule transport.** Two strips of double-sided tape 50  $\mu\text{m}$  thick (3M) were placed on a clean 25 $\times$ 51 mm quartz microscope slide (SPI, West Chester, PA) to use as spacers. A clean Corning (Lowell, MA) 22 $\times$ 22 mm glass slide was then placed on top of the tape to complete the chamber. A solution of BRB80 with the appropriate dilutions of microtubules and neutravidin modified NBQDs was allowed to incubate for approximately 10 min, while simultaneously a series of solutions was then flowed through the chamber to prepare the gliding assay. First, two chamber volumes of BRB80 solution containing 1.0 mg/ml casein (Sigma, St. Louis, MO) and 0.1 M  $\text{CaCl}_2$  (Fisher) was injected into the chamber and incubated at room temperature for 5 min. BRB80 solution containing 0.2 mg/ml casein, 0.2 mM MgATP, and kinesin displaced the previous solution in the chamber. After 5 min, BRB80 solution containing 0.2 mg/ml casein, 0.2 mM MgATP, 10  $\mu\text{m}$  Taxol, and NBQD modified microtubules flowed into the chamber and kept at room temperature for 5 min. The chamber was then rinsed with BRB80 solution containing 0.2 mg/ml casein and 0.2 mM MgATP. Finally, the chamber was filled with BRB80 solution containing 0.2 mg/ml casein, 1 mM Mg ATP, 10  $\mu\text{m}$  Taxol, and an oxygen scavenging system [50  $\mu\text{g}/\text{ml}$  glucose oxidase (Sigma), 4  $\mu\text{g}/\text{ml}$  catalase (Sigma), 1% (w/v) glucose (Sigma), and 0.1% (v/v)  $\beta$ -mercaptoethanol (Aldrich)] and placed under the microscope.

**Absolute axial position determination.** To prepare non-moving NBQD-modified microtubules in a quartz chamber the procedure described above was followed with the omission of the last solution. This allowed for the kinesin to hold the microtubules to the surface, but the microtubules were static due to the lack of ATP.

The localization precision in this experiment was dictated by the ability of our instrument to find and replicate the optimal incident illumination light angles and the consistency of the NBQDs to stay in the fluorescent emission state for prolonged periods of time. The automated calibration of the instrument was accomplished by using an in-house computer program that maximizes the signal to noise ratio of the region of interest (ROI) for each incident angle. More than 40 angles of incidence were imaged from subcritical angles to nearly  $90^\circ$  with intervals of approximately  $0.25^\circ$ . Before the data acquisition, the mirror position for each angle of incident light was set and both a rough-tune and a fine-tune position determination were performed. Each data point was the average of 5 measurements of the integrated fluorescence intensity of the entire particle taken with 50 ms exposure after subtracting the non-fluorescence background. The

points were plotted against the incident angle of the laser. Non-linear least squares (NLLS) fitting determined the vertical center of the NBQDs.

A thorough explanation and study of the uncertainty in SA-TIRFM axial direction super-localization can be found in our previous work.<sup>15</sup> To find the confidence interval for the calculated axial positions of the NBQDs, a  $\chi^2$  test was performed when  $\chi^2$  is defined as

$$\chi^2 = \sum_1^m \frac{1}{\sigma_m^2} [F_{\text{exp}} - F_{\text{theor}}]^2$$

where  $\sigma_m$  is the standard deviation of  $m$  measurements of the fluorescent intensity taken at each incident angle; and the experimental and theoretical fluorescent intensities are defined as  $F_{\text{exp}}$  and  $F_{\text{theor}}$ , respectively. To find the standard deviation of axial position we varied  $z$  close to its fitted value where  $\chi^2$  reaches a minimum,  $\chi^2(\text{min})$ . This is repeated for each fixed value of  $z$ , which reports another minimum  $\chi^2$  by floating the other parameters  $\chi^2(\text{par})$ .  $F_\chi$  statistics can estimate the confidence interval of  $z$  for the appropriate  $p$  parameters and  $\nu$  degrees of freedom:

$$F_\chi = \frac{\chi^2(\text{par})}{\chi^2(\text{min})} = 1 + \frac{\nu}{p} F(p, \nu, P)$$

where  $P$  is the probability that the value of  $F_\chi$  is due to random error. When  $P$  is smaller than 0.32, there is a 68% probability that the corresponding  $F_\chi$  consistent with the experimental values. This is the typical definition of one standard deviation.

$F_\chi$ , with our experimental fluorescence values, 2 parameters ( $p$ ), 40 degrees of freedom ( $\nu$ ), and a probability ( $P$ ) of 0.32 is 1.16. This means that when  $\chi^2(\text{par})$  is 1.16 times  $\chi^2(\text{min})$ , the corresponding  $z$  values are the standard deviation. If we take, for example,  $z_1$  from Figure 1B, 1.16 times  $\chi^2(\text{min})$  leads to 11.5 nm and 26.5 nm resulting in a standard deviation of 7.5 nm.

**Determination of blinking statistics.** Unmodified NBQDs were diluted to an appropriate concentration in toluene and dispersed across a Corning 22x22 mm coverslip and sandwiched by a Corning 18x18 mm coverslip. The toluene was then allowed to evaporate and the chamber was sealed with nail polish. DHLA-modified NBQDs were diluted in MilliQ water or 0.1% (v/v)  $\beta$ -mercaptoethanol and dispersed across a (3-aminopropyl)triethoxysilane (APTES) coated Corning 22 mm  $\times$  22 mm coverslip. The solution was then sandwiched by a Corning 18x18 mm coverslip and sealed with nail polish. Samples were viewed under TIRF conditions near the critical angle using an adjustable 75 mW maximum 488-nm argon continuous wave (CW) laser (Uniphase, San Jose, CA) as the excitation source. The sample was

allowed to settle for 30 min under the objective to reduce sample drift before imaging. Data was recorded with 100 gain in frame transfer mode with a 50 ms exposure time for 6000 continuous frames (5 min). ImageJ was used to analyze the data. A region of interest (ROI) was drawn around each individual quantum dot. Using the Track2 plugin the intensity through all 6000 frames was recorded. If the signal of the ROI was higher than the background signal plus  $3\sigma$ , the quantum dot was considered to be fluorescing or “on.” Statistics of the various samples were calculated using Microsoft Excel.

A comprehensive statistical analysis of the fluorescence intermittency for NBQDs, thin-shelled quantum dots (TSQDs), and commercial QDs (EviTag T2) was performed for a large sample size of individual particles (Table 1). Briefly, all samples were distributed across a microscope coverslip and excited by a 488 nm CW laser for 5 minutes. Data was recorded using an EMCCD with 50 ms exposure. Compared to the TSQDs and commercial QDs, unmodified NBQDs had vastly superior blinking statistics. A good comparison between traditional QDs and NBQDs can be held by looking at the sample fraction that emits for at least 80% of the acquisition time. A fraction of 37.5% of the commercial QDs emitted for at least 80% of the recorded time compared to unmodified NBQDs, of which 93.2% emitted. Even when the commercial QDs were analyzed in a solution of 1% (v/v) of  $\beta$ -mercaptoethanol (concentration appropriate for microtubule gliding assay), which is known to suppress fluorescent intermittency,<sup>4</sup> the fraction only increased to 60.1%. Without modification or a blinking suppressant environment, the NBQDs easily surpass the commercial QDs with regards to fluorescent intermittency. These statistics make the absolute positioning and dynamic tracking of NBQDs possible.

## References

1. Bruchez, M.; Moronne, M.; Gin, P.; Weiss, S.; Alivisatos, A. P. *Science* **1998**, 281, (5385), 2013-2016.
2. Han, M. Y.; Gao, X. H.; Su, J. Z.; Nie, S. *Nature Biotechnology* **2001**, 19, (7), 631-635.
3. Chan, W. C. W.; Nie, S. M. *Science* **1998**, 281, (5385), 2016-2018.
4. Hohng, S.; Ha, T. *Journal of the American Chemical Society* **2004**, 126, (5), 1324-1325.
5. Fomenko, V.; Nesbitt, D. J. *Nano Letters* **2008**, 8, (1), 287-293.



6. Chen, Y.; Vela, J.; Htoon, H.; Casson, J. L.; Werder, D. J.; Bussian, D. A.; Klimov, V. I.; Hollingsworth, J. A. *Journal of the American Chemical Society* **2008**, 130, (15), 5026-+.
7. Wang, X. Y.; Ren, X. F.; Kahen, K.; Hahn, M. A.; Rajeswaran, M.; Maccagnano-Zacher, S.; Silcox, J.; Cragg, G. E.; Efros, A. L.; Krauss, T. D. *Nature* **2009**, 459, (7247), 686-689.
8. Mahler, B.; Spinicelli, P.; Buil, S.; Quelin, X.; Hermier, J. P.; Dubertret, B. *Nature Materials* **2008**, 7, (8), 659-664.
9. Vela, J.; Htoon, H.; Chen, Y. F.; Park, Y. S.; Ghosh, Y.; Goodwin, P. M.; Werner, J. H.; Wells, N. P.; Casson, J. L.; Hollingsworth, J. A. *Journal of Biophotonics* **2010**, 3, (10-11), 706-717.
10. Huang, B.; Wang, W. Q.; Bates, M.; Zhuang, X. W. *Science* **2008**, 319, (5864), 810-813.
11. Juette, M. F.; Gould, T. J.; Lessard, M. D.; Mlodzianoski, M. J.; Nagpure, B. S.; Bennett, B. T.; Hess, S. T.; Bewersdorf, J. *Nature Methods* **2008**, 5, (6), 527-529.
12. Toprak, E.; Balci, H.; Blehm, B. H.; Selvin, P. R. *Nano Letters* **2007**, 7, (7), 2043-2045.
13. Vaziri, A.; Tang, J. Y.; Shroff, H.; Shank, C. V. *Proceedings of the National Academy of Sciences of the United States of America* **2008**, 105, (51), 20221-20226.
14. Pavani, S. R. P.; Greengard, A.; Piestun, R. *Applied Physics Letters* **2009**, 95, (2).
15. Wang, G. F.; Sun, W.; Luo, Y.; Fang, N. *Journal of the American Chemical Society* **2010**, 132, (46), 16417-16422.
16. Sun, W.; Xu, A. S.; Marchuk, K.; Wang, G. F.; Fang, N. *Jala* **2011**, 16, (4), 255-262.
17. Axelrod, D., Total Internal Reflection Fluorescence Microscopy. In *Biophysical Tools for Biologists, Vol 2: In Vivo Techniques*, Correia, J. J.; Detrich, H. W., Eds. 2008; Vol. 89, pp 169-221.
18. Ray, S.; Meyhofer, E.; Milligan, R. A.; Howard, J. *J. Cell Biol.* **1993**, 121, (5), 1083-1093.
19. Bohm, K. J.; Stracke, R.; Unger, E. *Cell Biology International* **2000**, 24, (6), 335-341.
20. Verma, V.; Hancock, W. O.; Catchmark, J. M. *Biomedical Microdevices* **2009**, 11, (2), 313-322.
21. Huang, Y.-M.; Uppalapati, M.; Hancock, W. O.; Jackson, T. N. *Biomedical Microdevices* **2007**, 9, (2), 175-184.
22. Friedman, D. S.; Vale, R. D. *Nature Cell Biology* **1999**, 1, (5), 293-297.



23. Kerssemakers, J.; Howard, J.; Hess, H.; Diez, S. *Proceedings of the National Academy of Sciences of the United States of America* **2006**, 103, (43), 15812-15817.
24. Nitzsche, B.; Ruhnaw, F.; Diez, S. *Nature Nanotechnology* **2008**, 3, (9), 552-556.
25. Ha, J. W.; Sun, W.; Wang, G. F.; Fang, N. *Chemical Communications* **2011**, 47, (27), 7743-7745.
26. Guo, Y.; Marchuk, K.; Sampat, S.; Abraham, R.; Fang, N.; Malko, A. V.; Vela, J. *The Journal of Physical Chemistry C* **2011**.
27. Saffarian, S.; Kirchhausen, T. *Biophysical Journal* **2008**, 94, (6), 2333-2342.
28. Guo, Y.; Marchuk, K.; Sampat, S.; Abraham, R.; Fang, N.; Malko, A. V.; Vela, J. *J. Phys. Chem. C* **2011**, 116, (4), 2791-2800.
29. Capek, R. K.; Moreels, I.; Lambert, K.; De Muynck, D.; Zhao, Q.; Vantomme, A.; Vanhaecke, F.; Hens, Z. *J. Phys. Chem. C* **2010**, 114, (14), 6371-6376.
30. Grabolle, M.; Spieles, M.; Lesnyak, V.; Gaponik, N.; Eychmueller, A.; Resch-Genger, U. *Anal. Chem.* **2009**, 81, (15), 6285-6294.
31. Clapp, A. R.; Goldman, E. R.; Mattoussi, H. *Nature Protocols* **2006**, 1, (3), 1258-1266.
32. Hancock, W. O.; Howard, J. *Journal of Cell Biology* **1998**, 140, (6), 1395-1405.
33. Ray, S.; Meyhofer, E.; Milligan, R. A.; Howard, J. *J. Cell Biol.* **1993**, 121, (5), 1083-1093.

## Figures

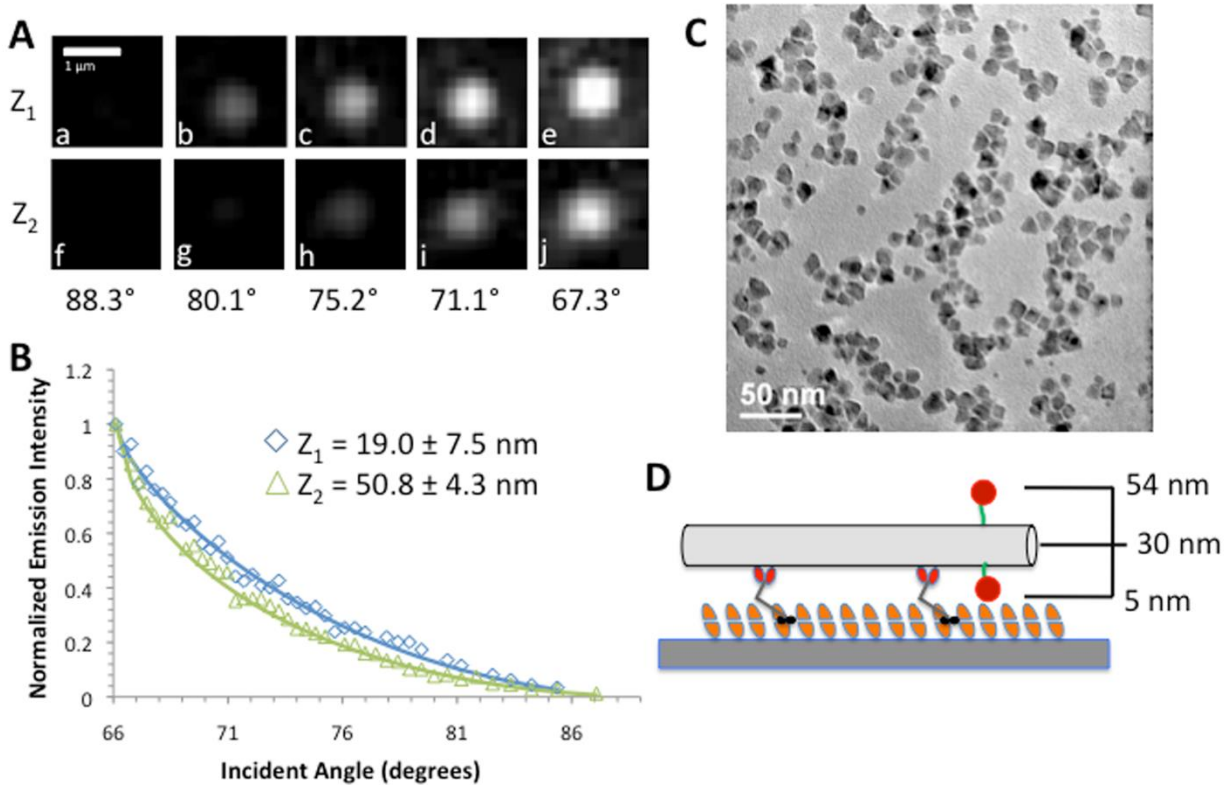


**Figure 4.** (A) Image set of NBQDs located at different axial positions on stationary microtubules. (a-e) Represent those for  $z_1$  at axial distance  $19.0 \pm 7.5 \text{ nm}$  and (f-j) represent those for  $z_2$  at axial distance  $50.8 \pm 4.3 \text{ nm}$ . (B) Fluorescence intensity decay curves for particle  $z_1$  and  $z_2$ . (C) TEM image of NBQDs CdSe(4.7nm)-17CdS. (D) Cartoon that represents important distances of the rotational-microtubule NBQD system. The figure is not drawn to the scale.

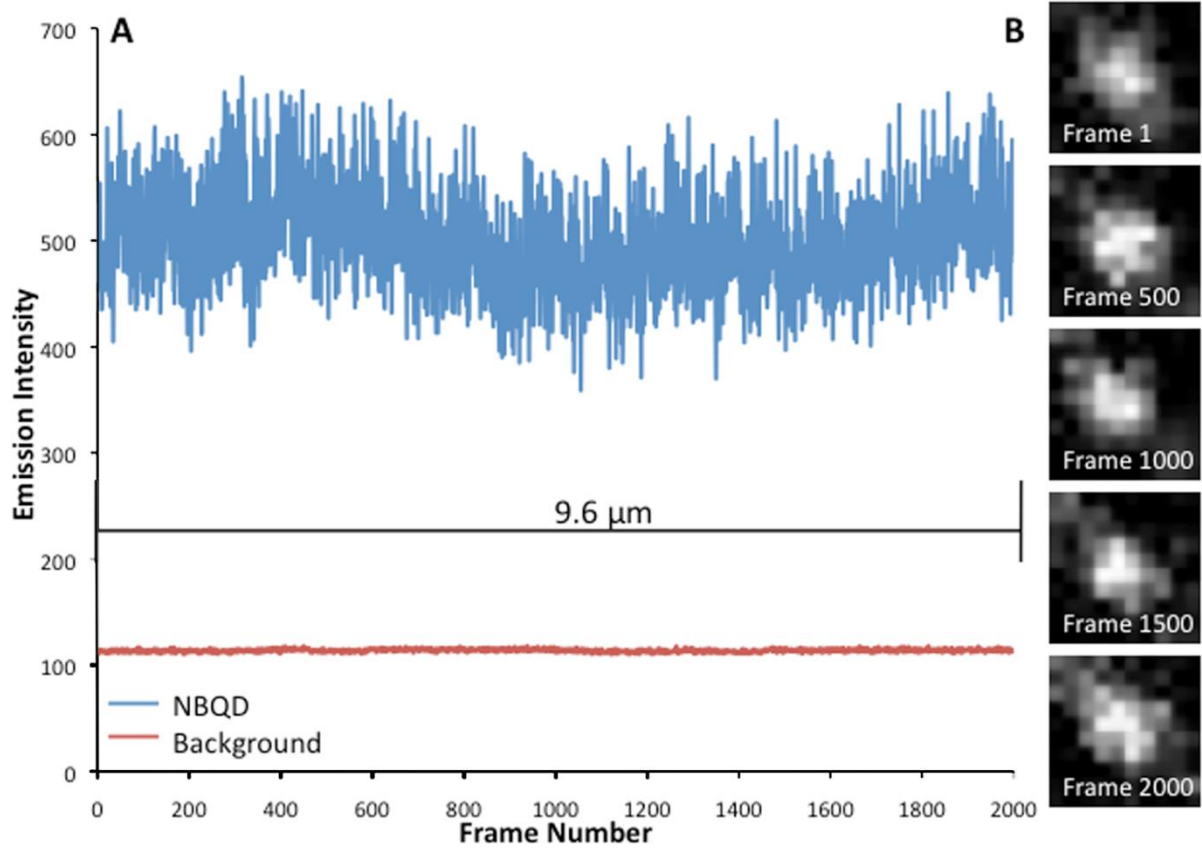


**Figure 5.** (A) Trace of NBQD attached to kinesin-propelled microtubule in gliding assay (50 ms exposure time). (B) Images of NBQD every 500 frames throughout the trace of (A).

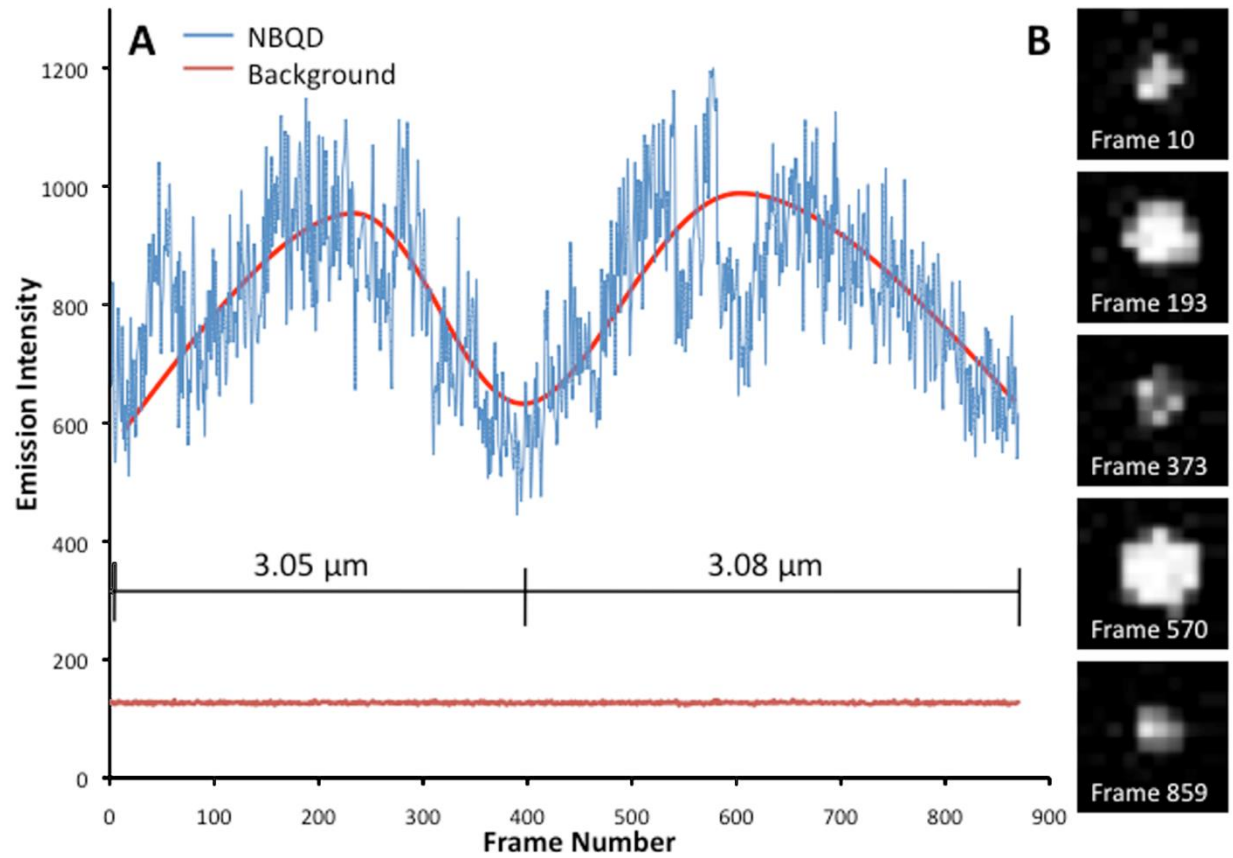


**Figure 6.** (A) Trace of NBQD attached to rotating microtubule followed for 2 full periods (50 ms exposure time). (B) Images of NBQD at frames corresponding to minimums and maximums of (A).

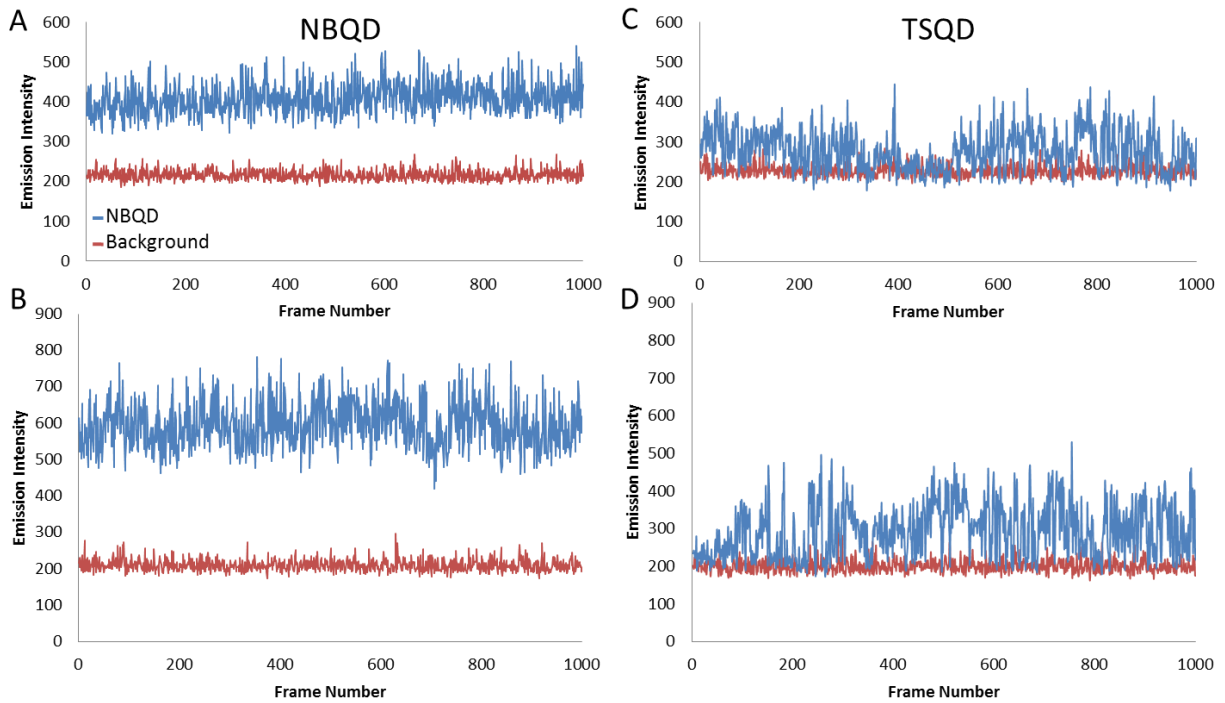


**Figure 7.** Trace (A) corresponds to a NBQD attached to a kinesin-propelled microtubule. (B) Corresponds to a NBQD on the quartz surface in a gliding assay. (C) Corresponds to a TSQD attached to a kinesin-propelled microtubule, while the trace in (D) is a TSQD on quartz surface in a gliding assay. All traces were captured using 50 ms exposure time.

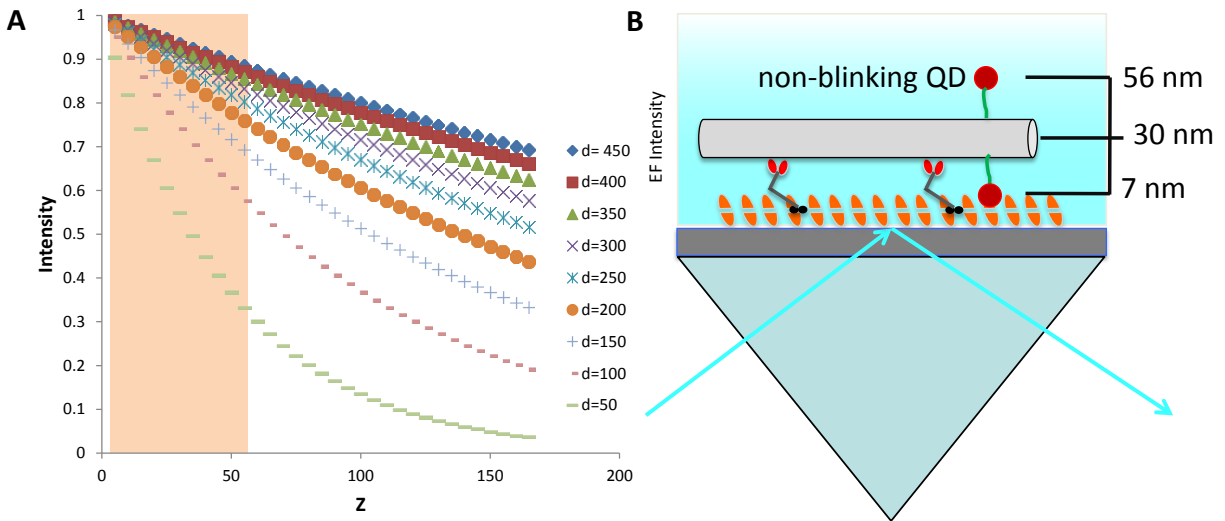


**Figure 8.** (A) Expected decay in signal intensity related to depth of EF. Shaded region relates to axial distance changes expected for microtubule system (7-56 nm). (B) Depiction of EF decay as the probe moves toward and away from the surface of TIR.

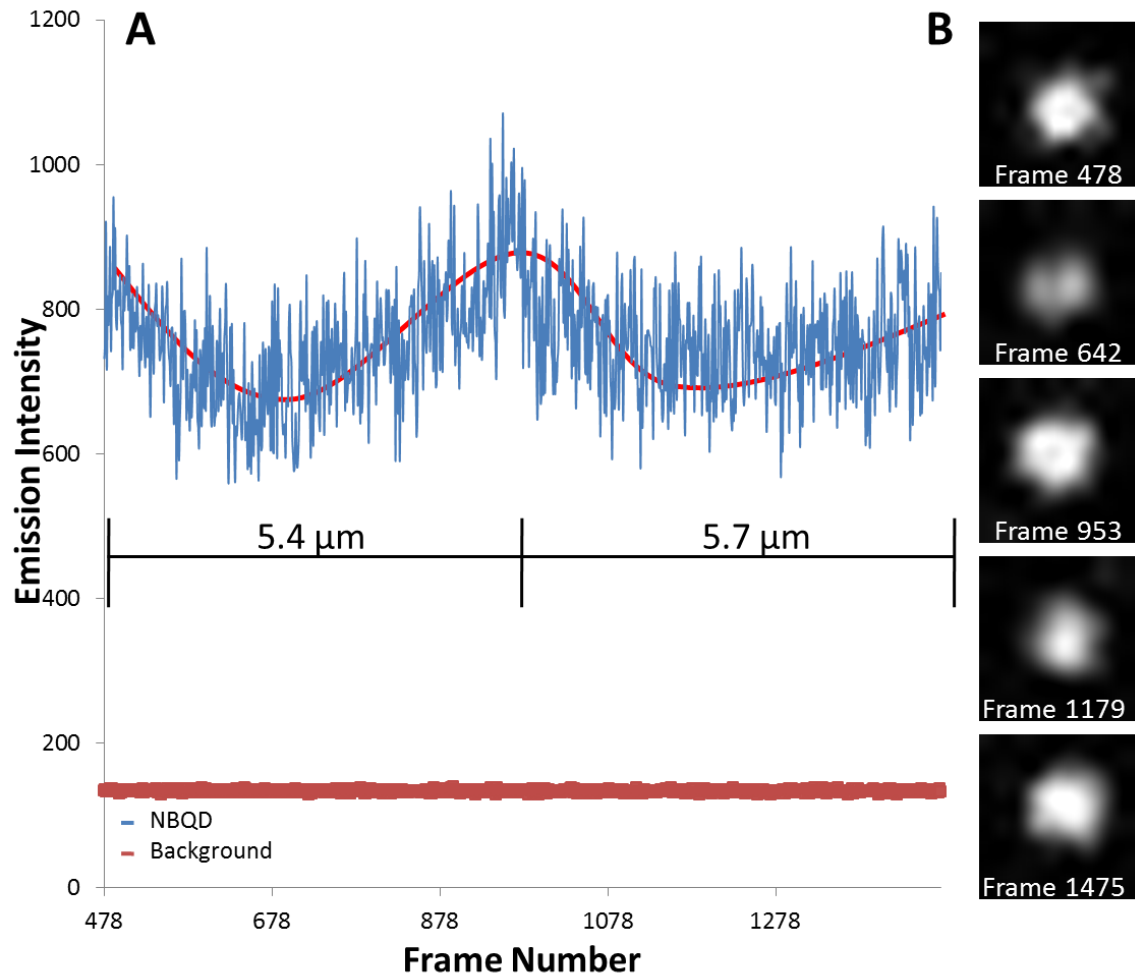


**Figure 9.** (A) Trace of NBQD attached to rotating microtubule followed for 2 full periods (50 ms exposure). (B) Images of NBQD at frames corresponding to maximums and minimums of (A).

**Table 1**

	<b>TSQDs (MilliQ)</b>	<b>EviTag (MilliQ)</b>	<b>EviTag (<math>\beta</math>ME)</b>	<b>NBQDs</b>	<b>NBQDs (MilliQ)</b>	<b>NBQDs (<math>\beta</math>ME)</b>
<b>Particles</b>	291	293	248	192	291	254
<b>Emit 98%</b>	0%	11.3%	22.2%	58.3%	69.1%	89.8%
<b>Emit 80%</b>	11.0%	37.5%	60.1%	93.2%	87.3%	95.3%
<b>Emit 60%</b>	30.9%	58.0%	76.6%	96.9%	94.5%	98.0%
<b>Average Number of “Blinks”</b>	282 $\pm$ 159	289 $\pm$ 188	273 $\pm$ 225	91 $\pm$ 136	69 $\pm$ 128	44 $\pm$ 126
<b>Average Length of Intermittency (seconds)</b>	0.84 $\pm$ .095	0.53 $\pm$ 0.84	0.26 $\pm$ 0.47	0.13 $\pm$ 0.12	0.23 $\pm$ 0.25	0.13 $\pm$ 0.14

Fluorescent intermittency statistics of various batches of QDs and NBQDs. Emit percentage refers to the fraction of the particles that emitted light equal to or greater than that percentage of length of time. Average number of “blinks” refers to the number of times an average particles switched between the “on” and “off” fluorescence state. Average length of intermittency is the average length a particle stayed in the “off” fluorescence state. Parenthesis below column title describe solution sample was imaged in. MilliQ refers to a solution of 18 $\Omega$  MilliQ water,  $\beta$ ME refers to 0.1% (v/v)  $\beta$ -mercaptoethanol in MilliQ water otherwise the sample was imaged in air.



## CHAPTER 3: THREE-DIMENSIONAL HIGH-RESOLUTION ROTATIONAL TRACKING WITH SUPER-LOCALIZATION REVEALS CONFORMATIONS OF SURFACE-BOUND ANISOTROPIC NANOPARTICLES

Kyle Marchuk, Ji Won Ha, and Ning Fang

Published in the Journal of Nano Letters<sup>§</sup>

### Abstract

The ability to directly follow three-dimensional rotational movement of anisotropic nanoparticles will greatly enhance our understanding of the way nanoparticles interact with surfaces. Herein we demonstrate dual-color total internal reflection scattering microscopy as a tool to probe the interactions of plasmonic gold nanorods with functional surfaces. By taking advantage of both the short and long axis surface plasmon resonance scattering enhancement, we are able to decipher both in-plane and out-of-plane gold nanorod motion relative to the sample surface with equally high resolution. In combination with super-localization through point spread function fitting, we overcome the four-quadrant angular degeneracy of gold nanorods in the focal plane of the objective and resolve conformations of surface-bound anisotropic nanoparticles in unprecedented detail.

### Introduction

Traditionally, the most commonly applied method for tracking rotational motions of sub-micron objects is fluorescence anisotropy using dye molecules or quantum dots (QDs) as orientation probes.<sup>1-3</sup> The most significant drawbacks to using organic dyes or QDs involve the stochastic intensity fluctuations and limited observation time due to the intrinsic photobleaching

---

<sup>§</sup> Reprinted with permission from Nano Letters, **2013**, 13 (3), 1245-1250. Copyright © Nano Letters

of both organic dyes<sup>4,5</sup> and quantum dots.<sup>6-8</sup> By exchanging these fluorescent probes with gold nanorods (AuNRs) the aforementioned hindrances are countered and additional advantages are gained, including geometrically controlled anisotropic optical properties,<sup>9</sup> large scattering and absorption cross-sections,<sup>10</sup> high-photostability,<sup>10,11</sup> and biocompatibility.<sup>12</sup>

A few techniques have been reported to resolve the in-plane orientation of AuNRs based on the polarization of light. These imaging schemes include dark-field (DF) polarization microscopy,<sup>9,13,14</sup> photothermal heterodyne imaging,<sup>15</sup> and differential interference contrast (DIC) microscopy.<sup>16-19</sup> These techniques monitor the intensity of orthogonally polarized light emanating from the AuNR to determine the orientation of the particle. While these are convenient techniques, they can only determine in-plane orientation information while out-of-plane (tilt) orientation remains difficult to resolve. This out-of-plane information is significant in complex biological systems.

Recently a technique called defocused orientation and position imaging (DOPI) has been utilized to determine the three-dimensional (3D) orientation of a fluorescent molecule or AuNR in a single image frame.<sup>20,21</sup> DOPI techniques are based upon the electron transition dipole approximation and the fact that the dipole radiation exhibits an angular anisotropy. Therefore, direct detection of the spatial distribution of the scattered or emitted field of single dipoles becomes possible when an aberration is deliberately applied to the imaging system, which, in these cases, is the out-of-focus image. Defocused imaging techniques carry significant drawbacks in that both signal and resolution are sacrificed to devolve 3D information. DOPI also does not always yield position accurately and the image needs to be alternated between defocused and focused for more precise position and orientation measurements.<sup>20</sup> Due to these limitations, DOPI is better suited for the characterization of stationary probes.

Another technique named focused orientation and position imaging (FOPI) is a scattering-based technique that overcomes some limitations of the DOPI technique.<sup>22</sup> Involving the effect of the supporting substrate on the far-field scattering patterns, the resulting image can be resolved into an absolute 3D orientation. The most significant limitation of this technique is the necessary interaction between the target particle and the substrate, which limits the potential applications.

Herein, we describe a technique that can dynamically track 3D orientation changes of multiple AuNRs without loss of signal or spatial resolution related to defocused images or that

relies on a specific interaction with the substrate. Using a dual-color total internal reflection scattering microscope (DC-TIRSM), we simultaneously tracked the orientation dependent intensity fluctuations of the long and short axis surface plasmon resonance (SPR) enhancement of AuNRs interacting with synthetic lipid membranes. The AuNRs are a model probe for studying particle interaction on engineered or biological surfaces due to their lateral and rotational dynamics being directly related to their binding status. With that in mind, the particles were also super-localized using point spread function (PSF) fitting to directly determine motion that may be lost within the diffraction limit. By combining super-localization with DC-TIRSM we are able to determine whether the particle is specifically bound to the surface, and moreover, we can determine where along the longitudinal axis the particle is bound and infer the 3D rotational motion the particle is undergoing.

## Results and Discussion

The AuNRs used in our experiments were  $25 \text{ nm} \times 60 \text{ nm}$  (aspect ratio 2.4) on average in size. Two absorption peaks with centers at 521 nm and 628 nm on the UV-vis spectrum correspond to the short axis surface plasmon resonance (SSPR) and the long axis surface plasmon resonance (LSPR), respectively.

The instrument we used is a scanning-angle total internal reflection fluorescence (SA-TIRF) microscope<sup>23,24</sup> modified for use as a DC-TIRSM (Fig. 1a). Our prism-based DC-TIRSM consists of a 647 nm continuous wave (CW) linearly polarized laser directed and focused through a series of optics before resulting in TIRS under the microscope objective. A symmetrical series of optics directed and focused a 532 nm CW linearly polarized laser on the opposing side of the microscope. The 647 nm and 532 nm laser lines are chosen to correspond to the LSPR and SSPR, respectively.

As is well understood, when the longitudinal axis of a AuNR rotates with respect to the polarization direction of the incident light at a wavelength within its LSPR enhancement, periodic changes in scattering signal will occur. This holds true for the SSPR as well. Therefore, AuNR orientation changes in the sample plane (azimuth angle,  $\psi$ ) can be tracked using polarized light that propagates parallel to the prism surface (s-pol), while out-of-plane orientation changes (elevation angle,  $\theta$ ) can be tracked utilizing the long axis of the AuNR and its interaction with polarized light propagating perpendicularly to the prism surface (p-pol). The scattering

intensities from both SSPR and LSPR interactions can be recorded simultaneously using a dual-wavelength imaging system. Fig. 1b and 1c portray polarized light propagation direction and AuNR geometry, respectively.

To demonstrate the simultaneous dynamic tracking of LSPR and SSPR orientation changes, we recorded AuNRs landing on a lipid bilayer. The AuNRs were surface-modified with transferrin, which produced a net negative charge to interact with net positively charged 1,2-dioleoyl-3-trimethylammonium-propane (DOTAP) infused 1-palmitoyl-2-oleoyl-*sn*-glycero-3-phosphocholine (POPC) lipids. As the AuNRs were injected into a lipid containing quartz chamber, we first used s-pol 647 nm and s-pol 532 nm laser lines to illuminate the sample under TIRS from opposing sides. Movies of 1000 frames a piece at 30 ms exposure in frame transfer mode were collected after the injection of AuNRs into the lipid modified quartz chamber. Since the SPR enhancement between the long and short axis occurs out-of-phase by 90°, we expected to see anti-correlated traces between the 647 nm and 532 nm channels. As seen in Fig. 2a, two nearly perfect anti-correlated (correlation coefficient: -0.9015) traces can be seen describing a 90° out-of-phase system. The resulting calculated angles were also in good agreement.

Recording the same AuNR, the 647 nm laser was then switched to p-pol illumination with the addition of a half-wave Fresnel rhomb (FR) placed in the beam path. The implementation of the FR saw the correlation coefficient change to -0.2479 with the loss of the completely anti-correlated traces into segmentation of anti-correlated, correlated, and non-correlated traces depicted in Fig. 2b, thus indicating the observation of out-of-plane movement. Correlation coefficients were calculated using a full 1000 frames before and after the FR was placed in the beam path. The full comparison can be seen in Fig. 6.

The coordinate system for the in-plane azimuth and elevation angle can be seen in Fig. 1c. Both the azimuth and elevation angles can be calculated from the normalized intensity with relative simplicity. When the longitudinal axis of the AuNR is positioned parallel to the direction of propagation for the 532 nm s-pol laser, the SSPR is maximally excited producing its most intense scattering. SSPR scattering intensity is at its minimum when the longitudinal axis is perpendicular to the incoming s-pol light. A  $\cos^2\psi$  fitting is used to calculate the remaining angles. Due to the nature of the squared cosine fitting a four-fold degeneracy remains in assigning absolute angles.

A similar approach is taken to assigning elevation angles. A AuNR with its longitudinal axis lying flat upon the surface is considered to have a minimum intensity when illuminated by the 647 nm p-pol laser, while a vertical position will achieve maximum LSPR excitation. A  $\sin^2\theta$  fitting of the normalized intensity calculates the rest of the angles.

To most accurately assign the maximum and minimum intensities, each AuNR is recorded from the initial point of surface interaction through many thousands of frames. It should also be emphasized that this is the first technique to resolve the elevation angle with a high angular resolution comparable to that for the azimuth angle.

Fig. 3 shows two 1000-frame segments for a neutravidin modified AuNR interacting with biotin infused POPC lipid membranes (full trace found in Fig. 7). While many AuNRs quickly became laterally and rotationally “frozen” when they interacted with the membrane, a significant fraction showed fluctuations for both in-plan and out-of-plane intensities. As can be seen, the AuNR showed preference for a variety of conformations on the membrane surface. It is also possible for AuNRs to undergo segments of high and low activity of orientation movement. Examples of this can be seen within the first 1000 frames of Fig. 3 where the particle originally starts with what appears to be random motion before achieving an orientation that it stays in the last ~150 frames. One might suspect that a particle will go through random conformational changes before it reaches a final resting orientation. This particular particle will achieve conformations in which it will stay in for several seconds before it once again goes through a phase of rapid motions. Fig. 7 depicts the undergoing of this motion several times throughout the observation. The dynamic nature of the lipid bilayer may cause a disturbance to the AuNR thus forcing motion upon it.

The first frames in Fig. 3 seem to be the result of the AuNR undergoing random motions while attached to the membrane. Without knowing the four quadrant position of the center of scattering, it is impossible to get the full picture of what motions the AuNR is undertaking. To break the four quadrant degeneracy of the in-plane rotation, we invoked a method of super-localizing the AuNRs as they underwent conformational changes. Using a MATLAB script, the scattering intensities of AuNRs were fit to a Gaussian PSF with sub-pixel localization. Localization precision was calculated using a method similar to Yildiz, et al.<sup>25</sup> and achieved a standard deviation of 1.62 nm at the current temporal resolution of 30 ms (see Methods for a detailed discussion on localization precision). Looking at the first 100 frames in the trace from

Fig. 3, what appears to be a random array of azimuth and elevation angles is observed. Plotting out the super-localized positions a pattern emerges (Fig. 4a). This oval shape suggests the AuNR is spinning around a central point. Considering the AuNR has an average size of  $25 \text{ nm} \times 60 \text{ nm}$ , the super-localization suggests the particle is tethered at the end of its long axis allowing a high degree of motion. Fig. 4a shows the AuNR profiles along with the neutravidin binding to biotin represented by a  $5.8 \text{ nm}$  circle.<sup>26</sup> Using the super-localization in tandem with the angle determination allows us to break the degeneracy for the in-plane angle determination.

A second example of an anchored AuNR can be found in Fig. 8. The particle was considered to start interacting with the surface in frame 711 and surface bound in frame 791 based on changes in its location. This trace suggests a much more subdued particle with regards to its orientation changes. Following the intensity after frame 2500 we can see that the elevation angle is relatively consistent while the azimuth angle shows some changes. The super-localization shows movement that is constricted by a shortened axis of rotation (Fig. 4b). The radius of travel suggests the AuNR is bound  $\sim 7 \text{ nm}$  from the end of its long axis.

Due to a more constricted geometry, the closer the binding point is to the center of the long axis, the less out-of-plane motion we predict. We expect the lipid layer will limit what elevation angle the nanorod can achieve since a AuNR bound  $7 \text{ nm}$  from one end can only achieve an elevation angle of  $53.7^\circ$  before the lipid surface sterically hinders motion. Examining the trace we see that the elevation angle is relatively low throughout the series and only reaches a calculated angle of  $53.5^\circ$  once throughout the trace.

Some AuNRs are not bound to the membrane and are relatively free to diffuse about the surface. These particles are distinguishable in our super-localization technique due to the distances they travel across the surface. Interestingly, we have found that some AuNRs seem to have preferred conformations that reach distances up to several axial lengths away from each other as depicted in Fig. 5. These are not just stops in the lengthy procession of diffusion, but are locations in which the AuNR will return time and time again. Without the super-localization combined with the dual-axis angular calculations, the lateral motions would have been lost within the diffraction limit. A more in depth study is needed to understand how non-covalently bound nanoparticles interact with a lipid bilayer at the nano-domain level.

## Conclusion

In summary, we have presented a method in which we can simultaneously track 3D orientation changes in anisotropic plasmonic nanoparticles while super-localizing their lateral motions across a surface. The method requires no special aberration placed in the light path, thus no spatial resolution is sacrificed, and there is no need for any substrate/particle interaction allowing for its invocation into studies requiring various particles and surfaces. Therefore, we expect this method to become widely useful in membrane and other biological studies in which out-of-plane particle motion is of great interest. We also foresee its potential use in surface patterning.

## Methods

**Dual-color total internal reflection scattering microscope.** The apparatus was built around a Nikon Optihot-2 microscope. The original microscope stage was removed and replaced with a Sutter MP-285 motorized three-dimensional translational stage (Novato, CA). A homemade prism holder was attached to the Sutter stage, which held an equilateral Bk7 prism (Melles Griot, Albuquerque, NM). An adjustable 40 mW maximum 647-nm continuous wave (CW) laser (CUBE, Coherent, Santa Clara, CA) and 50 mW 532-nm CW laser (Uniphase, San Jose, CA) were used as the excitation sources. A symmetric series of optics and motorized stages on both sides of the microscope were set up to direct the laser paths beneath the objective. First the laser beams were directed to a periscope and through a Uniblitz mechanical shutter (model LS2Z2, Vincent Associates, Rochester, NY). To switch between s- and p-pol illuminations a half-wave Fresnel rhomb (FR600HM, Thorlabs, Newton, NJ) was placed into or taken out of the beam path. The beams then passed through focusing lenses (15-cm focal length) and on to the mirror of a galvanometer optical scanner (model 6220H, Cambridge Technology, Cambridge, MA). The focusing lens was used to control the laser illumination size under the objective, while the mirror galvanometer was used in conjunction with a motorized linear stage (model MAA-PP, Newport, Irvine, CA) to direct the laser beam through the equilateral prism to the solid-liquid interface. Scattered light was collected by a Plan Fluor 100x/NA 1.3 oil immersion objective and directed into a Dual-View imaging system (Photometrics, Tucson, AZ) before reaching the Andor iXon<sup>EM</sup>+ 897 camera (Belfast, Northern Ireland; 512 × 512 imaging array, 16 μm × 16 μm pixel size). Within the Dual-View a Stoptone 532-nm notch filter (Semrock, Rochester, NY) was



placed in the long pass path, and a Coherent 560-nm short pass (Coherent, Santa Clara, CA) was placed in the short pass path.

**Gold nanorod surface modification.** AuNRs (25 nm × 60 nm, aspect ratio 2.4) were purchased from Nanopartz (Salt Lake City, UT). AuNR solution was first centrifuged for 6 min at 5500 rpm and the supernatant decanted. The AuNRs were then re-suspended in 18-M $\Omega$  Milli-Q water. N-hydroxylsuccinimide-polyethylene glycol (NHS-PEG) disulfide linker (Sigma-Aldrich) in DMSO (2 mg/ml) was added to the solution and placed on a rotating rack for 90 min. The solution was again centrifuged for 6 min at 5500 rpm and the supernatant removed. Solution was suspended in 18-M $\Omega$  Milli-Q water and transferrin (2 mg/mL) was added. The AuNRs were then placed on the rotation rack for a minimum of 2 hours before use.

Neutravidin modified AuNRs were similarly prepared. AuNR solution was centrifuged at 5500 rpm for 6 min and the supernatant decanted. The AuNRs were suspended in Milli-Q water and NHS-PEG disulfide linker in DMSO (2 mg/mL) was added before being placed on a rotation rack for 90 min. Solution was then diluted to the appropriate AuNR concentration with Milli-Q water before neutravidin in PBS (2 mg/mL) was added. Solution was placed on the rotation rack for a minimum of 2 hours before use.

**Synthetic Lipid Bilayers.** Lipid films composed of 1-palmitoyl-2-oleoyl-*sn*-glycero-3-phosphocholine (POPC, Avanti Polar Lipids) and biotin infused 1,2-dioleoyl-*sn*-glycero-3-phosphoethanol-amine (biotin-DOPE) were prepared following the published procedure<sup>14</sup> with the exceptions that no Texas-Red DHPE was used and the substrate was a quartz micro-chamber (described below). A 10% 1,2-dioleoyl-3-trimethylammonium-propane (DOTAP) in POPC was prepared following the same procedure as the biotin-DOPE.

**Imaging AuNRs under TIRS microscope.** Two strips of double-sided tape 50  $\mu$ m thick (3M) were placed on a clean 25 mm × 51 mm quartz microscope slide (SPI, West Chester, PA) to use as spacers. A clean Corning (Lowell, MA) 22 mm × 22 mm glass slide was then placed on top of the tape to complete the chamber. Lipid solution was flowed into the chamber and incubated at room temperature for 20 min. The chamber was rinsed with two chamber volumes of PBS buffer (pH 7.4) followed by two chamber volumes of 1 mg/ml BSA solution. The chamber was then set upon the prism and the microscope was focused. The chamber and sample was then allowed to settle for 5 min, which minimized the drift during sample acquisition.



After the 5 min passed, one chamber volume of modified AuNR solution was injected into the chamber. Immediately, signal acquisition was started. For each chamber, 20 spools of 1000 frames exposed for 30 ms in frame transfer mode were recorded sequentially. This provided 10 min of recording the same area under the objective.

The exposure time of 30 ms was chosen to both maximize the recordable area under the objective and the localization precision. The Andor iXon<sup>EM</sup>+ 897 camera (Belfast, Northern Ireland; 512 x 512 imaging array, 16  $\mu\text{m}$  x 16  $\mu\text{m}$  pixel size) has a maximum recording rate of 30 ms in frame transfer mode for full-area recording. The larger the viewing the more likely we were to observe landing events upon the lipid membrane. Since the imaging area was already split by the dual-view system, any increase in recording speed came with a drastic reduction in viewing area. Increasing the frame rate would also have negatively impacted the localization precision by decreasing the number of photons collected.

**Angle Determination.** Intensity traces for individual particles were generated for both SSPR and LSPR. A custom MATLAB script was written that calculated the sum of the 10 brightest pixels in a designated region of interest (ROI). These values were recorded prior to the AuNR landing event until the final spool was captured or 2000 frames after the AuNR stopped showing significant signal fluctuation. Background subtraction was performed by first calculating the average local background intensity using a 10x10 pixel area, multiplying that average by ten, and subtracting that value from the calculated signal.

The minimum intensity of the SSPR channel was assumed to be the signal of the AuNR angled 90° from laser propagation direction. The minimum intensity from the LSPR channel was assumed to result from an elevation angle of 0°. These minimum values were then subtracted from the background adjusted intensity. Normalization is performed for both SSPR and LSPR intensities using the resulting maximum. Fitting was performed using a simple  $\cos^2\psi$  for SSPR and  $\sin^2\theta$  for LSPR.

**Super-Localization Precision Determination.** The precision of localization of the AuNRs were determined using a previously described method.<sup>25</sup> Briefly, using a MATLAB script, the scattering intensities of AuNRs were fit to a Gaussian PSF with sub-pixel localization. First a nanoparticle that had landed and exhibited a bright and stable intensity was localized. A secondary particle that was also exhibiting a stable signal was then localized and the positions were then compared to each other to remove any subtle vibrations that may have occurred in the

sample. The stability of the particle location was then calculated for 100 frames and the resulting standard deviation was the calculated precision achieving 1.62 nm.

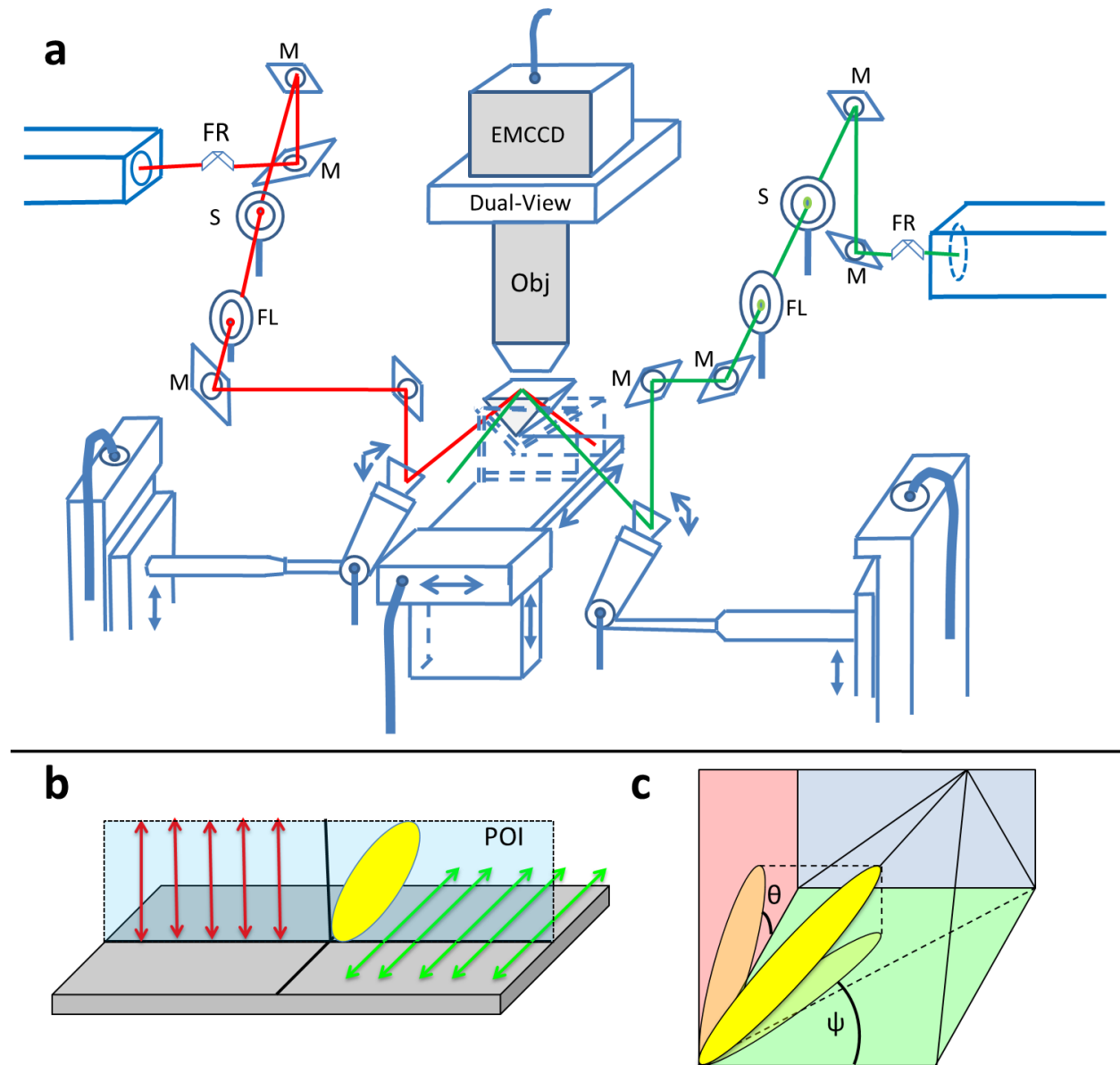
It should be noted that this precision determination was performed on a random AuNR that bound to the lipid surface early in the experiment. Since Gaussian PSF fitting is determined in part by the signal strength, we expect our super-localization to be both negatively and positively affected by fluctuating signal intensity inherent to the experimental observations.

## References

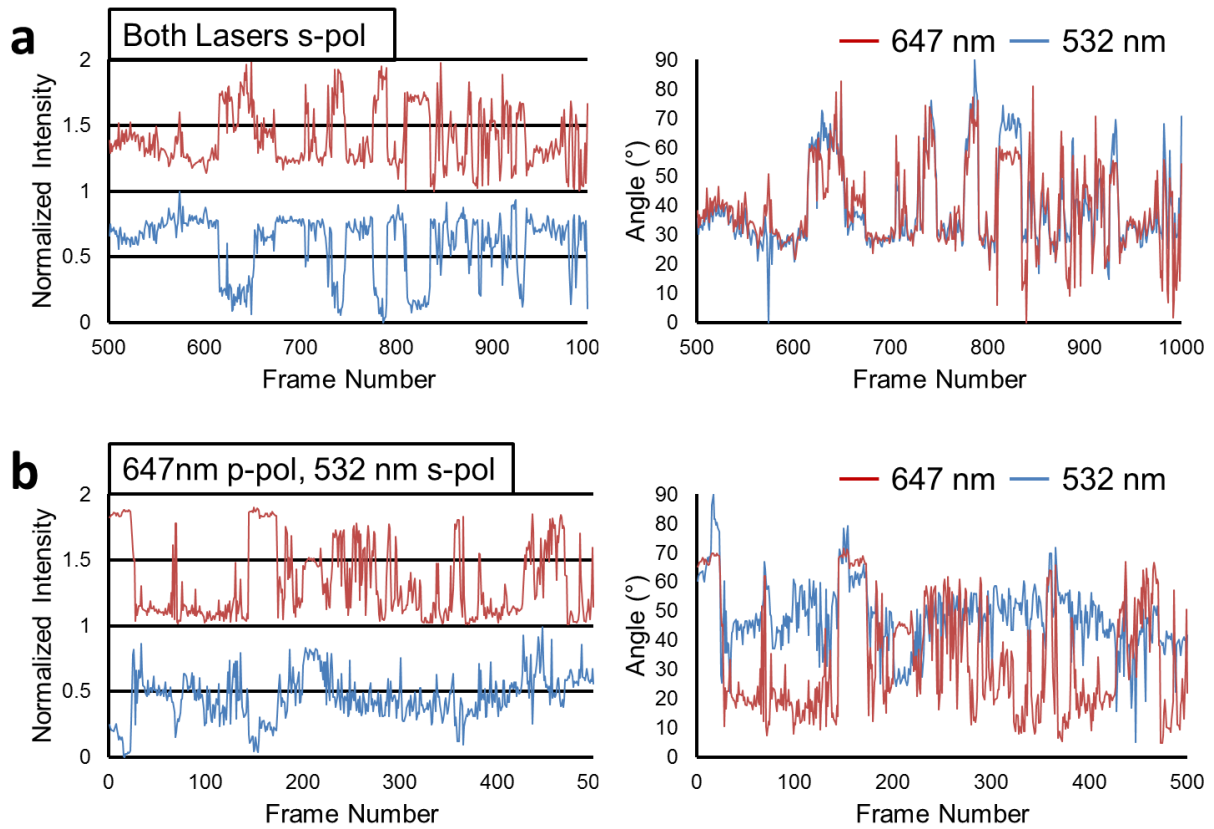
1. Forkey, J. N.; Quinlan, M. E.; Goldman, Y. E. *Prog. Biophys. Mol. Biol.* **2000**, 74, (1-2), 1-35.
2. Khatua, S.; Guerrero, J. M.; Claytor, K.; Vives, G.; Kolomeisky, A. B.; Tour, J. M.; Link, S. *Acs Nano* **2009**, 3, (2), 351-356.
3. Chung, I. H.; Shimizu, K. T.; Bawendi, M. G. *Proceedings of the National Academy of Sciences of the United States of America* **2003**, 100, (2), 405-408.
4. Moerner, W. E.; Orrit, M. *Science* **1999**, 283, (5408), 1670-+.
5. Xie, X. S.; Dunn, R. C. *Science* **1994**, 265, (5170), 361-364.
6. Nirmal, M.; Dabbousi, B. O.; Bawendi, M. G.; Macklin, J. J.; Trautman, J. K.; Harris, T. D.; Brus, L. E. *Nature* **1996**, 383, (6603), 802-804.
7. Kuno, M.; Fromm, D. P.; Hamann, H. F.; Gallagher, A.; Nesbitt, D. J. *Journal of Chemical Physics* **2001**, 115, (2), 1028-1040.
8. Kuno, M.; Fromm, D. P.; Gallagher, A.; Nesbitt, D. J.; Micic, O. I.; Nozik, A. J. *Nano Letters* **2001**, 1, (10), 557-564.
9. Sonnichsen, C.; Alivisatos, A. P. *Nano Letters* **2005**, 5, (2), 301-304.
10. Sperling, R. A.; Rivera gil, P.; Zhang, F.; Zanella, M.; Parak, W. J. *Chemical Society Reviews* **2008**, 37, (9), 1896-1908.
11. Wu, X. Y.; Yeow, E. K. L. *Nanotechnology* **2008**, 19, (3).
12. Murphy, C. J.; Gole, A. M.; Stone, J. W.; Sisco, P. N.; Alkilany, A. M.; Goldsmith, E. C.; Baxter, S. C. *Accounts of Chemical Research* **2008**, 41, (12), 1721-1730.
13. Xiao, L. H.; Qiao, Y. X.; He, Y.; Yeung, E. S. *Journal of the American Chemical Society* **2011**, 133, (27), 10638-10645.

14. Pierrat, S.; Hartinger, E.; Faiss, S.; Janshoff, A.; Soennichsen, C. *Journal of Physical Chemistry C* **2009**, 113, (26), 11179-11183.
15. Chang, W. S.; Ha, J. W.; Slaughter, L. S.; Link, S. *Proceedings of the National Academy of Sciences of the United States of America* **2010**, 107, (7), 2781-2786.
16. Ha, J. W.; Sun, W.; Wang, G. F.; Fang, N. *Chem. Commun.* **2011**, 47, (27), 7743-7745.
17. Ha, J. W.; Sun, W.; Stender, A. S.; Fang, N. *Journal of Physical Chemistry C* **2012**, 116, (4), 2766-2771.
18. Wang, G. F.; Sun, W.; Luo, Y.; Fang, N. *Journal of the American Chemical Society* **2010**, 132, (46), 16417-16422.
19. Gu, Y.; Sun, W.; Wang, G. F.; Fang, N. *Journal of the American Chemical Society* **2011**, 133, (15), 5720-5723.
20. Toprak, E.; Enderlein, J.; Syed, S.; McKinney, S. A.; Petschek, R. G.; Ha, T.; Goldman, Y. E.; Selvin, P. R. *Proceedings of the National Academy of Sciences of the United States of America* **2006**, 103, (17), 6495-6499.
21. Li, T.; Li, Q.; Xu, Y.; Chen, X.-J.; Dai, Q.-F.; Liu, H.; Lan, S.; Tie, S.; Wu, L.-J. *Acs Nano* **2012**, 6, (2), 1268-1277.
22. Ha, J. W.; Marchuk, K.; Fang, N. *Nano Letters* **2012**, 12, (8), 4282-4288.
23. Sun, W.; Marchuk, K.; Wang, G. F.; Fang, N. *Analytical Chemistry* **2010**, 82, (6), 2441-2447.
24. Marchuk, K.; Guo, Y. J.; Sun, W.; Vela, J.; Fang, N. *Journal of the American Chemical Society* **2012**, 134, (14), 6108-6111.
25. Yildiz, A.; Forkey, J. N.; McKinney, S. A.; Ha, T.; Goldman, Y. E.; Selvin, P. R. *Science* **2003**, 300, (5628), 2061-2065.
26. Berndt, M.; Lorenz, M.; Enderlein, J.; Diez, S. *Nano Letters* **2010**, 10, (4), 1497-1500.

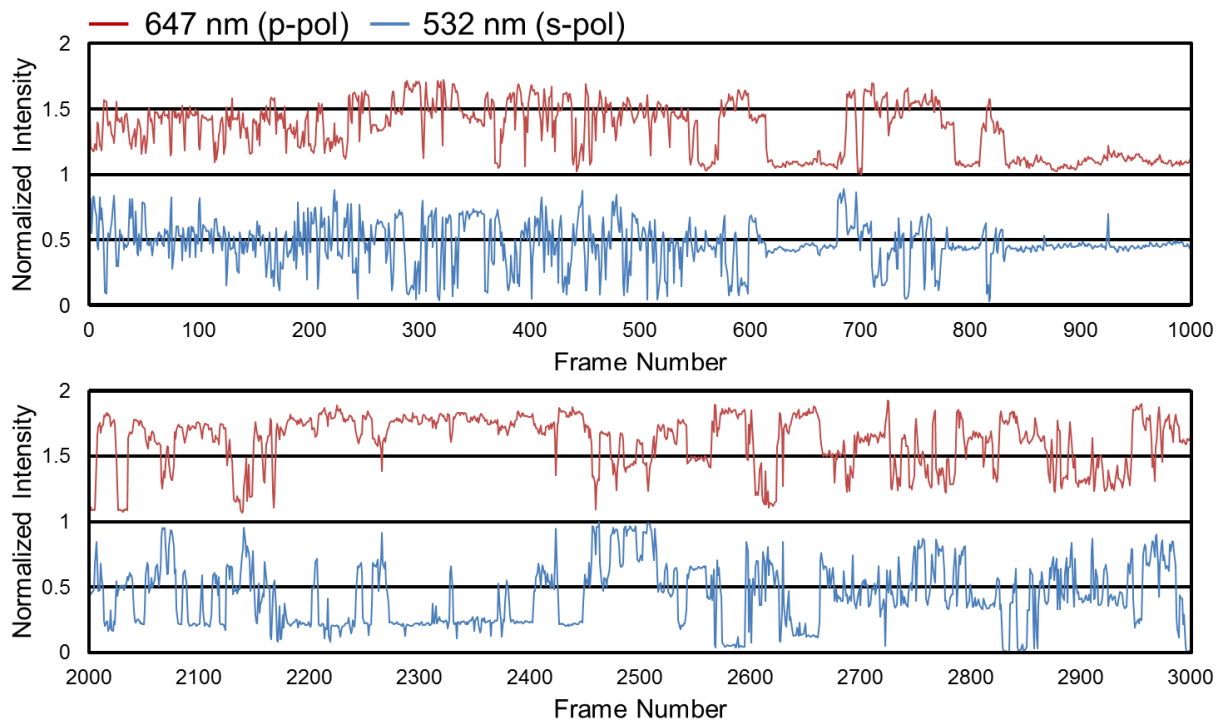
## Figures



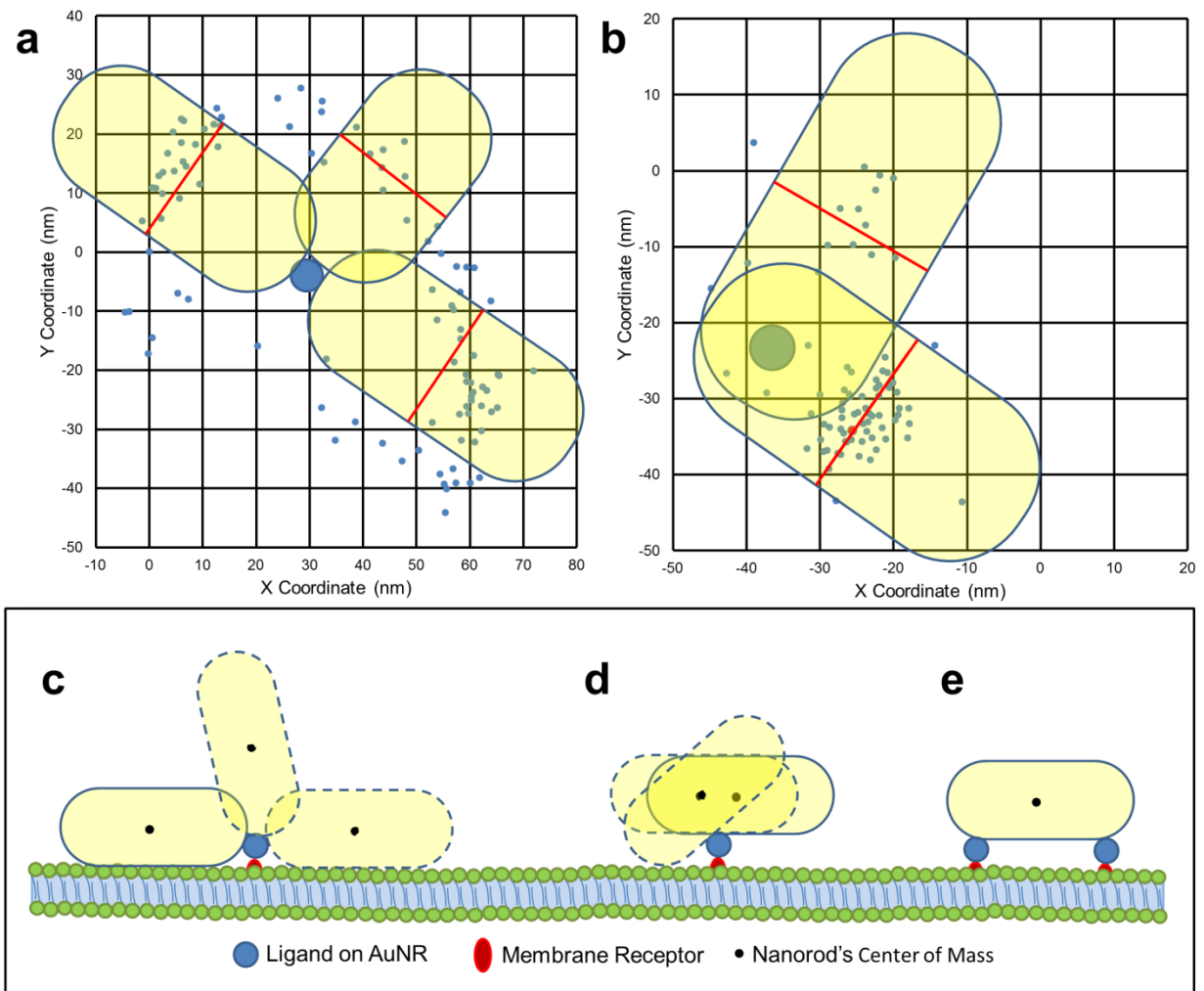
**Figure 1.** Visualizations for both the instrument and the particle geometry. **(a)** Scheme of DC-TIRSM illustrating laser geometry. **(b)** Representation of p (red) & s (green) laser polarization. **(c)** Example of azimuth and elevation angle and the corresponding AuNR projection used in angle calculations. FR: Fresnel rhombs, M: mirror, S: shutter, FL: focusing lens, Obj: objective, POI: plane of incidence,  $\psi$ : azimuth angle,  $\theta$ : elevation angle.



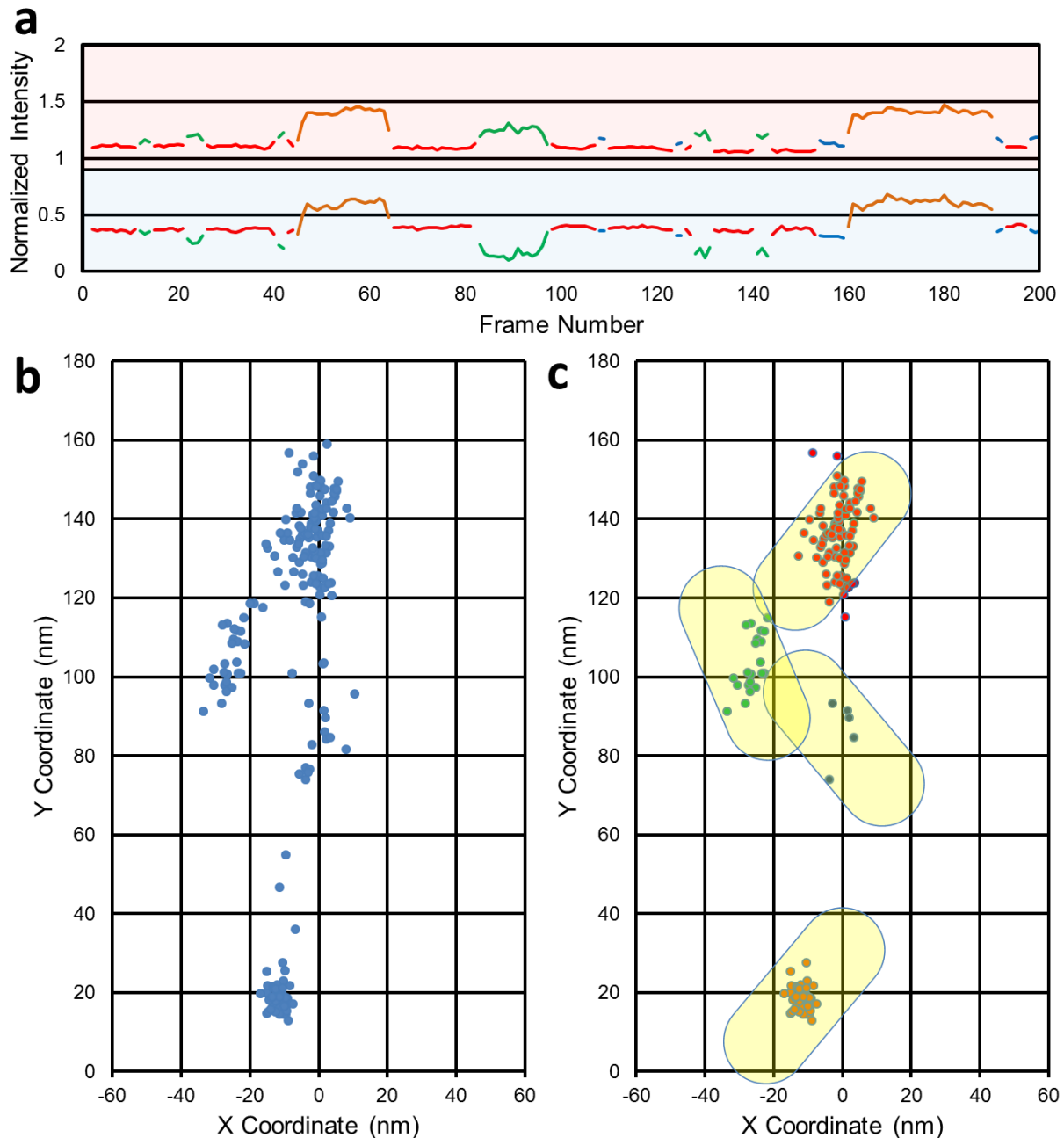
**Figure 2.** Effect of changing LSPR excitation from s-pol to p-pol. (a) Intensity (left) and calculated angle (right) traces when both lasers were set to s-polarization. (b) Intensity (left) and calculated angle (right) traces after the 647 nm laser was set to p-polarization.



**Figure 3.** Two 1000-frame segments taken from 16,000 frames recorded for this particular AuNR with long axis p-polarization and short axis s-polarization. Within the traces are examples of correlated, anti-correlated, and non-correlated intensities.

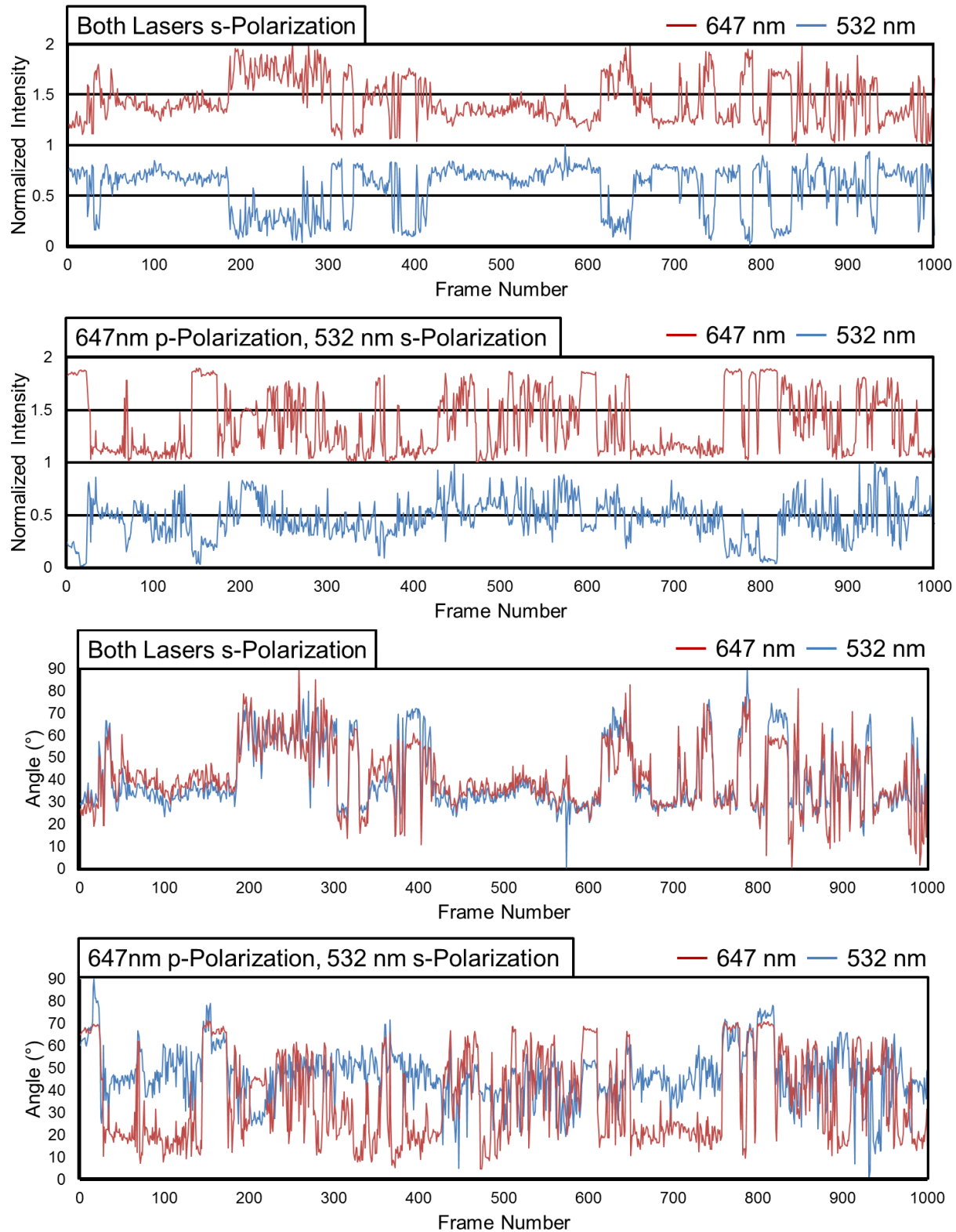


**Figure 4.** Examples of AuNRs bound to the lipid membrane at different points along the longitudinal axis. AuNR in (a) is bound at the end of the axis, while the AuNR in (b) is bound  $\sim 7$  nm along the axis. Blue circles correspond to size of neutravidin. (c-e) Examples of possible binding scenarios for AuNRs on lipid membranes. The number and position of binding sites directly influence the rotational dynamics of the particle.



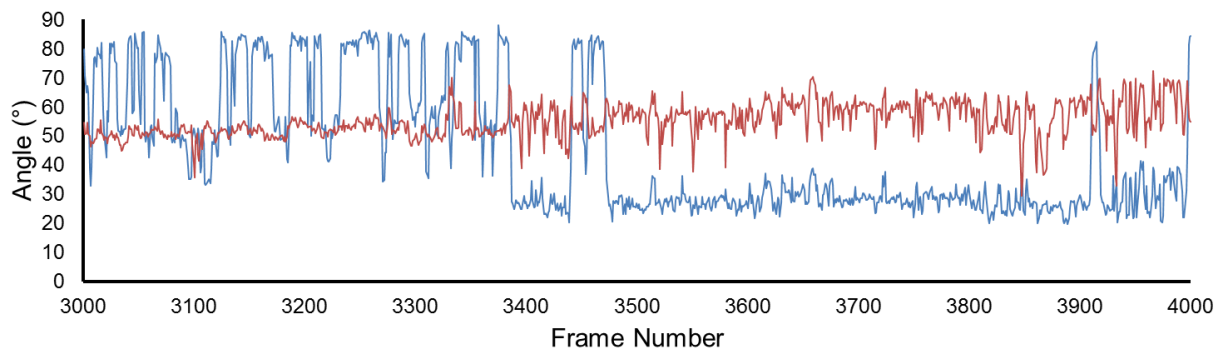
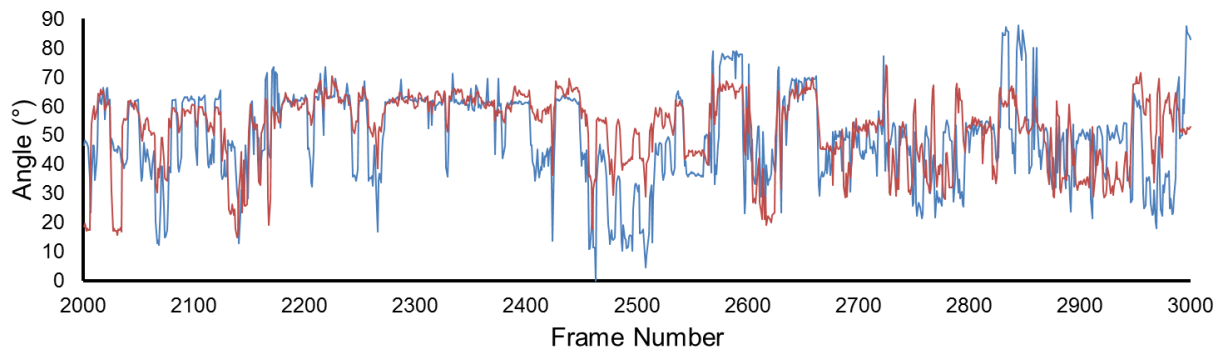
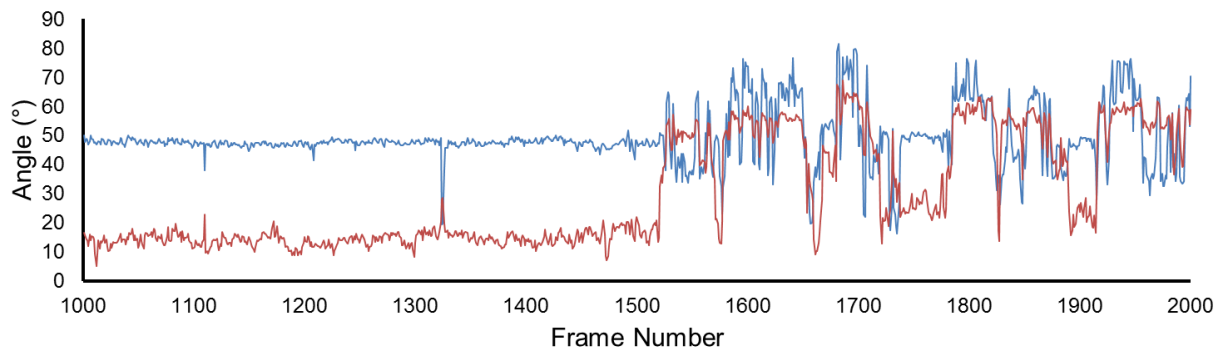
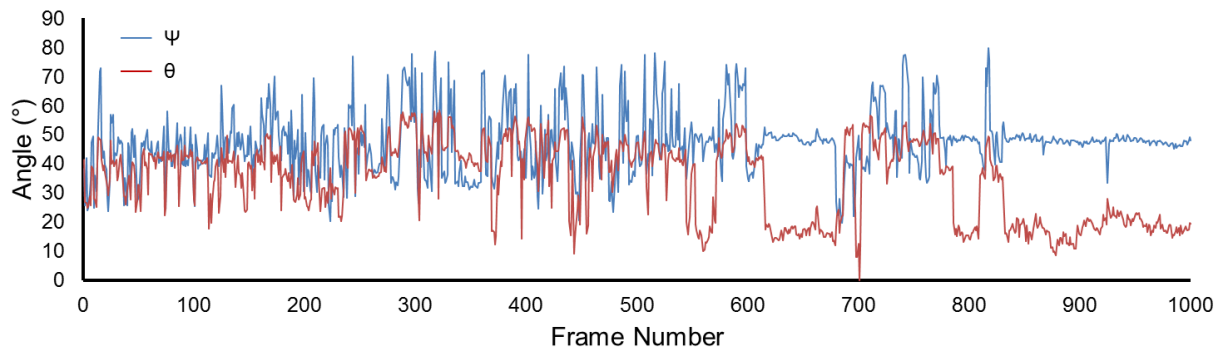
**Figure 5.** Example of the relation between the scattering intensities and the super-localized positions. **(a)** Intensity traces for out-of-plane (top) and in-plane (bottom) AuNR movements on lipid bilayer. **(b)** Super-localization position of trace in **(a)**. **(c)** The colors in trace **(a)** related to the corresponding colors in **(c)**. Positions corresponding to the “slopes” on the trace have been removed for clarity.

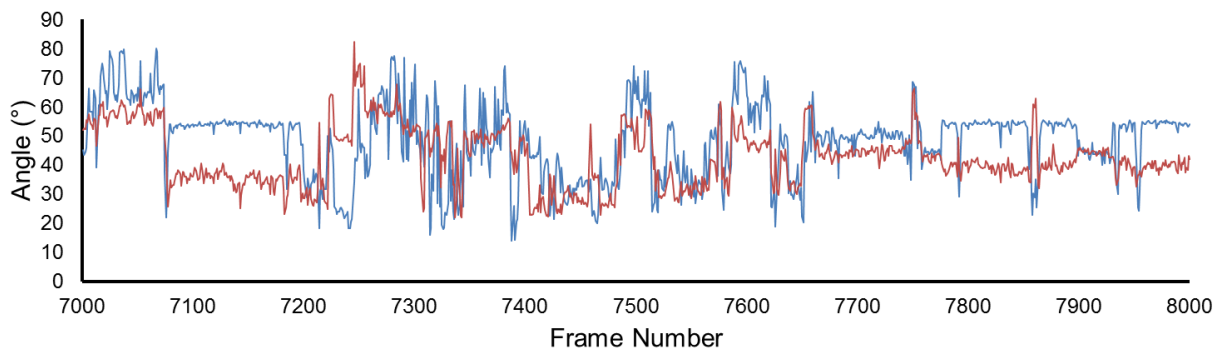
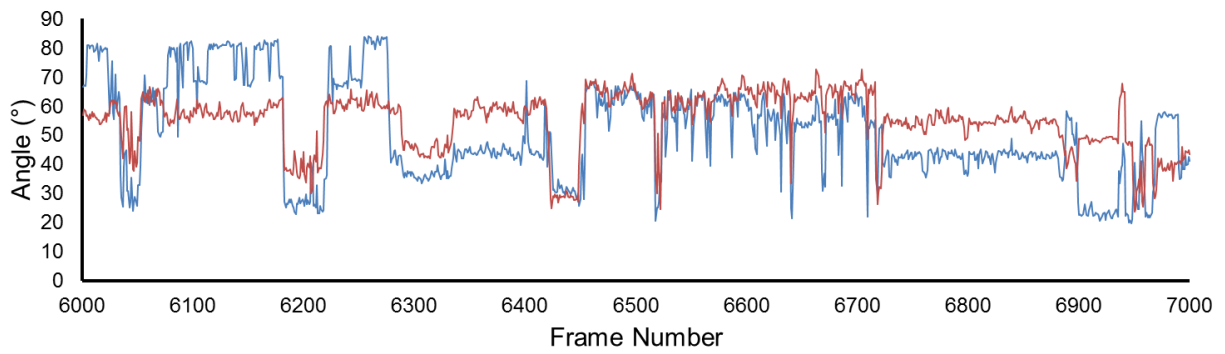
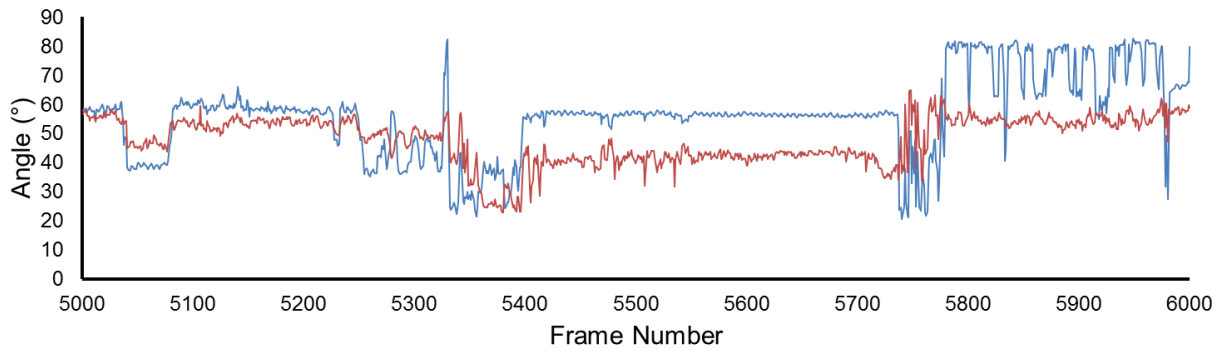
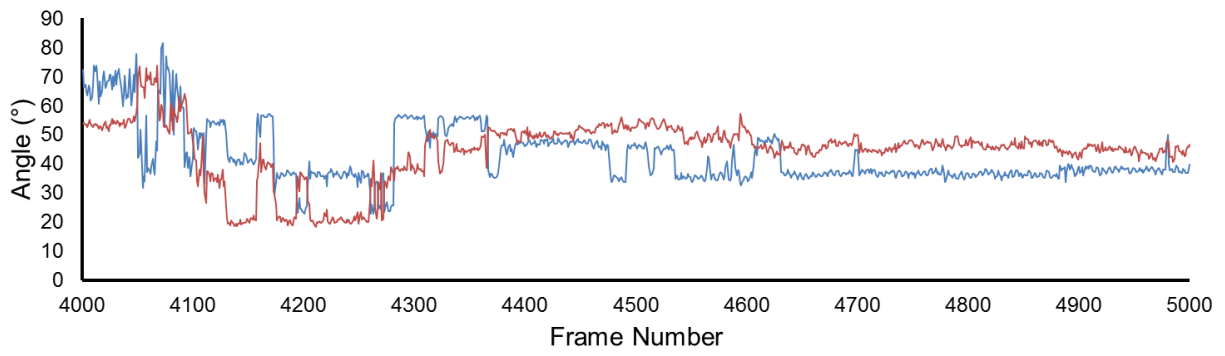


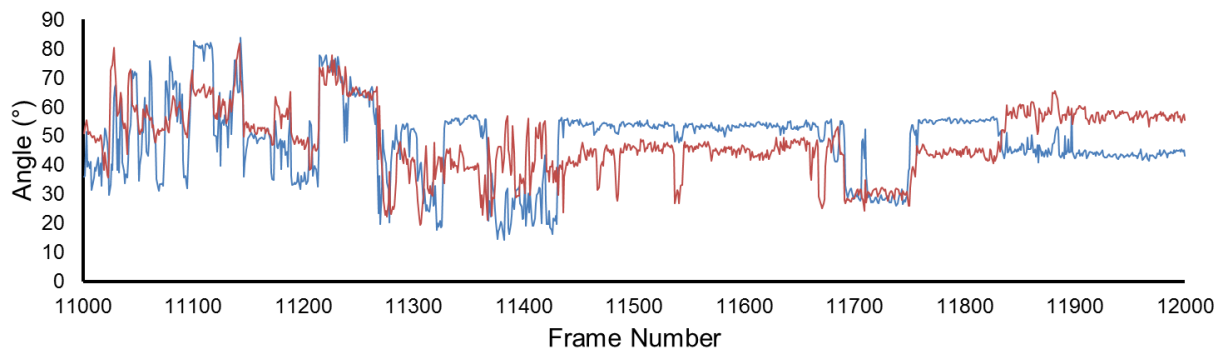
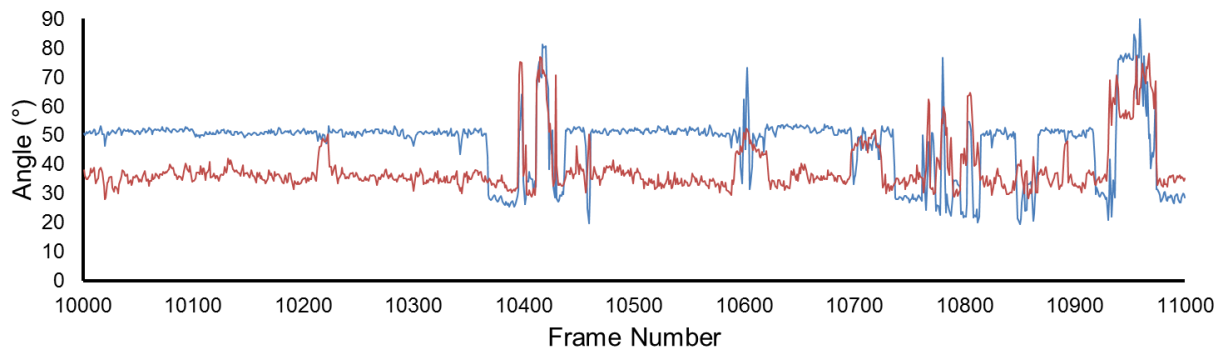
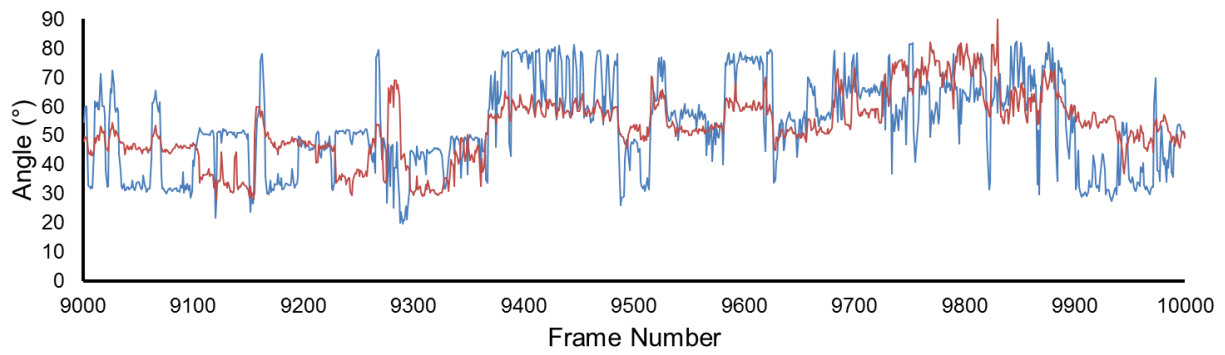
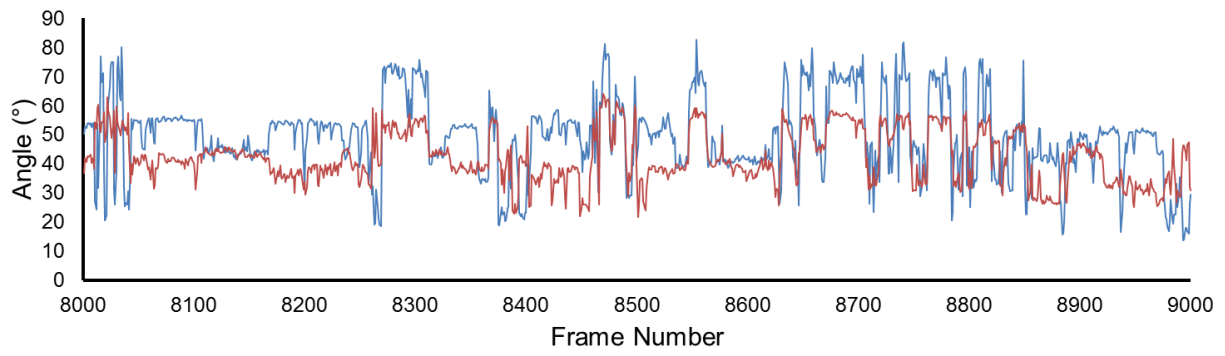


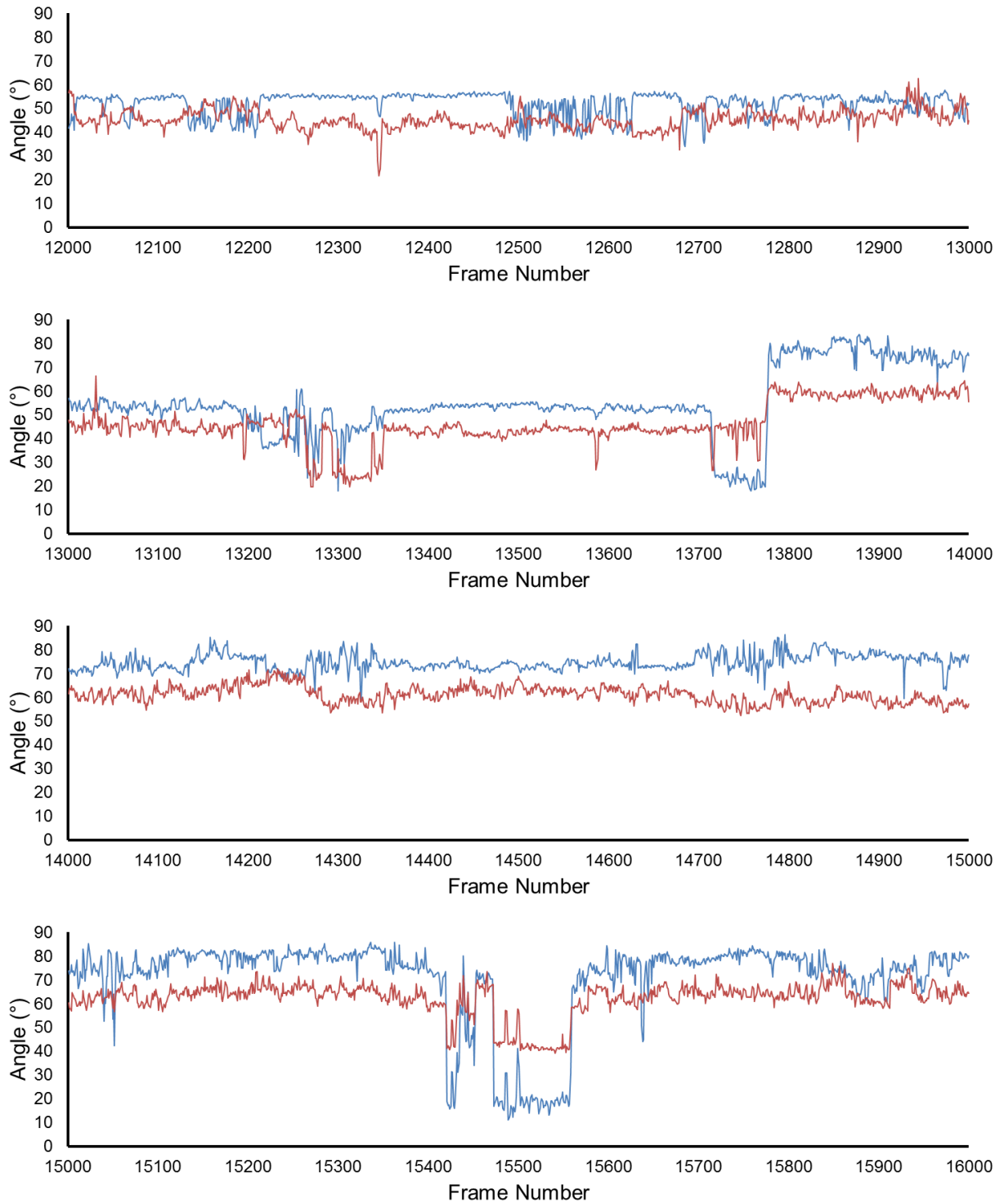
**Figure 6.** Full 1000 frame comparison between LSPR and SSPR s-polarization and LSPR p-polarization SSPR s-polarization. The top two graphs are the normalized intensity traces, while

the bottom two graphs are the calculated angles. Correlation coefficients in main text were calculated from these full 1000 frames.

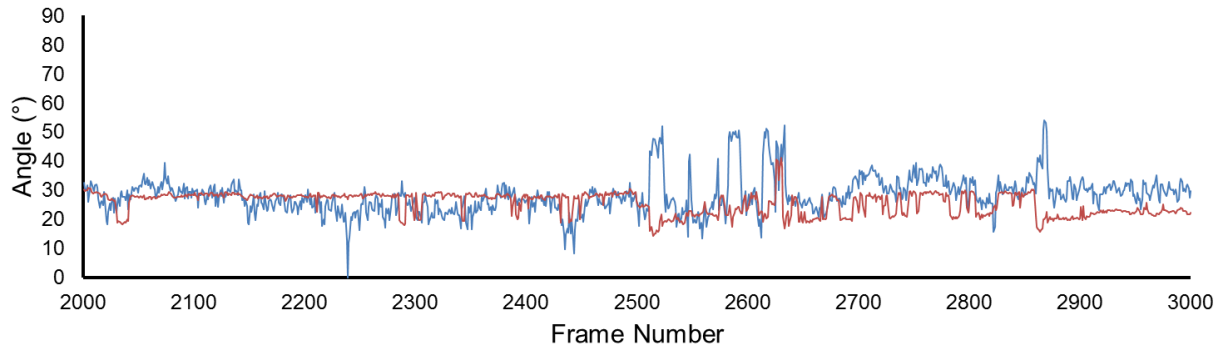
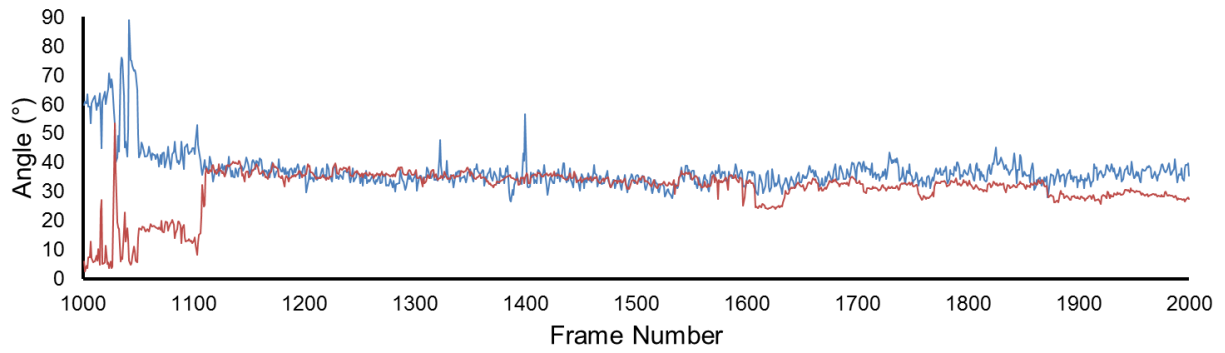
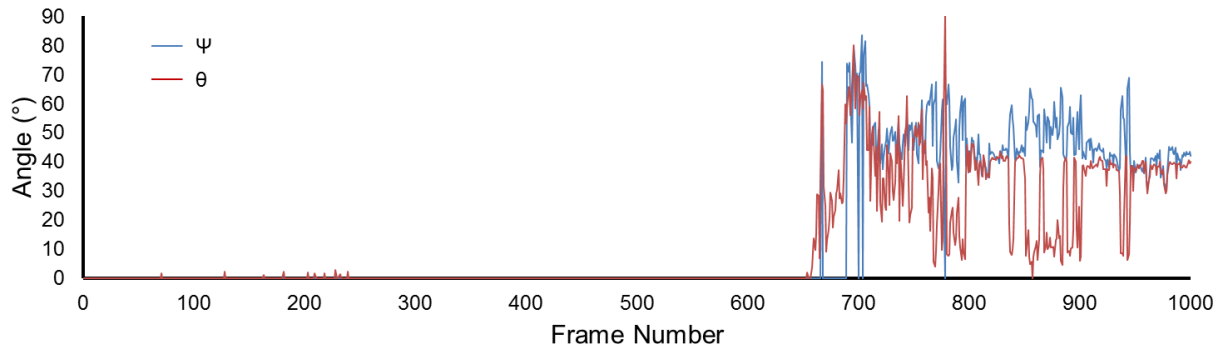








**Figure 10.** Complete trace of Figure 3 in main text. Many segments of high and low rotational activity can be seen.



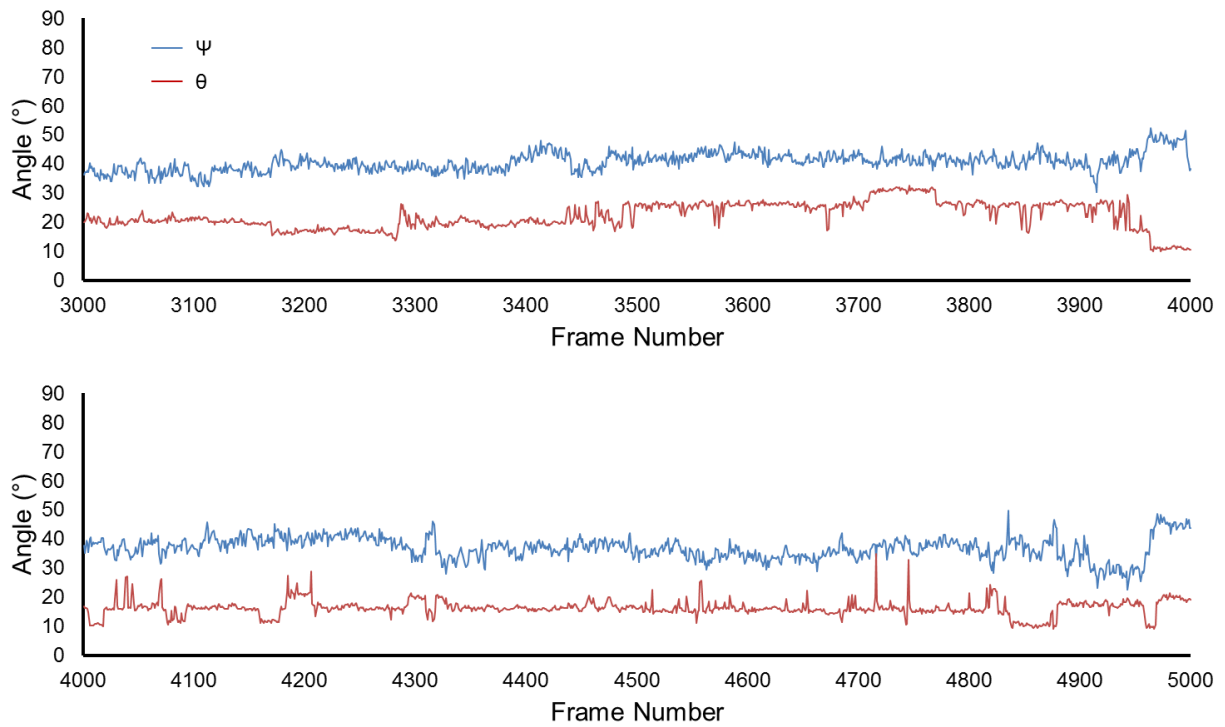


**Figure 11.** Complete trace referred to in Figure 4a of the main text. Angular calculations were based on intensity after frame 711 while position measurements were determined after frame 791 when the AuNR found its final position.



## CHAPTER 4: THREE-DIMENSIONAL ORIENTATION DETERMINATION OF STATIONARY ANISOTROPIC NANOPARTICLES WITH SUB-DEGREE UNCERTAINTY UNDER TOTAL INTERNAL REFLECTION SCATTERING MICROSCOPY

### Abstract

Single-particle and single-molecule orientation determination plays a vital role in deciphering molecular motion in complex environments. Previous attempts to determine the absolute three-dimensional orientation of static anisotropic particles rely on subjective pattern matching and are inherently plagued by high degrees of uncertainty. Herein, we describe a method utilizing total internal reflection scattering microscopy to determine the 3D orientation of gold nanorods with sub-degree uncertainty.

### Introduction

Single particle orientation and rotational tracking (SPORT) techniques have made a large impact in studying molecular motions.<sup>1</sup> This is due partially to the rise in use of plasmon resonant nanoparticles as imaging probes compared to organic fluorescent dyes or semiconductor quantum dots. The advantages of these nanoparticles include large absorption and scattering cross sections,<sup>2</sup> high-photostability,<sup>2,3</sup> biocompatibility,<sup>4</sup> and shape-induced anisotropic optical properties.<sup>5</sup> While the other traits are crucial to their application, it is the anisotropic optical properties that allows for the determination of particle orientation and thus the elucidation of molecular motions.

Particle orientation determination for gold nanorods (AuNRs) in the plane of the sample substrate has been demonstrated by a few optical techniques including dark-field (DF) polarization microscopy,<sup>5-7</sup> photothermal heterodyne imaging,<sup>8</sup> and differential interference contrast (DIC) microscopy.<sup>9-13</sup> Light scattered from AuNRs has been shown to be strongly polarized along the long axis,<sup>14</sup> and the aforementioned techniques take advantage of this scattering trait by monitoring the intensity of orthogonally polarized light to determine the in-plane orientation of the nanoparticles. While these techniques are simple to implement, they lack the ability to determine the out-of-plane (tilt) orientation of the AuNRs.

Image recognition has been implemented with DIC microscopy,<sup>15</sup> defocused microscopy,<sup>16-18</sup> and total internal reflection scattering (TIRS) microscopy<sup>19</sup> to determine the three-dimensional (3D) particle orientation without degeneracy. Unfortunately, these techniques are accompanied by a large degree of error ( $>10^\circ$ ) in determining out-of-plane orientation that is associated with orientation dependent signal or the necessity to match defocused image patterns.

Defocused imaging techniques such as those used with dark-field microscopy use pattern matching of simulated images to determine the 3D orientation of anisotropic metallic nanoparticles. The resolution of which is dependent on the ability of a researcher to determine whether or not a particular pattern matches. This requires the correct simulation input of the defocus depth that may not be accurately estimated if particles are in different sample planes. Figure 1 shows examples of how a defocus change of even a few hundred nanometers can affect pattern matching, while Figure 2 demonstrates how difficult it can be to match even correctly simulated defocused images. A more recent technique called focused orientation and position imaging (FOPI) induces an image charge-coupled effect with the substrate to determine 3D orientation information but also suffers from image correlation and has the added necessity of needing a particular substrate-particle interaction.<sup>19</sup>

Previously, we have demonstrated the ability to use both short- and long-axis surface plasmon resonance (SPR) enhancement to simultaneously probe the in-plane and out-of-plane (tilt) motion of dynamic surface-bound AuNRs using TIRS microscopy.<sup>20</sup> By illuminating the sample with two wavelengths of the light that are orthogonally polarized, the particle intensity fluctuates correspondingly to the 3D orientation of rotating particles. While the previous technique is limited to the study of dynamic nanorods, herein, we expand the study to stationary probes. Using a combination of defocused imaging and the rotation of linearly polarized light incident upon the sample, we resolve the 3D orientation of AuNRs with unprecedented precision under TIRS microscopy.

## Results and Discussion

AuNRs with an aspect ratio of 2.4 (25 nm  $\times$  60 nm) and a long axis SPR absorption peak centered at 628 nm were used. The instrument is a TIRS microscope modified from its previous description.<sup>19, 20</sup> Briefly, our prism-based TIRS microscope consists of a 660 nm continuous wave (CW) linearly polarized laser directed through periscope optics and focused under the

objective. Placed after the periscope, a double Fresnel rhomb acting as a  $\lambda/2$  wave plate (HWP) was inserted into the light path of the 660 nm laser. This HWP was attached to a computer-controlled rotating stage that can allow light to pass down its center. We used this stage/HWP combination to accurately control the polarization direction under TIR. It should be noted that a double Fresnel rhomb is not considered a polarization rotator like that of a half-wave plate made from birefringent material. The double Fresnel rhomb HWP actually produces elliptically or circularly polarized light depending on its orientation, but since we are using a TIR method, the effect at the sample is identical. A more detailed explanation can be found in Methods.

To create a stationary environment with randomly oriented particles, AuNRs were diluted in a 0.5% (w/v) solution of agarose gel before being deposited on a quartz slide where it cooled for 30 minutes. The slide was then placed on the prism, focused under the microscope, and allowed to settle for 30 minutes to reduce sample drift. Using the HWP the polarization of the incoming laser was carefully aligned to produce s-pol light (light with the electric field parallel to the substrate surface). Light that has the electric field aligned perpendicular to the substrate surface is considered p-polarized (p-pol). EMCCD exposure time was 30 ms in frame transfer mode while the stage rotated the HWP at  $15^\circ/\text{s}$ . The polarization direction rotates at double the speed of the HWP producing a speed of  $30^\circ/\text{s}$  and  $0.9^\circ$  of polarization rotation per frame. The sample was then defocused by  $\sim 1.0 \mu\text{m}$ , and the procedure was repeated producing two data sets for each area of interest. The  $\sim 1.0 \mu\text{m}$  defocus depth was chosen to produce defocused images dissimilar to images that would be produced at nearby focal depths (Figure 1) and maximize the effect the polar angle has on the image pattern.

The coordinate system for the electric field, particle orientation, and polarization direction is similar to that used by Beausang *et al.* and has been defined in Figure 3.<sup>21</sup> In the microscope coordinate system,  $x$  and  $y$  comprise the sample plane and  $x$  is the direction of illumination propagation. The optical axis is  $z$ . The AuNR orientation is defined by the polar angle ( $0^\circ \leq \theta \leq 90^\circ$ ) and the azimuthal angle ( $0^\circ \leq \phi \leq 180^\circ$ ), which originates on the  $x$  axis. The angle of the polarization rotation ( $\zeta$ ) is  $0^\circ$  when the polarization is horizontal and therefore producing s-pol illumination.

Rotating the polarization direction affects the electric field polarization ( $\hat{\epsilon}$ ) produced by changing the ratio of s-pol and p-pol light at the surface of total internal reflection (TIR) (see Methods for details). Since the particles are treated as an anisotropic dipole, the scattering

intensity from the AuNR is dependent on both the 3D particle orientation and  $\hat{\epsilon}$ . Rotation of the HWP produces a periodic intensity fluctuation as displayed for an example particle (P1) in Figure 4A. Knowing the azimuthal angle, the intensity versus  $\zeta$  can be fit to simulations to determine the polar angle. To aid in the fitting of the polar angle, the intensity curves were first fit to a higher-order polynomial.

Though we previously mentioned that defocused imaging techniques are difficult to interpret for polar angle determination, high azimuthal angle accuracy can be achieved under the proper conditions. The defocusing of a AuNR produces an image pattern with an axis of symmetry corresponding to the long axis of the particle (Figure 4E). The simplest method of determining symmetry involves slicing the particle image into two halves through the center point and comparing the integrated intensity. A MATLAB code was written that rotates the axis in which the image is sliced and calculates the differences in integrated intensities (see Methods for details). By rotating the incoming polarization while the image is defocused, the highest contrast image can be used in determining image symmetry resulting in a reduction of the azimuthal angle uncertainty. For P1 the angle that produces the smallest difference is  $44.1^\circ \pm 0.9^\circ$  and thus the angle of the AuNR. The uncertainty of the azimuthal angle is determined by multiplying the noise by the total image area and adding it to the integrated intensity difference at the angle of symmetry. The precision can be increased by collecting more signal until, ultimately, it is limited by the amount of photons the camera can collect. While stacking images is a common method to increase the signal-to-noise ratio, it would necessitate the starting and stopping of the rotational stage inducing error in polarization position.

Figure 5 makes obvious the advantage of using a high-contrast image to reduce the uncertainty in calculating the azimuthal angles of particles. Similar to other single-molecule or single-particle experiments, the stronger the signal the less the angle determination is affected by noise. Figure 5A displays the plots of the same particle at different angles  $\zeta$  and therefore different intensities. The grey line represents the uncertainty caused by noise within the signal collection.

By knowing both the intensity profile produced by changing  $\zeta$  and  $\varphi$  from the defocused images, we can calculate the angle  $\theta$  for the AuNR. Considering each particle to be an anisotropic electromagnetic dipole that scatters preferentially down its dipole axis, the intensity curves for 3D particle orientations were simulated revealing that the intensity at  $\zeta$  is dependent

upon both  $\theta$  and  $\varphi$  (see Methods for simulation details). Figure 6 reveals the relationship to  $\varphi$  and how closely the maximum intensity at angle  $\zeta$  relates to the simulated angle  $\theta$ . By fitting the simulated curve to the data using non-linear least squared fitting, the polar angle for P1 was calculated to be  $23.4^\circ \pm 0.8^\circ$  at the 68% confidence interval using  $\chi^2$  fitting. These angles match well with the simulated defocused image (Figure 4F).

It is important to note how the simulated curves relate to both  $\theta$  and  $\varphi$  (Figure 6). When the azimuthal angle is at  $90^\circ$  it means the longitudinal axis is aligned for maximum scattering with the incoming laser. Under this condition, the peak maximums are closely related to the polar angle. This relates to low uncertainty when fitting the data. When the azimuthal angle is  $0^\circ$ , the peak positions are at  $90^\circ$  no matter the polar angle, resulting in a higher uncertainty of the polar angle when the particle is aligned with the x-axis. The high degree of precision in determining the azimuthal angle from the defocused images is therefore paramount to the determination of the polar angle. It also becomes obvious that in the few cases where the long axis of the AuNR is exactly aligned with the x-axis of the system, the technique cannot extrapolate the polar angle. This can be overcome by changing the orientation of the sample by some known amount before again rotating the polarizing direction.

To demonstrate these influencing factors in the uncertainty, more particles were analyzed to compare the precision of the 3D orientation to a particle (P2) that had a less obvious axis of symmetry (Figure 7) and a particle (P3) that has an azimuthal angle closer to  $0^\circ$  and thus more uncertainty in fitting (Figure 8). P2 ( $\varphi = 74.8^\circ \pm 2.7^\circ$ ,  $\theta = 81.5^\circ \pm 0.3^\circ$ ) has an azimuthal angle uncertainty larger than P1, but due to the near  $90^\circ$  in-plane orientation, the fit generates a small uncertainty in the polar angle. Just the opposite is true in P3 ( $\varphi = 8.6^\circ \pm 0.4^\circ$ ,  $\theta = 48.3^\circ \pm 2.4^\circ$ ) in which the azimuthal has a small uncertainty but due to the in-plane orientation being near  $0^\circ$ , the resulting polar angle has a larger uncertainty than P1. Through these examples, it is apparent that the uncertainty in the polar angle determination arises from a combination of the intensity and the orientation of the particle.

An additional advantage of this technique is its ability to distinguish single particles from aggregates (multiple particles within the diffraction limited spot). The distinction can be made using either the defocused (Figure 9) or focused (Figure 10) polarization rotation data set. In Figure 9 comparisons are made between two single particles with either a large or small polar angles and an aggregate (multi-mer). The comparisons are made at the polarization orientation of

$0^\circ$  and  $90^\circ$  producing predominantly s-pol and p-pol light at the surface of TIR respectively. As can be seen, the single particles produce a high contrast image in under one polarization and nearly no image in the opposing polarization. On the other hand, the aggregate produces a well-defined defocused image at both polarizations suggesting at least two particles are within the diffraction limited spot size.

The focused polarization rotation data can also be applied in separating single particles from aggregates. Figure 10 displays the images of two areas as the polarization direction is rotated  $180^\circ$ . The spot in the left column displays the typical periodic bright to dark intensity response, while the spot in the right column seems to transform from a Gaussian shaped intensity profile to a donut shape. Interpretation of the donut shape indicates a AuNR with a small polar angle is near a AuNR with a large polar angle. The ability of the polarization direction rotation to isolate particles that are within diffraction limits areas opens up an exciting opportunity in single particle orientation determination and tracking.

## Conclusion

A method for determining the 3D orientation of stationary metallic anisotropic nanoparticles with sub-degree uncertainty has been demonstrated under TIRS microscopy. Rotating the incoming polarization direction produces intensity curves that are unique to the 3D orientation of the particle. Determining the azimuthal angle by precisely calculating the symmetry axis of a defocused image allows for the fitting of the polarization rotation data to simulations to determine the polar angle. The technique is also useful for identifying single particles versus aggregates within the diffraction limited area. We foresee this technique being applied to various studies such as nanoparticle loading before cargo transport in engineered environments, surface mapping, and other applications involving particle interaction.

## Acknowledgements

The author of this chapter would like to thank Keith Fritzsche from Iowa State University for his help regarding the home written MATLAB codes. Keith provided valuable discussions with regards to the design of the programs along with help in the coding itself. This work was supported by the U.S. Department of Energy, Office of Basic Energy Sciences, Division of Chemical Sciences, Geosciences, and Biosciences through the Ames Laboratory. The

Ames Laboratory is operated for the U.S. Department of Energy by Iowa State University under contract no. DE-AC02-07CH11358.

## Methods

***TIRS/TIRF Microscope.*** The instrument is a home built variable-angle total internal reflection scattering microscope that was slightly modified from previous TIRS and TIRF microscopy applications.<sup>19, 20, 22, 23</sup>

The prism-based TIRS instrument was built around a Nikon Optihot-2 microscope, of which the original state was removed and replaced with a Sutter MP-285 motorized 3D translational stage (Novato, CA). The Sutter stage supported a homemade prism holder that held an equilateral Bk7 prism (Melles Griot, Albuquerque, NM). A 660-nm continuous wave (CW) laser (Ignis, LaserQuantum, San Jose, CA) with an adjustable power output (max 200 mW) was used as the excitation source. The beam was directed through a periscope set of optics, a Uniblitz mechanical shutter (model LS2Z2, Vincent Associates, Rochester, NY), and a focusing lens (15-cm focal length) before being directed to the mirror on a galvanometer optical scanner (model 6220H, Cambridge Technology, Cambridge, MA). The focusing lens was used to control the laser illumination size under the objective, while the mirror galvanometer was used in conjunction with a motorized linear stage (model MAA-PP, Newport, Irvine, CA) to direct the laser beam through the equilateral prism to the solid-liquid interface. The scattered light was collected by an objective (Plan Fluor, 100x, NA 1.3, oil immersion) before being recorded by our Andor iXon<sup>EM</sup> + 897 EMCCD (Belfast, Northern Ireland; 512x512 imaging array, 16  $\mu\text{m}$  x 16  $\mu\text{m}$  pixel size). To control the incoming laser polarization a half-wave Fresnel rhomb (FR600HM, Thorlabs, Newton, NJ) was placed into the laser path after the shutter. The Fresnel rhomb was connected to a computer-controlled rotating stage (8MRU-1, Altos Photonics, Bozeman, MT).

***The Use of a Double Fresnel Rhomb for Polarization Control.*** A double Fresnel rhomb rotates the polarization direction by 90° through the use of multiple total internal reflections. Unlike a HWP that uses birefringence to control polarization direction, a double Fresnel rhomb will produce elliptically polarized light when it is rotated to angles between 0° and 45° (for each degree rotated the polarization direction rotates 2 $\zeta$ ).



Since the light undergoes TIR at the sample, regardless of the polarization circularity, the polarization is broken into s-pol and p-pol components. When the double Fresnel rhomb is rotated  $22.5^\circ$ , it is producing circularly polarized light, which is translated into half s-pol and half p-pol components at the surface of TIR. The same would be true of the incoming illumination was polarized linearly at  $\zeta=45^\circ$ . Therefore, while a double Fresnel rhomb cannot be used in many other microscopy techniques to control polarization direction, a TIR illumination scheme is compatible with either a birefringent HWP or a double Fresnel rhomb.

***AuNR Orientation Determination. Polarization Rotation.*** AuNRs (25 nm x 60 nm, aspect ratio 2.4) were purchased from Nanopartz (Salt Lake City, UT). The particles were diluted in a solution of 0.5 (w/v) agarose (Promega, Madison, WI) solution to an appropriate concentration. Hot solution was placed on a 2" x 1" quartz microscope slide (SPI Supplies, West Chester, PA) and quickly covered by a 18 mm<sup>2</sup> Corning coverslip. The sample was sealed with enamel and allowed to gel for 30 min at room temperature.

The slide was then placed on the prism and focused under TIRS before being allowed to settle for an additional 30 minutes to reduce sample drift. The double Fresnel rhomb (Thorlabs) HWP was installed onto the rotation stage by the threaded mount taking care to center the laser beam through the HWP. The orientation of the HWP was carefully determined by first placing a polarizer perpendicular to the beam path. The HWP was rotated until maximum extinction occurred determining the horizontal polarization (s-pol).

Data was collected while rotating the polarization at  $30^\circ/\text{s}$  with a 30 ms camera exposure in frame transfer mode leading to a polarization rotation of  $0.9^\circ/\text{frame}$ . Since the control of the rotating stage and our EMCCD is done with separate software, there is a lag of  $\sim 30$  frames before the rotation was started. To determine the frame in which the rotation starts a single particle can be used. A AuNR with an approximate polar angle of  $45^\circ$  was chosen and MATLAB was used to plot the sum of the 10 brightest pixels in a user defined region of interest (ROI) against frame number. The average and standard deviation ( $\sigma$ ) was calculated from the first 20 points. When the signal intensity exceeded the average  $\pm 3\sigma$ , the point was determined to correspond to the angle  $\zeta = 0.9^\circ$  and the previous point to  $\zeta = 0.0^\circ$ .



The first 180° of the polarization rotation is then plot in MATLAB and fit with a multi-order polynomial. The polynomial curve is then used in the fitting with simulations to produce the polar angle of the particle.

**Azimuthal Angle Determination.** To correctly determine the polar angle, the azimuthal angle ( $\varphi$ ) must first be determined. While we mentioned that defocused imaging is unreliable for polar angle determination, optimized properly, an accurate azimuthal angle can be obtained from the image. The in-plane angle of the AuNR can be determined from a defocused image by determining the symmetry of the image. The resulting plane of symmetry is then used as the direction of the long-axis of the particle. The simplest way of determining symmetry is to cut the image into two equal area regions around the central point of the image at a variety of angles and determine the intensity in each region. When the intensity difference between the two regions is minimal, the angle will correspond to the angle of symmetry.

As mentioned in the main text, after rotation data are collected for the in-focus AuNR, the procedure is repeated with the sample plane defocused by  $\sim 1 \mu\text{m}$ . The frame in which the intensity for the AuNR is at its maximum is then selected from the stack. A region of interest 27 pixels by 27 pixels is drawn around the AuNR and cropped. This image is then loaded into a home written MATLAB code which calculates the symmetry. It should be noted that the line used to cut the image in half is considered infinitely thin and program will actually cut pixels and assign the appropriate count of intensity to the fractions of the original pixel. Using this technique, no error is generated in integrating the intensity from program.

For each AuNR, the image is first divided down the  $x$  axis through the image center creating two regions (top and bottom), the total intensity of the regions is then summed and the difference is taken. The image is rotated by increments of  $0.1^\circ$  and the process is repeated. The angle that produces the smallest difference between the two regions has the most symmetry and corresponds to the azimuthal angle.

The accuracy of the azimuthal angle determination ultimately depends on the signal of the AuNR and the noise of the image. When the overall signal of the particle is low such as when the AuNR is at the outer edge of the evanescent field or the incoming polarization is not optimized, the background noise will make up a larger fraction of the symmetry regions leading to false orientation assignments. Other false assignments may occur when a AuNR is approaches a near  $0^\circ$  or near  $90^\circ$  polar angle. If the noise component is greater than the subtle differences

associated with the particle tilt, actual symmetry may not be determined. Thus, azimuthal angle uncertainty increases the farther the particle is from the surface of TIR, and when the particle reaches nears either extreme in polar angle.

The uncertainty of the angle determination is made by first finding the standard deviation of the background. This is considered the noise of the system. The noise is then multiplied by the area of the image and added to the integrated intensity difference produced at the angle of symmetry. The angles that produce intensity difference less than this intensity value are within the range of uncertainty. A representation of the uncertainty as dependent on total image intensity can be found in Figure 5.

**Simulating Intensity Profiles with Respect to  $\zeta$ .** In order to determine the polar angle of the AuNR, measured scattering intensities have to be compared to calculated data from a theoretical model of the AuNR. Within this model we approximate the particle as an anisotropic electromagnetic dipole  $\hat{\mu}$  that scatters photons polarized preferentially along its dipole axis. The scattering intensity,  $I_s$ , is related to the dipole vector and the electric field polarization ( $\hat{\varepsilon}$ ):

$$I_s(\hat{\mu}_s, \hat{\varepsilon}) \equiv |\hat{\mu}_s \cdot \hat{\varepsilon}|^2 \quad (1)$$

$$\begin{aligned} \propto & \left( \varepsilon_x^2 \mu_x^2 + \varepsilon_y^2 \mu_y^2 + \varepsilon_z^2 \mu_z^2 + 2\varepsilon_x \varepsilon_y \mu_x \mu_y \sin(\delta_s - \delta_p) \right. \\ & \left. + 2\varepsilon_y \varepsilon_z \mu_y \mu_z \sin(\delta_s - \delta_p) \right) \quad (2) \end{aligned}$$

These calculations assume the coordinate system described in the main text where  $x$  and  $y$  are the image plane and  $x$  is the propagation direction of the incident light. The  $z$  direction is into the microscope objective. The orientation of the AuNR is again described through the polar and azimuthal angle  $(\theta, \varphi)$ , hence the dipole orientation can be described:

$$\hat{\mu} = (\sin \theta \cos \varphi, \sin \theta \sin \varphi, \cos \theta) \quad (3)$$

The Cartesian coordinates are thus determined by the magnitude of the  $s$  and  $p$  polarization components of the evanescent field. Within our system the  $s$  component of the

overall  $\varepsilon$  is constrained to the  $y$  direction. The  $p$  component of  $\varepsilon$  is predominantly in the  $z$  direction, though there is also a component that propagates in the  $x$  direction. The composition of the evanescent field is described in the following equations:

$$\varepsilon_{p,t} = -2 \cos(\zeta) \cos(\theta_i) \sin(\delta_p) \quad 4)$$

$$\varepsilon_{p,n} = 2 \cos(\zeta) \sin(\theta_i) \cos(\delta_p) / \xi^2 \quad 5)$$

$$\varepsilon_s = 2 \sin(\zeta) \cos(\delta_s) \quad 6)$$

where  $\theta_i$  is the incident angle of the illuminating laser light,  $\zeta$  is the ratio of the indices of refraction of the AuNRs surrounding to the slide material, and  $\delta_s$  and  $\delta_p$  are the phase lags for  $s$  and  $p$  polarized light, respectively.

$$\delta_p = \tan^{-1} \left[ \frac{(\sin^2 \theta - \sin^2 \theta_c)^{\frac{1}{2}}}{\sin^2 \theta_c \cos \theta} \right] \quad 7)$$

$$\delta_s = \tan^{-1} \left[ \frac{(\sin^2 \theta - \sin^2 \theta_c)^{\frac{1}{2}}}{\cos \theta} \right] \quad 8)$$

Where  $\theta_c$  is the critical angle determined by the indices of refraction of the substrate and sample medium.

## References

1. Stender, A. S.; Marchuk, K.; Liu, C.; Sander, S.; Meyer, M. W.; Smith, E. A.; Neupane, B.; Wang, G.; Li, J.; Cheng, J.-X.; Huang, B.; Fang, N. *Chemical Reviews* **2013**.
2. Sperling, R. A.; Rivera gil, P.; Zhang, F.; Zanella, M.; Parak, W. J. *Chemical Society Reviews* **2008**, 37, (9), 1896-1908.
3. Wu, X. Y.; Yeow, E. K. L. *Nanotechnology* **2008**, 19, (3).

4. Murphy, C. J.; Gole, A. M.; Stone, J. W.; Sisco, P. N.; Alkilany, A. M.; Goldsmith, E. C.; Baxter, S. C. *Accounts of Chemical Research* **2008**, 41, (12), 1721-1730.
5. Sonnichsen, C.; Alivisatos, A. P. *Nano Letters* **2005**, 5, (2), 301-304.
6. Xiao, L. H.; Qiao, Y. X.; He, Y.; Yeung, E. S. *Journal of the American Chemical Society* **2011**, 133, (27), 10638-10645.
7. Pierrat, S.; Hartinger, E.; Faiss, S.; Janshoff, A.; Soennichsen, C. *Journal of Physical Chemistry C* **2009**, 113, (26), 11179-11183.
8. Chang, W. S.; Ha, J. W.; Slaughter, L. S.; Link, S. *Proceedings of the National Academy of Sciences of the United States of America* **2010**, 107, (7), 2781-2786.
9. Ha, J. W.; Sun, W.; Wang, G. F.; Fang, N. *Chemical Communications* **2011**, 47, (27), 7743-7745.
10. Ha, J. W.; Sun, W.; Stender, A. S.; Fang, N. *Journal of Physical Chemistry C* **2012**, 116, (4), 2766-2771.
11. Wang, G. F.; Sun, W.; Luo, Y.; Fang, N. *Journal of the American Chemical Society* **2010**, 132, (46), 16417-16422.
12. Gu, Y.; Sun, W.; Wang, G. F.; Fang, N. *Journal of the American Chemical Society* **2011**, 133, (15), 5720-5723.
13. Gu, Y.; Sun, W.; Wang, G.; Jeftinija, K.; Jeftinija, S.; Fang, N. *Nature Communications* **2012**, 3.
14. Sonnichsen, C.; Franzl, T.; Wilk, T.; von Plessen, G.; Feldmann, J.; Wilson, O.; Mulvaney, P. *Physical Review Letters* **2002**, 88, (7).
15. Xiao, L.; Ha, J. W.; Wei, L.; Wang, G.; Fang, N. *Angewandte Chemie-International Edition* **2012**, 51, (31), 7734-7738.
16. Toprak, E.; Enderlein, J.; Syed, S.; McKinney, S. A.; Petschek, R. G.; Ha, T.; Goldman, Y. E.; Selvin, P. R. *Proceedings of the National Academy of Sciences of the United States of America* **2006**, 103, (17), 6495-6499.
17. Li, T.; Li, Q.; Xu, Y.; Chen, X.-J.; Dai, Q.-F.; Liu, H.; Lan, S.; Tie, S.; Wu, L.-J. *Acs Nano* **2012**, 6, (2), 1268-1277.
18. Xiao, L. H.; Qiao, Y. X.; He, Y.; Yeung, E. S. *Analytical Chemistry* **2010**, 82, (12), 5268-5274.
19. Ha, J. W.; Marchuk, K.; Fang, N. *Nano Letters* **2012**, 12, (8), 4282-4288.

20. Marchuk, K.; Ha, J. W.; Fang, N. *Nano Letters* **2013**, 13, (3), 1245-1250.
21. Beausang, J. F.; Schroeder, H. W., III; Nelson, P. C.; Goldman, Y. E. *Biophysical Journal* **2008**, 95, (12), 5820-5831.
22. Marchuk, K.; Guo, Y. J.; Sun, W.; Vela, J.; Fang, N. *Journal of the American Chemical Society* **2012**, 134, (14), 6108-6111.
23. Sun, W.; Marchuk, K.; Wang, G. F.; Fang, N. *Analytical Chemistry* **2010**, 82, (6), 2441-2447.

## Figures

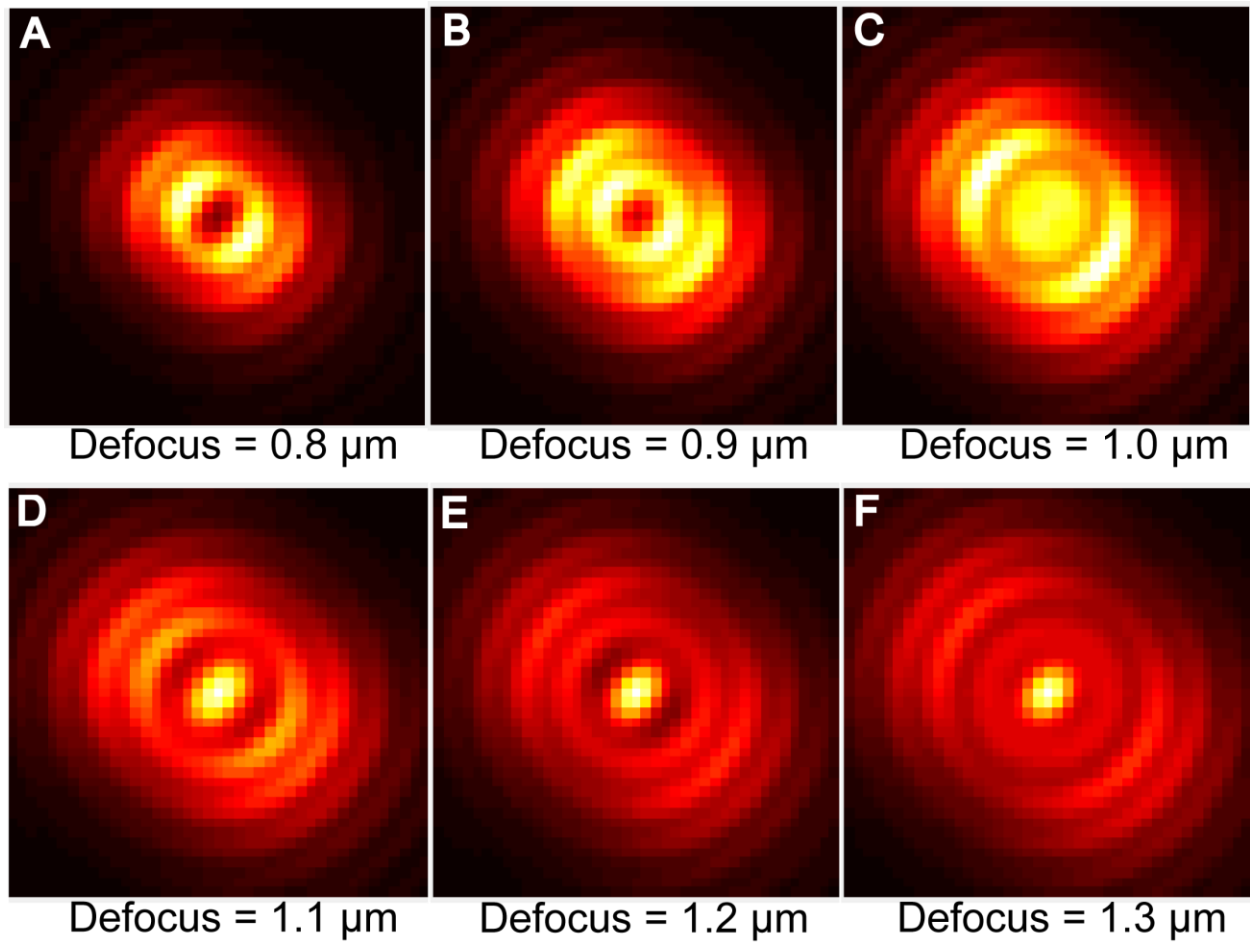


**Figure 1.** Simulated defocused patterns of gold nanorods at  $\theta = 0^\circ$ . Patterns (A-F) are varied in their defocus depth by 100 nm to illustrate the effect of different defocus depths has on the recorded image.

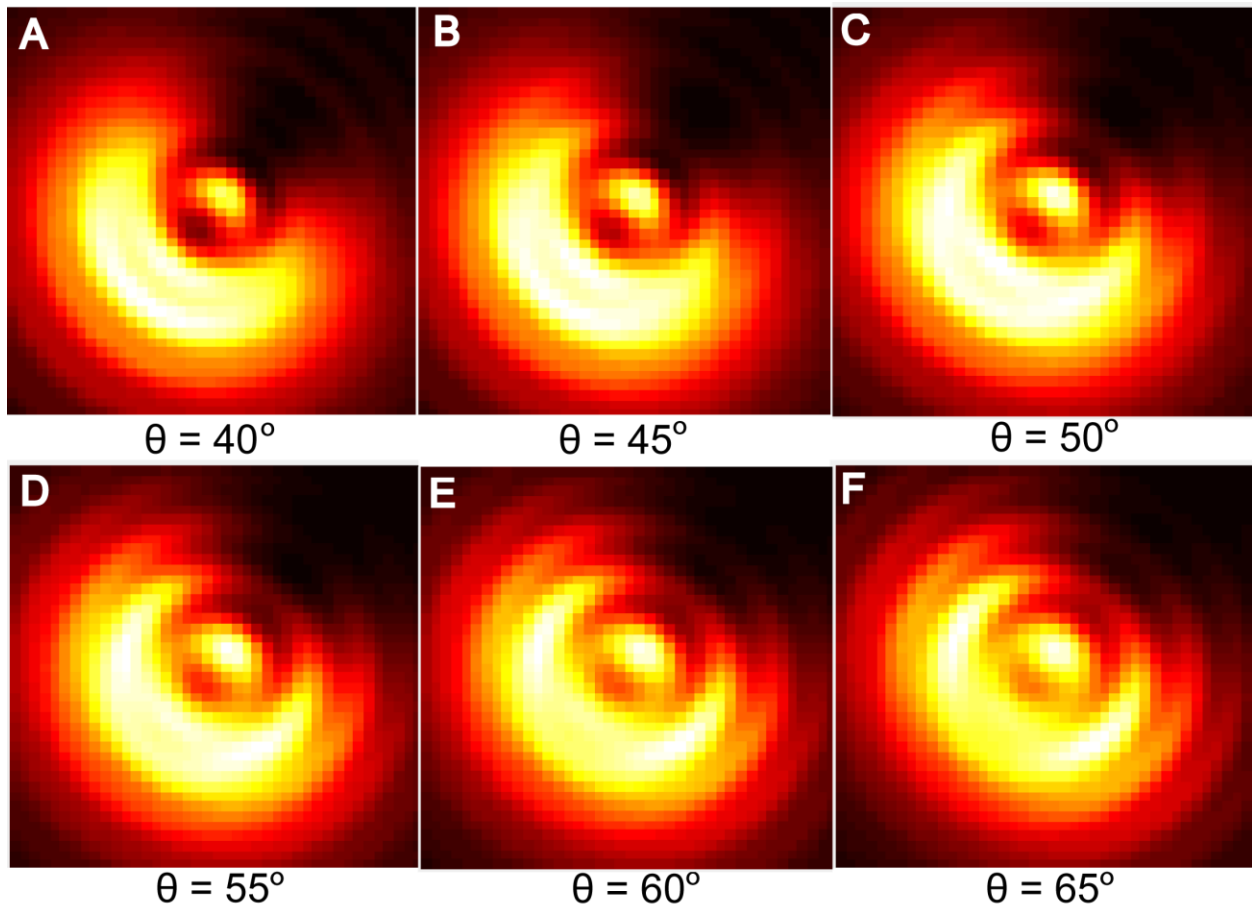


**Figure 2.** Simulated defocused patterns of gold nanorods at polar angles varying from  $40^\circ$ - $65^\circ$ . All images were simulated with the same defocus depth of  $1.0 \mu\text{m}$ . Presented to illustrate the difficulty in reliably assigning polar angles of tilted particles.

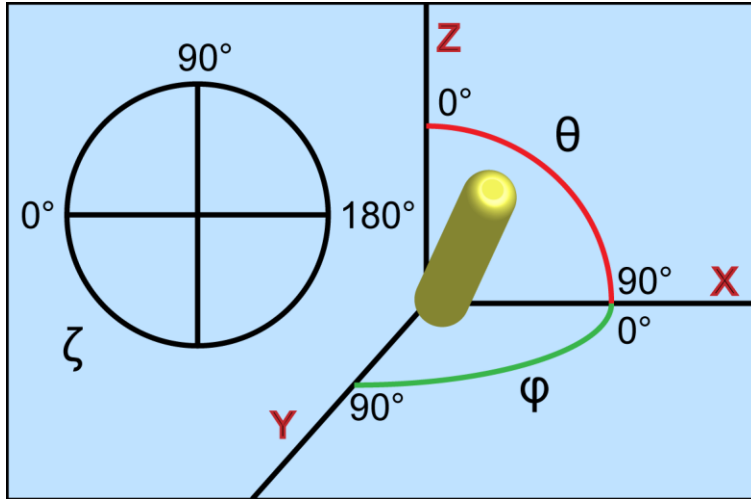


**Figure 3.** The coordinate system for both the polarization direction (left) and the 3D orientation of the AuNR. X and Y is the sample plane with X being the direction of the incoming laser. Z is the axial direction.  $\psi$ : azimuth angle,  $\theta$ : polar angle.



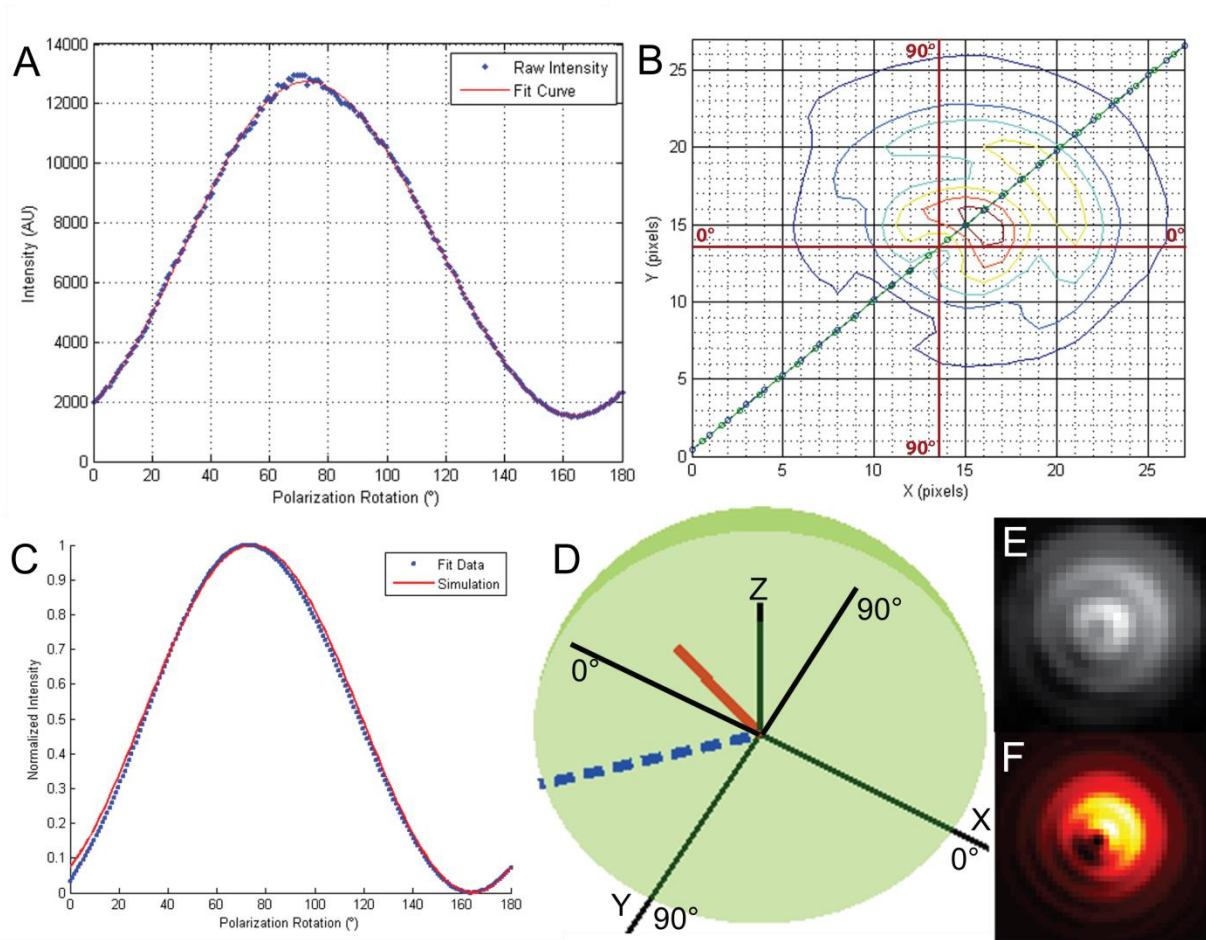


**Figure 4.** Data and representations of a single AuNR with a polar angle of  $23.4^\circ \pm 0.8^\circ$ . (A) Raw intensity versus the first  $180^\circ$  of rotation of the polarizer fit with a higher-order polynomial. (B) Representation of the azimuthal angle determination using the defocused image with the highest contrast. The angle was determined to be  $44.1^\circ \pm 0.9^\circ$  with respect to the  $x$ -axis. (C) Plot portraying the alignment of the data with the simulated curves. (D) 3D representation of the AuNR in space. (E) Actual defocused imaged taken at the polarization rotation angle of highest intensity. (F) Simulated image of a AuNR with the angles calculated for the particle.

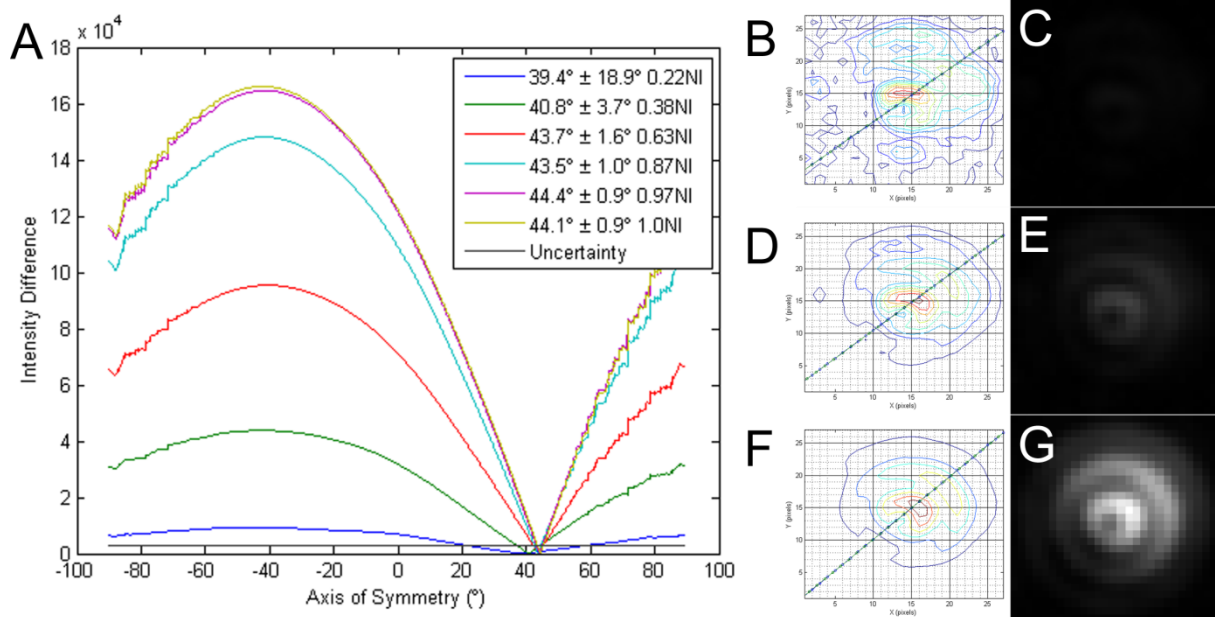


**Figure 5.** Representation of the dependence of azimuthal angle determination upon signal intensity. (A) Plots of the intensity difference for the symmetry axis determination of the same AuNR at six different total intensities. The yellow line represents the trace with the highest intensity, which was set to 1.0 normalized intensity (NI). The rest of the plots represent the symmetry determination for the same particle at different angles  $\zeta$ . The grey line represents the intensity level of uncertainty. (B) Surface plot of the lowest intensity symmetry determination (0.22NI) corresponding to the particle image (C). (D) and (E) are the surface plot and particle image corresponding to the 0.38NI plot, respectively. (F) and (G) are the surface plot and particle image corresponding to the 1.0NI plot, respectively.

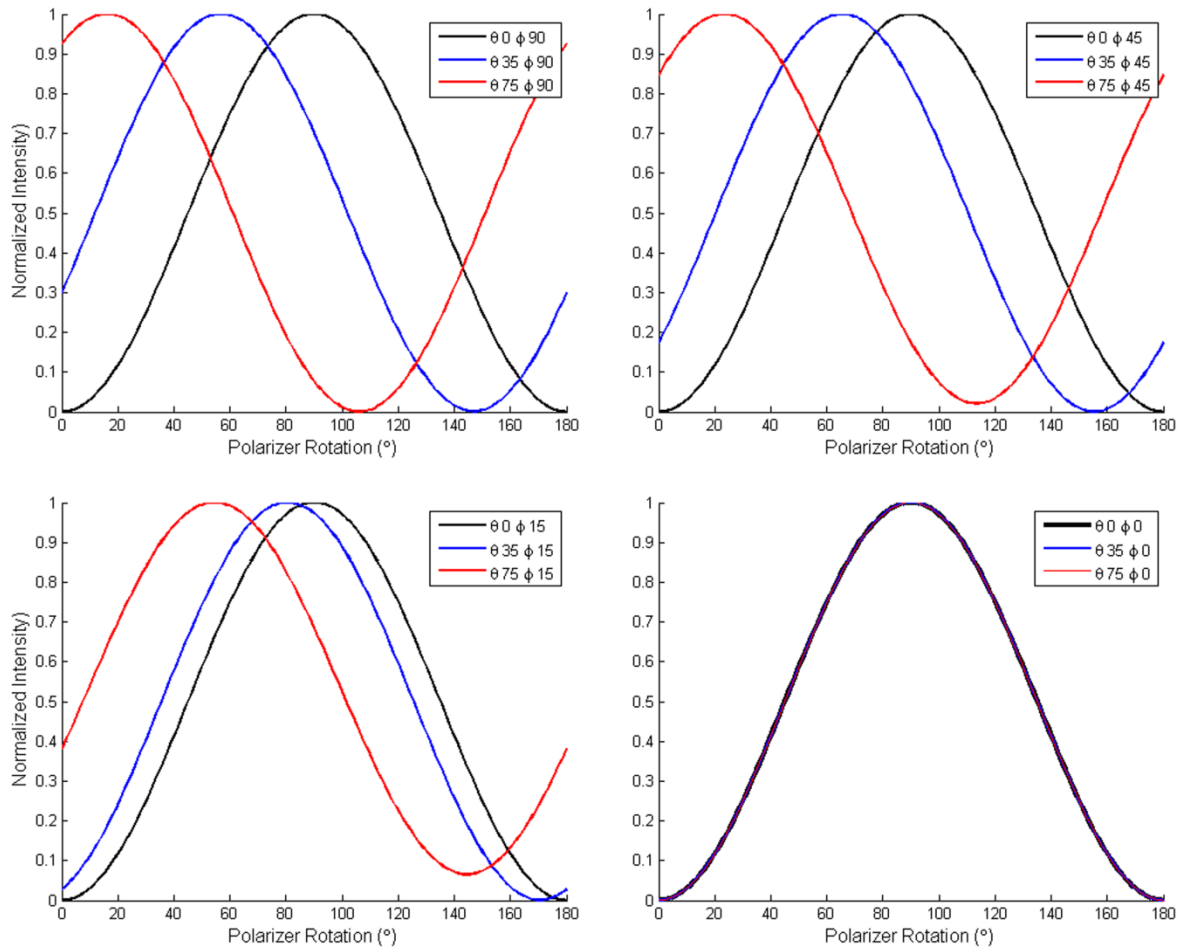


**Figure 6.** Simulated intensity profiles for various polar and azimuthal angles with respect to the incoming polarization direction.

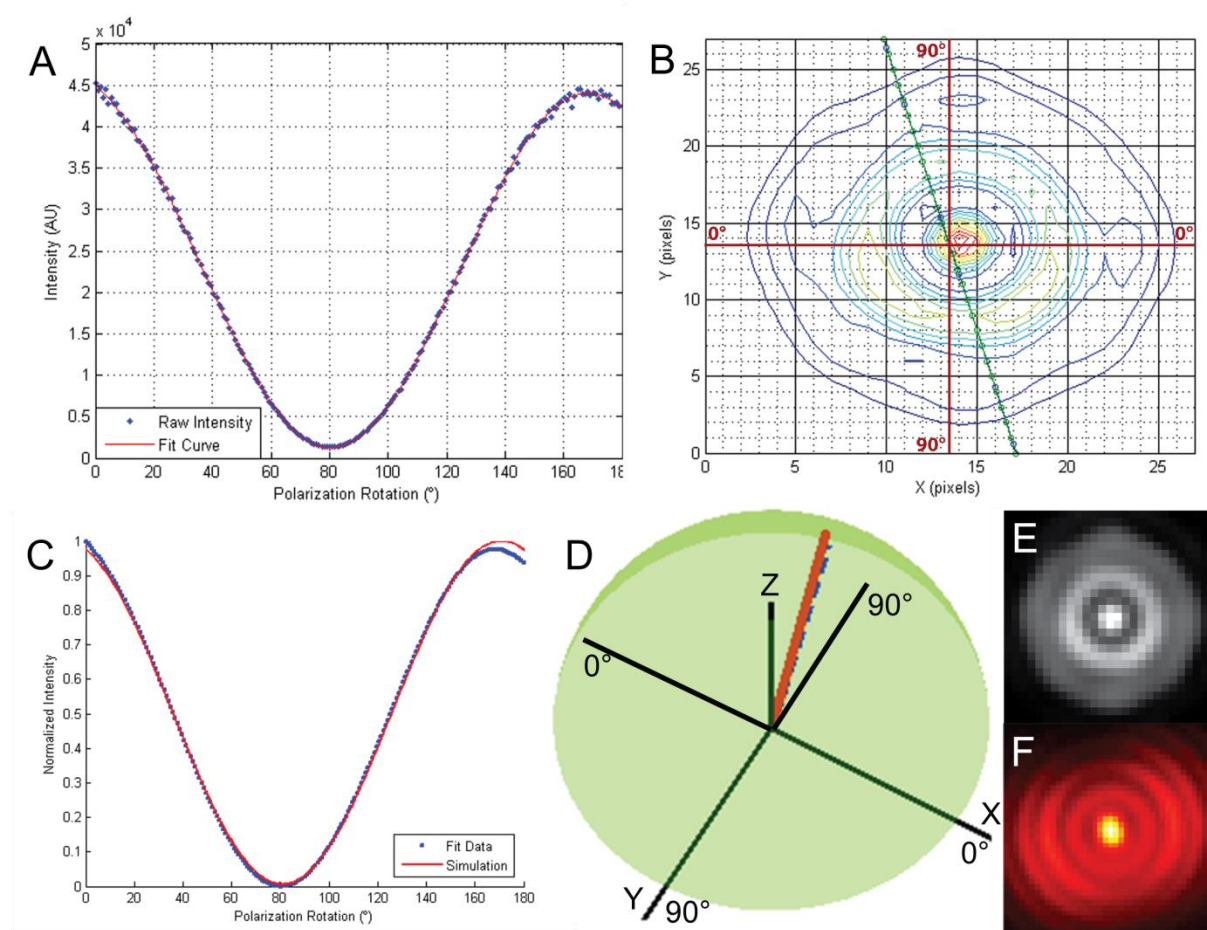


**Figure 7.** Data and representations of a single AuNR with a polar angle of  $81.5^\circ \pm 0.3^\circ$ . (A) Raw intensity versus the first  $180^\circ$  of rotation of the polarizer fit with a higher-order polynomial. (B) Representation of the azimuthal angle determination using the defocused image with the highest contrast. The angle was determined to be  $74.8^\circ \pm 2.7^\circ$  with respect to the  $x$ -axis. (C) Plot portraying the alignment of the data with the simulated curves. (D) 3D representation of the AuNR in space. (E) Actual defocused imaged taken at the polarization rotation angle of highest intensity. (F) Simulated image of a AuNR with the angles calculated for the particle.

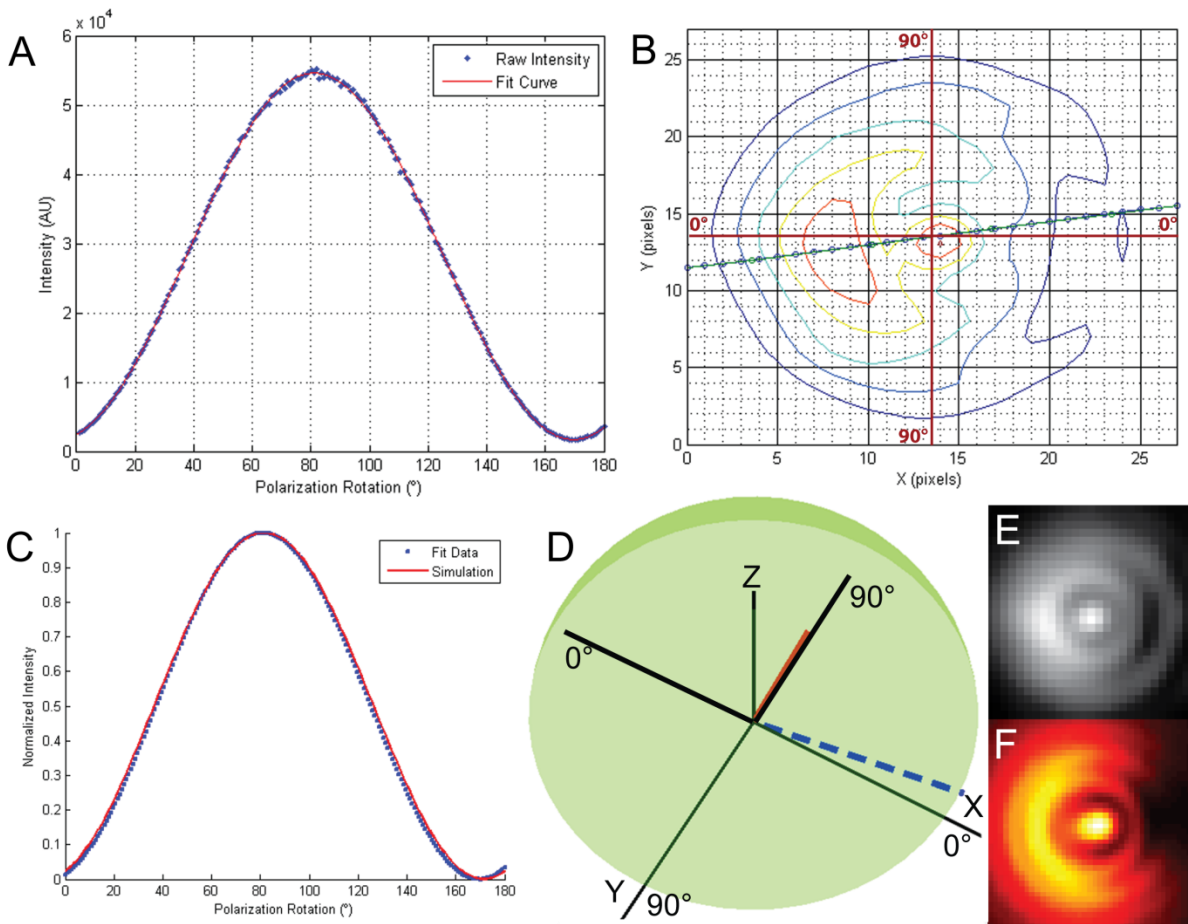


**Figure 8.** Data and representations of a single AuNR with a polar angle of  $48.3^\circ \pm 2.4^\circ$ . (A) Raw intensity versus the first  $180^\circ$  of rotation of the polarizer fit with a higher-order polynomial. (B) Representation of the azimuthal angle determination using the defocused image with the highest contrast. The angle was determined to be  $8.6^\circ \pm 0.4^\circ$  with respect to the  $x$ -axis. (C) Plot portraying the alignment of the data with the simulated curves. (D) 3D representation of the AuNR in space. (E) Actual defocused imaged taken at the polarization rotation angle of highest intensity. (F) Simulated image of a AuNR with the angles calculated for the particle.

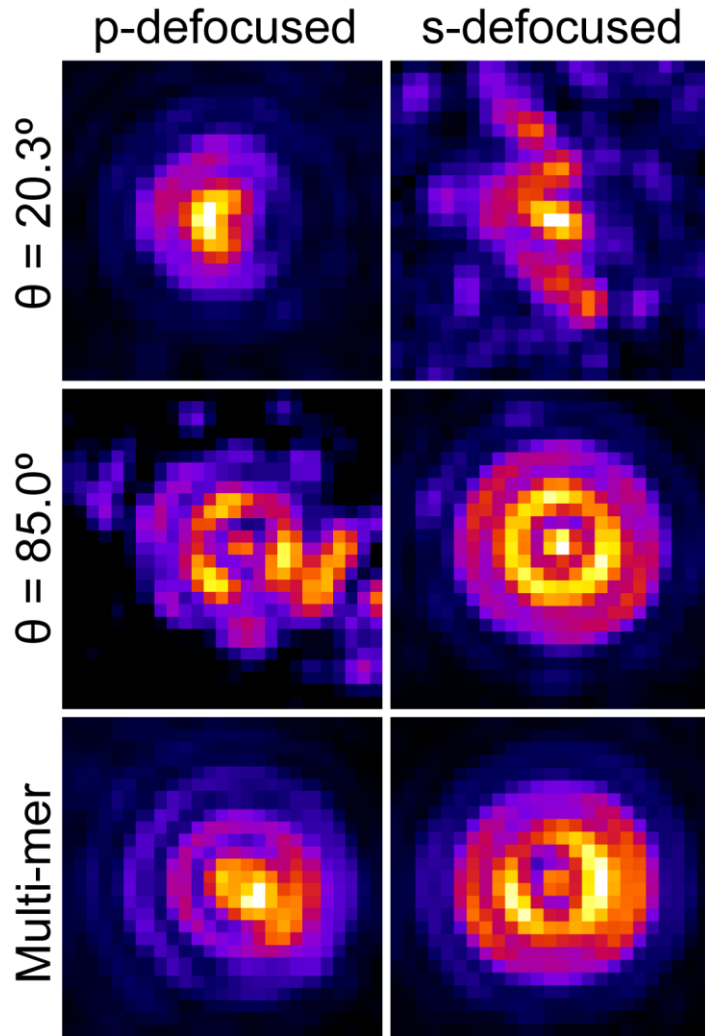


**Figure 9.** Comparison of single particle and possible multi-mer with defocused imaging at p-pol and s-pol illumination. The top row shows a single particle with a polar angle of  $20.3^\circ$  and the second row shows a single particle with a polar angle of  $85.0^\circ$ . The bottom row displays what is considered a multi-mer at the two polarization illuminations.

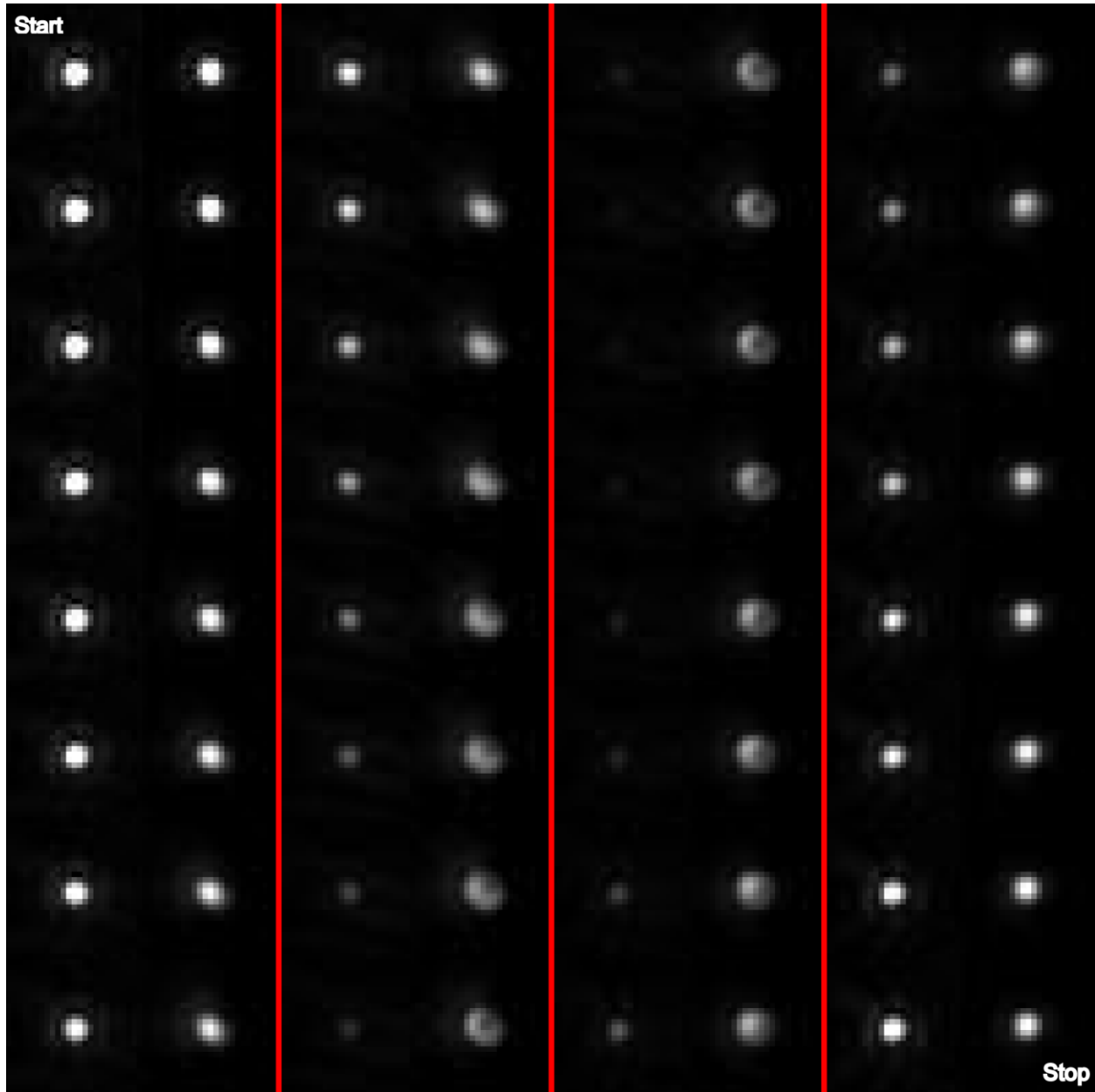


**Figure 10.** Comparison of a single AuNR (left spot) with a large polar angle to an aggregate (right spot) that appears to be a dimer throughout a 180° rotation of the polarization direction.



## CHAPTER 5: LASER NOMARSKI DIFFERENTIAL INTERFERENCE CONTRAST MICROSCOPY FOR THE INVESTIGATION OF NANOPARTICLES AND NANOSTRUCTURES ON REFLECTIVE SURFACES

### Abstract

Metallic nanoparticles and nanostructures are of much interest due to a broad range in applications such as optoelectronics, biosensing, and medical diagnostics amongst others. The fabrication of many of these materials is done through lithographic means typically taking place on reflective surfaces such as silicon wafers. The typical characterization methods such as SEM, TEM, and AFM are unable to directly study the optical properties of systems or follow dynamic events in real-time compared to optical microscopy techniques. Reflected mode Nomarski differential interference contrast (DIC) microscopy is introduced as a method of studying nanoparticle and nanostructures on reflective surfaces. Gold bowties, pyramids, and particle dimers fabricated within silicon wafer templates are imaged using reflected mode DIC microscopy.

### Introduction

The formation of metallic nanoparticles and nanostructures is fundamentally interesting due to their applications in electronics,<sup>1-3</sup> optoelectronics and plasmonics,<sup>4-10</sup> chemical sensing and biosensors,<sup>11-16</sup> and medical diagnostics and therapies.<sup>17-19</sup> The wide application of these particles and structures depends upon their optical, electronic, and catalytic properties that can be finely tuned over a broad range by controlling their size, shape, and composition.<sup>20-22</sup> While a bottom-up solution phase synthesis is a popular route to control the formation of nanoparticles,<sup>23-26</sup> top-down lithographic techniques offer highly reproducible routes for the synthesis of structures with tunable optical properties.<sup>27-29</sup> Many interesting particles and structures have been developed such as particle multi-mers,<sup>30</sup> pyramids,<sup>31</sup> bowties,<sup>32</sup> nanoholes,<sup>33, 34</sup> and many others.

The visualization and characterization of nanostructures is typically performed by a series of invasive or destructive microscopy techniques such as scanning electron microscopy (SEM), transmission electron microscopy (TEM), and atomic force microscopy (AFM),<sup>35</sup> While these



techniques provide high-resolution images, little information about the optical characteristics can be gathered directly. In addition, surface characterization techniques do not have the ability to follow dynamic processes in real-time as compared to optical microscopy techniques such as total internal reflection scattering (TIRS) microscopy<sup>36, 37</sup> and dark-field microscopy,<sup>31, 38</sup> which have been applied to the study of both the optical characterization of nanoparticles/nanostructures and the investigation into real-time dynamics.

Another optical technique known as differential interference contrast (DIC) microscopy uses interferometry to image unstained transparent samples. Also known as Nomarski interference contrast (NIC) microscopy due to the use of specific prisms,<sup>39</sup> DIC works by using a birefringent Nomarski prism to split polarized incident light into two orthogonal wavefronts both angled 45° to an incident polarizer and separated by what is known as the shear distance. These wavefronts then pass through an analyzer and interact with the sample. Depending on the position of the wavefronts to the sample, a phase delay may develop between the orthogonal beams. After passing through the objective, a second Nomarski prism is then used to recombine the light introducing either constructive or destructive interference. A second polarizer is then set at extinction to block all non-interfering light. The result is a grey background on which the sample appears as a shadow-cast relief. While other forms of DIC have been developed, the Nomarski configuration has been proven most popular due the use of a large condenser aperture that lends itself to increased lateral resolution and produces a shallower depth of field.<sup>40</sup>

DIC microscopy is advantageous for biological applications since there is no need for fluorescent labels. In 2008 Tsunoda, *et al.* directly compared DIC, bright-field, and dark-field microscopy of a single cell demonstrating the advantages of DIC for its minimization of interference from cell features found outside the focal plane.<sup>41</sup> Without the need for staining, observations can last for several hours with minimal intrusion to the biological system. This technique enabled the simultaneous observation of both nanoparticles and a cancer cell during the endocytosis process,<sup>42</sup> and the recording of 40 nm gold nanospheres going through endocytosis.<sup>43</sup>

Since it can visualize nanoparticles, DIC microscopy also lends itself to single particle orientation and rotation tracking (SPORT).<sup>44</sup> Within the surface plasmon resonance (SPR) wavelengths, an isotropic nanoparticle will have a consistent appearance no matter the orientation of the particles in relation to the polarizer. The rotation of an anisotropic nanoparticle,

on the other hand, will change in appearance between appearing all dark, as a shadow-effect, and all bright depending on orientation. The intensity ratio between the bright and dark part of the particle have a periodic  $\cos^4$  and  $\sin^4$  relationship, respectively that can be used to monitor rotational dynamics on a cell membrane,<sup>45</sup> and investigate the rotational motions of cargo during intracellular transport.<sup>46</sup>

While the DIC configuration previously described is an ideal microscope to study systems on transparent substrates, most nanoparticles and nanostructures created through lithographic techniques are made on reflective surfaces such as silicon wafers. In 1979 Lessor *et al.* developed the reflected Nomarski DIC (rDIC) configuration and applied it towards surface topography studies.<sup>47</sup> The rDIC configuration is simpler in the aspect that it has fewer optical components to align. The condenser works also as the objective and only one Nomarski prism is needed as it both shears the light directed at the sample and recombines the light reflected back through the objective. One additional component, a beamsplitter, is used to direct the signal towards the camera. Traditionally, rDIC has been used to both qualitatively and quantitatively report surface roughness while studying polishing techniques, but it has also found much use in visualizing details and defects in semiconductor chips made on silicon wafers. Herein, a benchtop configured laser-source Nomarski rDIC is described that has been applied to the study of nanostructures on silicon wafer substrates.

## Results and Discussion

The design of the microscope included a laser as the light-source. Lasers are incorporated into many microscopic techniques such as total internal reflection fluorescence (TIRF) microscopy, TIRF microscopy, light-sheet microscopy, two-photon excitation microscopy, and STED microscopy. The advantages of utilizing a laser compared to other bulb-based light sources (mercury vapor, etc.) include monochromatic light, minimal beam divergence, optical coherence, and highly focused beam intensity.

Unlike the aforementioned microscopy techniques, rDIC (and DIC) needs to contend with laser speckling (visualized in Figure 1A and 1C). This intensity pattern arises due to the interference of wavefronts as the laser is directed through optics and off surfaces. In the case of fluorescence microscopy such as TIRF microscopy, light-sheet microscopy, and STED microscopy, laser speckle is not observed since the collected signal arises from fluorescence.

Speckle does not arise in TIRS microscopy either since the scattering signal is produced by an evanescent field.

The first attempts to reduce laser speckle involved rotating a diffuser. Diffusers are typically composed of polycarbonate or glass that homogenizes the light creating uniform illumination. Incoming light passes through the material and scatters to various extents in which large angle diffusers produce the greatest degree of homogenized light. Using a diffuser by itself only changes the speckle pattern, but passing the laser light through a rotating diffuser changes the path length by a small amount thus affecting the speckle pattern. The effect of laser speckle can be nearly eliminated by quickly spinning the diffuser and using longer exposure times when viewing through a camera. Spinning the diffuser fast enough with a long camera exposure time allows for the diffuser movement to average the background allowing the samples to be observed.

Two issues arose while using the rotating diffuser method. The first had to do with uneven background averaging. The diffuser pattern is essentially projected onto the imaging area. This means the area of the image with the diffuser farthest from its center of rotation will experience the largest averaging of the background. While the diffuser can be spun at a rate that makes the difference in background arbitrarily small, there are arc-like features that show up on the image that look like “streaks”. This is caused by the same pattern of the diffuser being spun across the same area of the image and will compound itself based on exposure time and image stacking.

The second diffuser issue is much more significant. DIC microscopy requires polarized collimated light in order to produce the interferometry patterns. While the light continues to have a high degree of polarization after passing through the diffuser, all spatial coherence is lost. Diffusers that have a large enough degree of diffusion to homogenize the background are unable to be properly re-collimated into a suitable illumination source for DIC without significant loss of light.

To counter these problems, a fiber-optic light scrambler (Technical Video LTD, FJJB#219) was used to produce collimated light that could also produce an averaged background. The propagation of light through an optical fiber is based upon the total internal reflection of the lightwave. Rough and irregular surfaces or a bend in the cable will cause the light rays to be reflected in random angles. This is called diffuse reflection or scattering and

produces unpolarized and spatially incoherent light. Fiber-optics can be collimated using a series of lenses placed at the proper distance from the end of the cable. The fiber-optic incorporated into the microscope has two lenses at the optical output that produces nearly collimated light. With the addition of a single 15 cm focal length lens complete collimation was achieved.

The light scrambler itself does nothing to reduce laser speckle as the path length stays consistent for the passing light. Moving the fiber-optic cable slightly changes the light path of the passing light thus changing the speckle pattern observed on the image. A Vibrabeam (Elforlight Ltd) was attached to the cable, which randomly moves the fiber-optic cable producing rapidly changing speckle patterns allowing for an unbiased background averaging. Examples of the improved image quality while using the Vibrabeam can be seen in Figure 1. Comparisons were made using 10  $\mu\text{m}$  and 400 nm diameter polystyrene beads.

The fiber-optic light scrambler has additional benefits in our setup. With the addition of a polarizer, the polarization direction of the laser light can be easily directed to the proper orientation in relation to the Nomarski prism. Also, since the input of the optical fiber can be aligned separately from the output, alignment of new laser sources is a simple matter that does not affect the crucial DIC components.

The representation of the rDIC can be seen in Figure 2. A 45-mW 532-nm continuous wave linearly polarized laser (Uniphase, San Jose, CA) is directed to periscope optics, through a Uniblitz mechanical shutter (model #LS2Z2, Vincent Associates, Rochester, NY) and into the fiber-optic light scrambler (Technical Video LTD, FJJB#219). The internal optics are set to produce the most collimated light output that is then directed at a 25.4 mm diameter 15-cm focal length lens. A polarizer (Edmund Optics, Barrington, NJ, model 54-926) is set to  $45^\circ$  from vertical to produce even intensity orthogonally polarized beams passing through the Nomarski prism. A 50/50 beamsplitter (Thorlabs, Newton, NJ, BSW10) passes light towards the condenser/objective (Zeiss, UltraFluor 100x 1.20 Gly,  $\infty/0.20$  Qu), which then focuses and collects the reflected light from the silicon wafer substrate. The substrate is supported by a homemade stage capable of two-dimensional translation. The reflected light is next directed by the beam splitter through a second polarizer set at extinction and on to the CCD (Photometrics CoolSnap ES).

Using this setup, images of both polystyrene microbeads and gold nanospheres were imaged. To prepare the microbead samples, a drop of sample solution was placed directly on the

silicon wafer and evenly distributed across the surface. The solution was allowed to dry before a drop of immersion oil (Zeiss, Immersol,  $n=1.518$ ) was placed upon the beads. A 22 mm x 50 mm No. 1 Corning coverslip was then placed upon the sample and sealed by enamel. The samples were then placed onto the microscope stage and a drop of immersion glycerin was placed between the objective and sample. Images of 10  $\mu\text{m}$  and 400 nm in diameter beads can be seen in Figure 2B and Figure 2D, respectively. Both examples display the characteristic shadow-cast appearance found in DIC microscopy.

Gold nanosphere samples were prepared in the following manner. Silicon wafers were modified with (3-aminopropyl)triethoxysilane (APTES) (Sigma-Aldrich) by submerging the wafer in 1.5% (v/v) APTES in acetone for 1 hour at 37° C. The slide was then rinsed in pure acetone to remove excess APTES and placed in an oven for 1 hour at 107° C. Gold nanospheres (BBI Solutions) were diluted 5x in 18M $\Omega$  MilliQ water and sonicated for 30 min. Solution was then deposited on the APTES modified silicon wafer and sandwiched by a 25 mm<sup>2</sup> Corning coverslip. The sample was sealed with enamel and placed on the microscope slide with immersion glycerol.

As can be seen in Figure 3, 80 nm and 60 nm in diameter gold spheres can easily be imaged by our microscope with an exposure time set to 50 ms. Figure 3C is an example of imaging 40 nm gold spheres with a single exposure of 50 ms. The particles do not become apparent until images are stacked. Figure 3D is the same area as shown in Figure 3C with 20 images stacked. The particles can now easily be seen. Like the polymer beads, these gold particles display the characteristic DIC shadow-effect image with a half-dark half-bright pattern transposed onto a gray background. Since the particles are isotropic in shape, the patterns are identical for all the spheres in the images.

Anisotropic gold nanorods (AuNRs) display a distinct pattern under DIC microscopy that can be used for orientation determination<sup>44, 48</sup> and rotational studies<sup>44-46</sup>. Depending on the orientation of the long axis of the particles, the intensity of the bright and dark patterns of the particle can vary from the particle appearing entirely bright, to half dark and half bright, to entirely dark. AuNRs with dimensions of 40 x 118 nm (Nanopartz, Loveland, CO) with an axial surface plasmon resonance (SPR) peak at 540 nm were imaged. The AuNRs were modified with transferrin to produce a net negative charge. The solution was then placed on an APTES

modified silicon wafer, sandwiched with a 25 mm<sup>2</sup> Corning coverslip, sealed with enamel, and placed upon the microscope.

Figure 4A depicts the sum of 20 images exposed for 50 ms of the 40 x 118 nm AuNRs under 532-nm illumination. The particles exhibit a range of patterns due to their random orientations upon the surface. The single AuNRs in Figure 4B-F depicts nanorods at different orientations in the plane of the substrate. It has previously been demonstrated that the three-dimensional (3D) orientation of AuNRs can be determined from their DIC patterns.<sup>49</sup> Within the imaged area there are particles exhibiting the patterns of AuNRs that have a polar angle smaller than 90°. Figure 4G-K shows examples of patterns produced by AuNRs in random 3D orientations.

The aforementioned examples have all been of particles placed upon a reflective surface. Figure 5 displays nanoparticles created on silicon wafers through lithographic means. The three types of particles displayed (nanorod dimers, bowties, and pyramids) were created in a pyramidal template that was etched into the substrate. The substrate can be seen in the SEM images (Figure 5A and 5B) surrounding the particles. The blank template is visualized under rDIC and seen in Figure 5C. Due to the pyramidal structure of the template, the path difference the light takes entering and reflecting off the substrate gives rise to the DIC pattern. Imaging the template can be considered a study of the surface topography much like the original microscopes were used for.

Figure 5A and 5D are SEM and rDIC images, respectively, of gold particle dimers made within the template. The particles are each 100 nm x 60 nm x 35 nm in size. Compared to the rDIC image of the template, a sharper contrast arises between the “columns” while the periodic “rows” tend to blend together. The orientation of the rDIC image corresponds to that of the SEM. The change in contrast indicates an optical response from the dimers.

Gold bowties were also imaged under rDIC (Figure 5E). The periodic array and orientation can be seen in the corresponding SEM image in Figure 5B. The optical response in the rDIC image depicts a more classical DIC image showing what appears to be contrast relief. Though there is an obvious periodic spacing in the SEM image, the DIC appears somewhat random. This may be due to the optical response of the individual halves of the bowties structure and the proximity of the structures. The distance separating structures is less than the diffraction limit of the microscope, which may be cause for the interesting patterns.

Gold pyramids in the template were imaged in Figure 5F (no corresponding SEM). The images show a periodic array of half-dark half-bright particles. The optical response is most similar to that of the empty template with a periodic array of columns and rows. The images indicate that rDIC is capable of detecting the patterning of difference materials on a reflective surface.

## Conclusions

It has been demonstrated that a laser-source rDIC microscope benchtop configuration has been built that can study nanoparticles and nanomaterials on a reflective surface. The method of reducing laser speckle allows for quality DIC imaging. Gold nanospheres as small as 40 nm and the different patterns resulting from the random 3D orientations of AuNRs could be easily imaged. Gold nanostructures such as pyramids, dimers, and bowties created in silicon wafer templates were also imaged, each producing a different optical response.

It is expected that rDIC will become a common tool in characterizing nanofabrication on reflective surface as an alternative to more expensive methods such as SEM, TEM, and AFM. Optical microscopy such as rDIC also allows for the observation of dynamic processes such as self-assembly or monitoring the stability of structures in changing conditions. Reflected DIC will also be a useful technique for the observation of molecular and nanomachines within engineered environments.

## References

1. Ko, S. H.; Park, I.; Pan, H.; Grigoropoulos, C. P.; Pisano, A. P.; Luscombe, C. K.; Frechet, J. M. J. *Nano Letters* 2007, 7, (7), 1869-1877.
2. Herderick, E. D.; Tresback, J. S.; Vasiliev, A. L.; Padture, N. P. *Nanotechnology* 2007, 18, (15).
3. Bluemel, A.; Klug, A.; Eder, S.; Scherf, U.; Moderegger, E.; List, E. J. W. *Organic Electronics* 2007, 8, (4), 389-395.
4. Ozbay, E. *Science* 2006, 311, (5758), 189-193.
5. Oldenburg, S. J.; Jackson, J. B.; Westcott, S. L.; Halas, N. J. *Applied Physics Letters* 1999, 75, (19), 2897-2899.



6. Maier, S. A.; Atwater, H. A. *Journal of Applied Physics* 2005, 98, (1).
7. Bozhevolnyi, S. I.; Volkov, V. S.; Devaux, E.; Laluet, J. Y.; Ebbesen, T. W. *Nature* 2006, 440, (7083), 508-511.
8. Yin, L. L.; Vlasko-Vlasov, V. K.; Pearson, J.; Hiller, J. M.; Hua, J.; Welp, U.; Brown, D. E.; Kimball, C. W. *Nano Letters* 2005, 5, (7), 1399-1402.
9. Lal, S.; Hafner, J. H.; Halas, N. J.; Link, S.; Nordlander, P. *Accounts of Chemical Research* 2012, 45, (11), 1887-1895.
10. Chang, W.-S.; Lassiter, J. B.; Swanglap, P.; Sobhani, H.; Khatua, S.; Nordlander, P.; Halas, N. J.; Link, S. *Nano Letters* 2012, 12, (9), 4977-4982.
11. Haes, A. J.; Haynes, C. L.; McFarland, A. D.; Schatz, G. C.; Van Duyne, R. R.; Zou, S. *L. Mrs Bulletin* 2005, 30, (5), 368-375.
12. Brolo, A. G.; Gordon, R.; Leathem, B.; Kavanagh, K. L. *Langmuir* 2004, 20, (12), 4813-4815.
13. Liu, J. W.; Lu, Y. *Angewandte Chemie-International Edition* 2006, 45, (1), 90-94.
14. Lee, J.-S.; Han, M. S.; Mirkin, C. A. *Angewandte Chemie-International Edition* 2007, 46, (22), 4093-4096.
15. Haes, A. J.; Chang, L.; Klein, W. L.; Van Duyne, R. P. *Journal of the American Chemical Society* 2005, 127, (7), 2264-2271.
16. Lin, J. Y.; Stuparu, A. D.; Huntington, M. D.; Mrksich, M.; Odom, T. W. *The Journal of Physical Chemistry C* 2013, 117, (10), 5286-5292.
17. Chen, J.; Wang, D.; Xi, J.; Au, L.; Siekkinen, A.; Warsen, A.; Li, Z.-Y.; Zhang, H.; Xia, Y.; Li, X. *Nano Letters* 2007, 7, (5), 1318-1322.
18. Loo, C.; Lowery, A.; Halas, N. J.; West, J.; Drezek, R. *Nano Letters* 2005, 5, (4), 709-711.
19. Huang, X. H.; El-Sayed, I. H.; Qian, W.; El-Sayed, M. A. *Journal of the American Chemical Society* 2006, 128, (6), 2115-2120.
20. Lee, K.-S.; El-Sayed, M. A. *Journal of Physical Chemistry B* 2006, 110, (39), 19220-19225.
21. Kelly, K. L.; Coronado, E.; Zhao, L. L.; Schatz, G. C. *Journal of Physical Chemistry B* 2003, 107, (3), 668-677.
22. Murphy, C. J.; Sau, T. K.; Gole, A.; Orendorff, C. J. *Mrs Bulletin* 2005, 30, (5), 349-355.



23. Hostetler, M. J.; Wingate, J. E.; Zhong, C. J.; Harris, J. E.; Vachet, R. W.; Clark, M. R.; Londono, J. D.; Green, S. J.; Stokes, J. J.; Wignall, G. D.; Glish, G. L.; Porter, M. D.; Evans, N. D.; Murray, R. W. *Langmuir* 1998, 14, (1), 17-30.
24. Wiley, B.; Sun, Y. G.; Mayers, B.; Xia, Y. N. *Chemistry-a European Journal* 2005, 11, (2), 454-463.
25. Chen, H. M.; Hsin, C. F.; Liu, R.-S.; Lee, J.-F.; Jang, L.-Y. *Journal of Physical Chemistry C* 2007, 111, (16), 5909-5914.
26. Lu, X.; Tuan, H.-Y.; Chen, J.; Li, Z.-Y.; Korgel, B. A.; Xia, Y. *Journal of the American Chemical Society* 2007, 129, (6), 1733-1742.
27. Gunnarsson, L.; Rindzevicius, T.; Prikulis, J.; Kasemo, B.; Kall, M.; Zou, S. L.; Schatz, G. C. *Journal of Physical Chemistry B* 2005, 109, (3), 1079-1087.
28. Su, K. H.; Wei, Q. H.; Zhang, X.; Mock, J. J.; Smith, D. R.; Schultz, S. *Nano Letters* 2003, 3, (8), 1087-1090.
29. Rechberger, W.; Hohenau, A.; Leitner, A.; Krenn, J. R.; Lamprecht, B.; Aussenegg, F. R. *Optics Communications* 2003, 220, (1-3), 137-141.
30. Stoerzinger, K. A.; Lin, J. Y.; Odom, T. W. *Chemical Science* 2011, 2, (8), 1435-1439.
31. Sweeney, C. M.; Stender, C. L.; Nehl, C. L.; Hasan, W.; Shuford, K. L.; Odom, T. W. *Small* 2011, 7, (14), 2032-2036.
32. Suh, J. Y.; Huntington, M. D.; Kim, C. H.; Zhou, W.; Wasielewski, M. R.; Odom, T. W. *Nano Letters* 2011, 12, (1), 269-274.
33. Gao, H.; Hyun, J. K.; Lee, M. H.; Yang, J.-C.; Lauhon, L. J.; Odom, T. W. *Nano Letters* 2010, 10, (10), 4111-4116.
34. Yang, J.-C.; Gao, H.; Suh, J. Y.; Zhou, W.; Lee, M. H.; Odom, T. W. *Nano Letters* 2010, 10, (8), 3173-3178.
35. Stewart, M. E.; Anderton, C. R.; Thompson, L. B.; Maria, J.; Gray, S. K.; Rogers, J. A.; Nuzzo, R. G. *Chemical Reviews* 2008, 108, (2), 494-521.
36. Koen, K. A.; Weber, M. L.; Mayer, K. M.; Fernandez, E.; Willets, K. A. *The Journal of Physical Chemistry C* 2012, 116, (30), 16198-16206.
37. Marchuk, K.; Ha, J. W.; Fang, N. *Nano Letters* 2013, 13, (3), 1245-1250.
38. Sonnichsen, C.; Alivisatos, A. P. *Nano Letters* 2005, 5, (2), 301-304.

39. Pluta, M., *Advanced Light Microscopy*. Elsevier Science Publishing Co. Inc.: New York, 1989; Vol. 2.
40. Mehta, S. B.; Sheppard, C. J. R. *Optics Express* 2008, 16, (24), 19462-19479.
41. Tsunoda, M.; Isailovic, D.; Yeung, E. S. *Journal of Microscopy* 2008, 232, (2), 207-211.
42. Sun, W.; Fang, N.; Trewyn, B. G.; Tsunoda, M.; Slowing, I. I.; Lin, V. S. Y.; Yeung, E. S. *Analytical and Bioanalytical Chemistry* 2008, 391, (6), 2119-2125.
43. Sun, W.; Wang, G. F.; Fang, N.; Yeung, E. S. *Analytical Chemistry* 2009, 81, (22), 9203-9208.
44. Wang, G. F.; Sun, W.; Luo, Y.; Fang, N. *Journal of the American Chemical Society* 2010, 132, (46), 16417-16422.
45. Gu, Y.; Sun, W.; Wang, G. F.; Fang, N. *Journal of the American Chemical Society* 2011, 133, (15), 5720-5723.
46. Gu, Y.; Sun, W.; Wang, G.; Jeftinija, K.; Jeftinija, S.; Fang, N. *Nature Communications* 2012, 3.
47. Lessor, D. L.; Hartman, J. S.; Gordon, R. L. *Journal of the Optical Society of America* 1979, 69, (2), 357-366.
48. Stender, A. S.; Wang, G. F.; Sun, W.; Fang, N. *Acs Nano* 2010, 4, (12), 7667-7675.
49. Xiao, L.; Ha, J. W.; Wei, L.; Wang, G.; Fang, N. *Angewandte Chemie-International Edition* 2012, 51, (31), 7734-7738.

## Figures

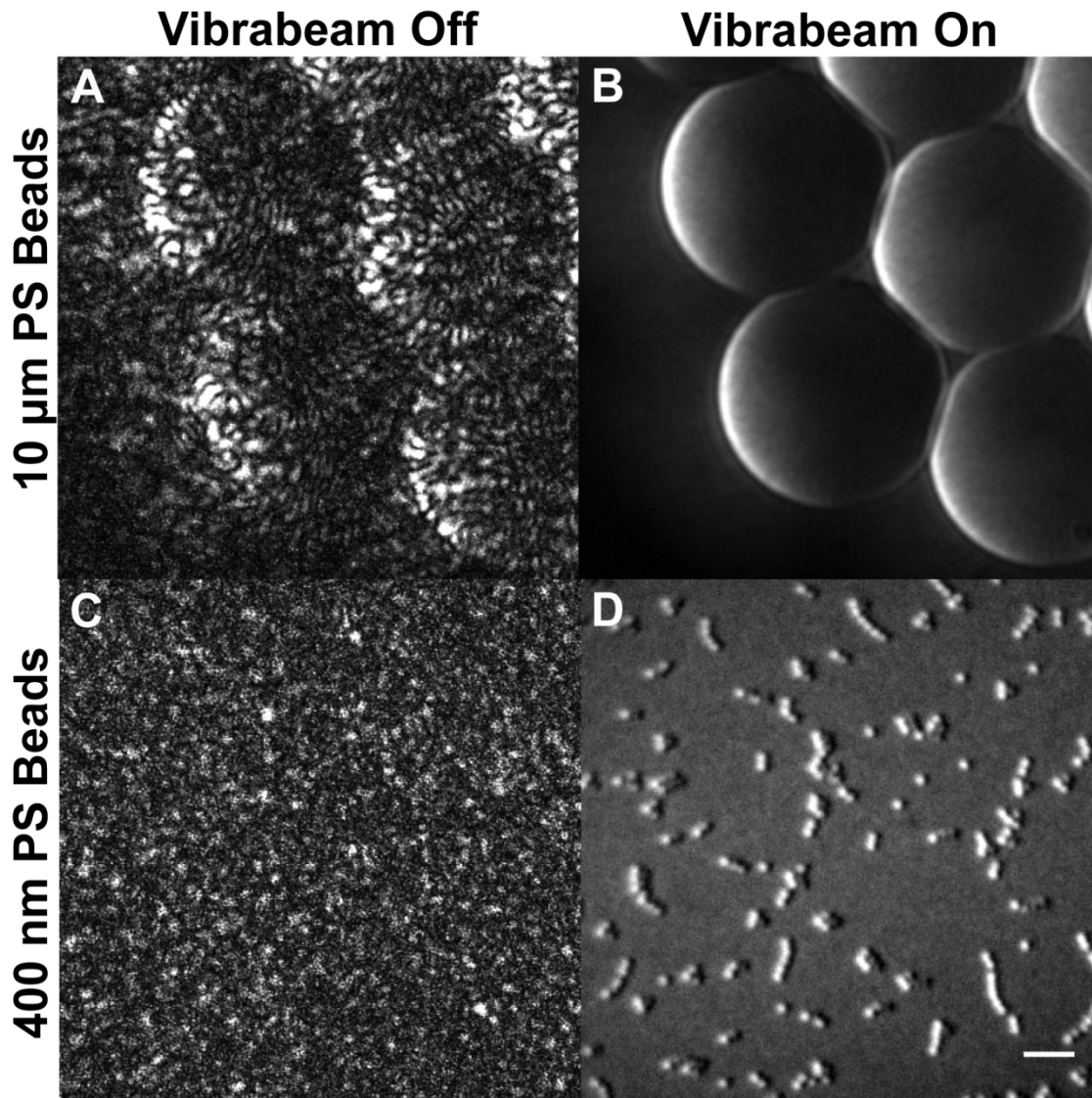


**Figure 1.** Examples of laser speckle and the influence the Vibrabeam has on signal averaging. (A) 10  $\mu\text{m}$  diameter polystyrene (PS) beads with the Vibrabeam turned off. (B) Same particles as seen in (A) with the Vibrabeam turned on. 400 nm diameter polystyrene beads with the off (C) and on (D). Scale bar is 2  $\mu\text{m}$ .

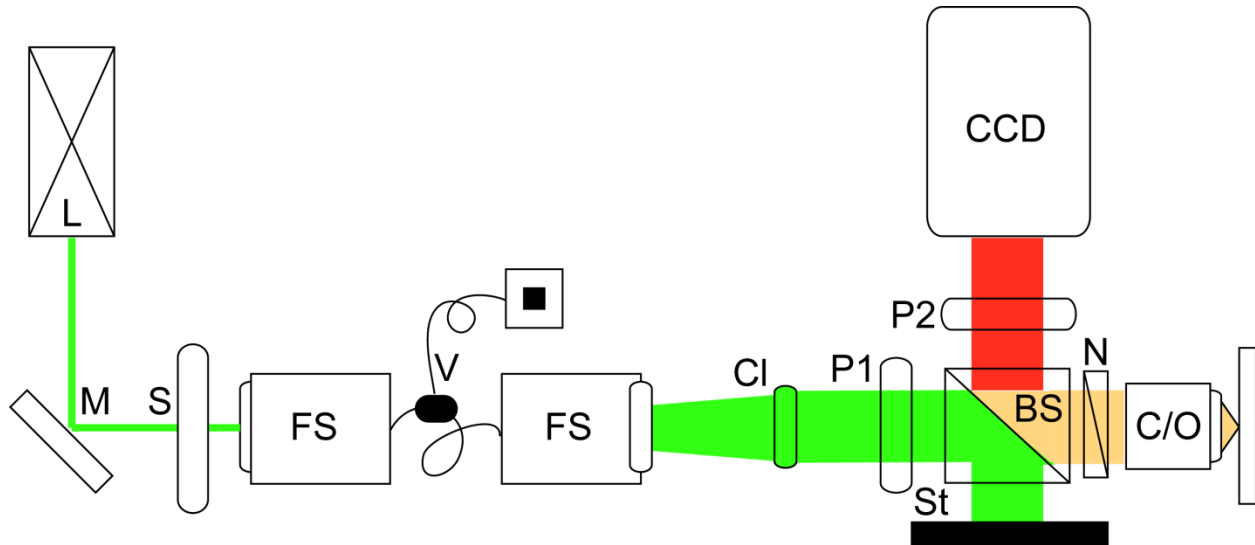


**Figure 2.** Illustration of rDIC setup. Illumination starts from the laser (L) and is directed by the mirror (M) through a shutter (S) and into the fiber-optic scrambler (FS). The Vibrabeam (V) quickly moves the fiber-optic randomly to average the background reducing the laser speckle. The light leaves the fiber-optic scrambler and is collimated by a lens (Cl). The light then passes through the first polarizer (P1) and is split by the beam splitter (BS). Half the light is directed to a beam stop (St), and the other half is directed through the Nomarski prism (N). Light then focused by the condenser/objective (C/O) onto the sample. The substrate reflects the light back through the condenser/objective, which reflects the signal through the second polarizer (P2) and into the camera (CCD).

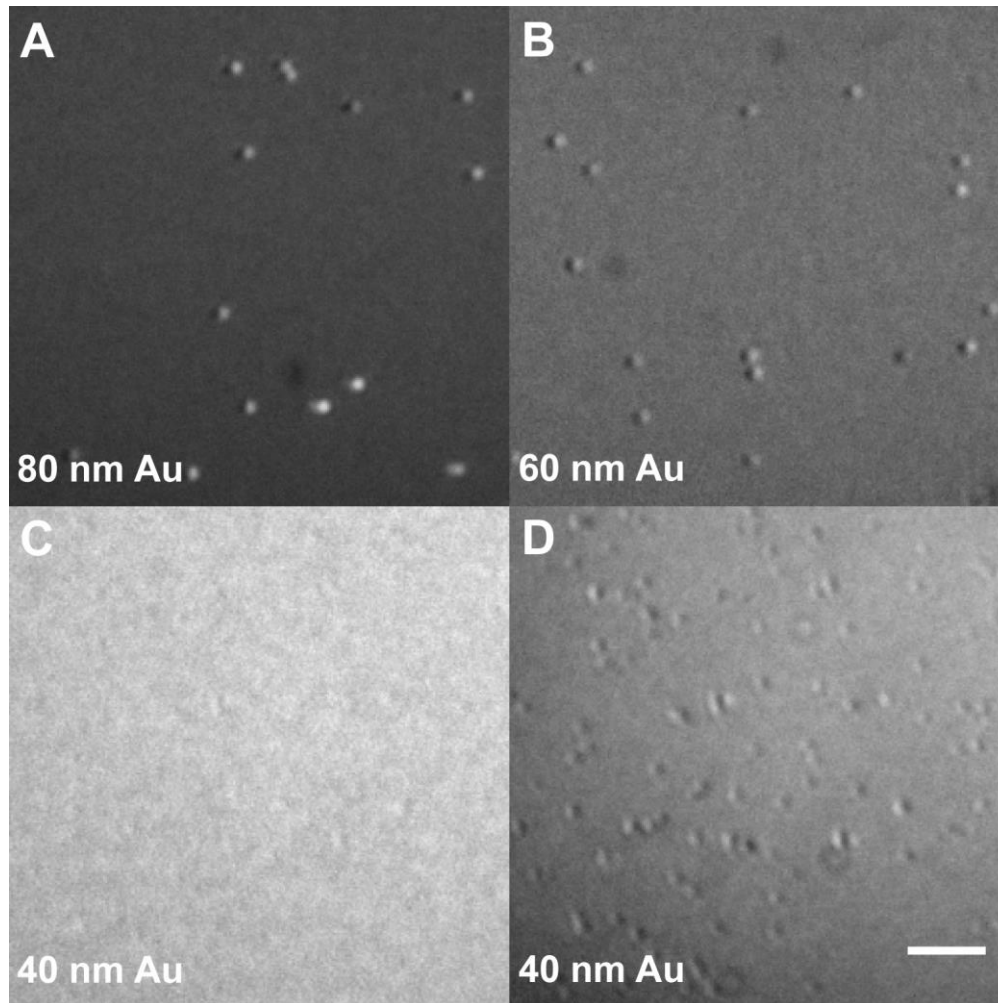


**Figure 3.** Examples of gold nanospheres imaged under rDIC. (A-C) correspond to 80 nm, 60 nm, and 40 nm in diameter particles respectively. (D) is the same area as (C) with 20 images summed. All exposure times are 50 ms. Scale bar is 2  $\mu\text{m}$ .

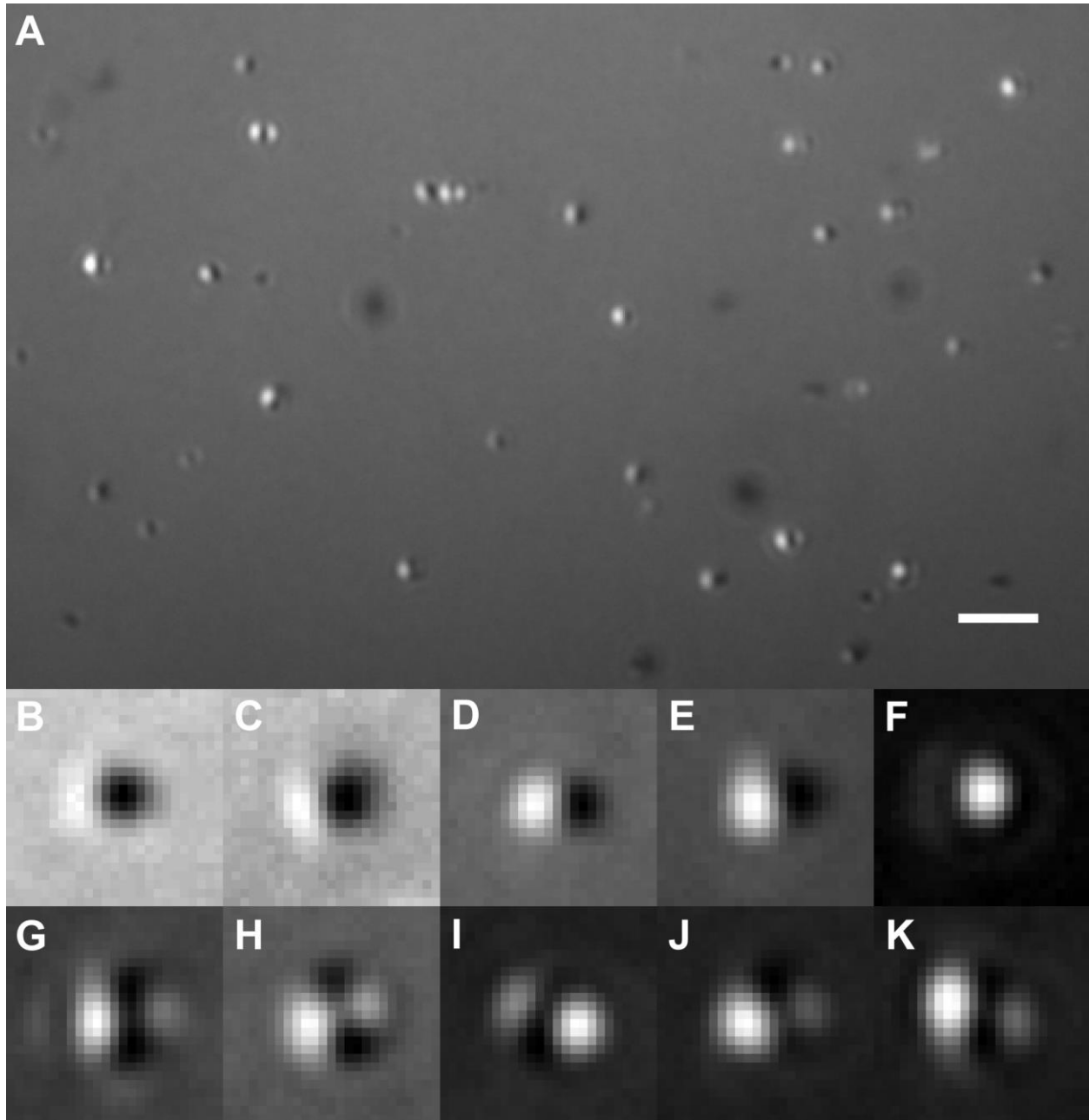


**Figure 4.** Gold nanorods (40x118 nm) imaged under rDIC. (A) Random assortment of AuNRs with different 3D orientations. (B-F) Examples of AuNRs with different in-plane orientations. Patterns range from nearly completely dark to nearly completely bright. (G-F) Examples of AuNRs with different 3D orientations. The positions of the dark and bright “lobes” are orientation dependent. All images are the sum of 20 frames exposed for 50 ms. Scale bar is 2  $\mu\text{m}$ .



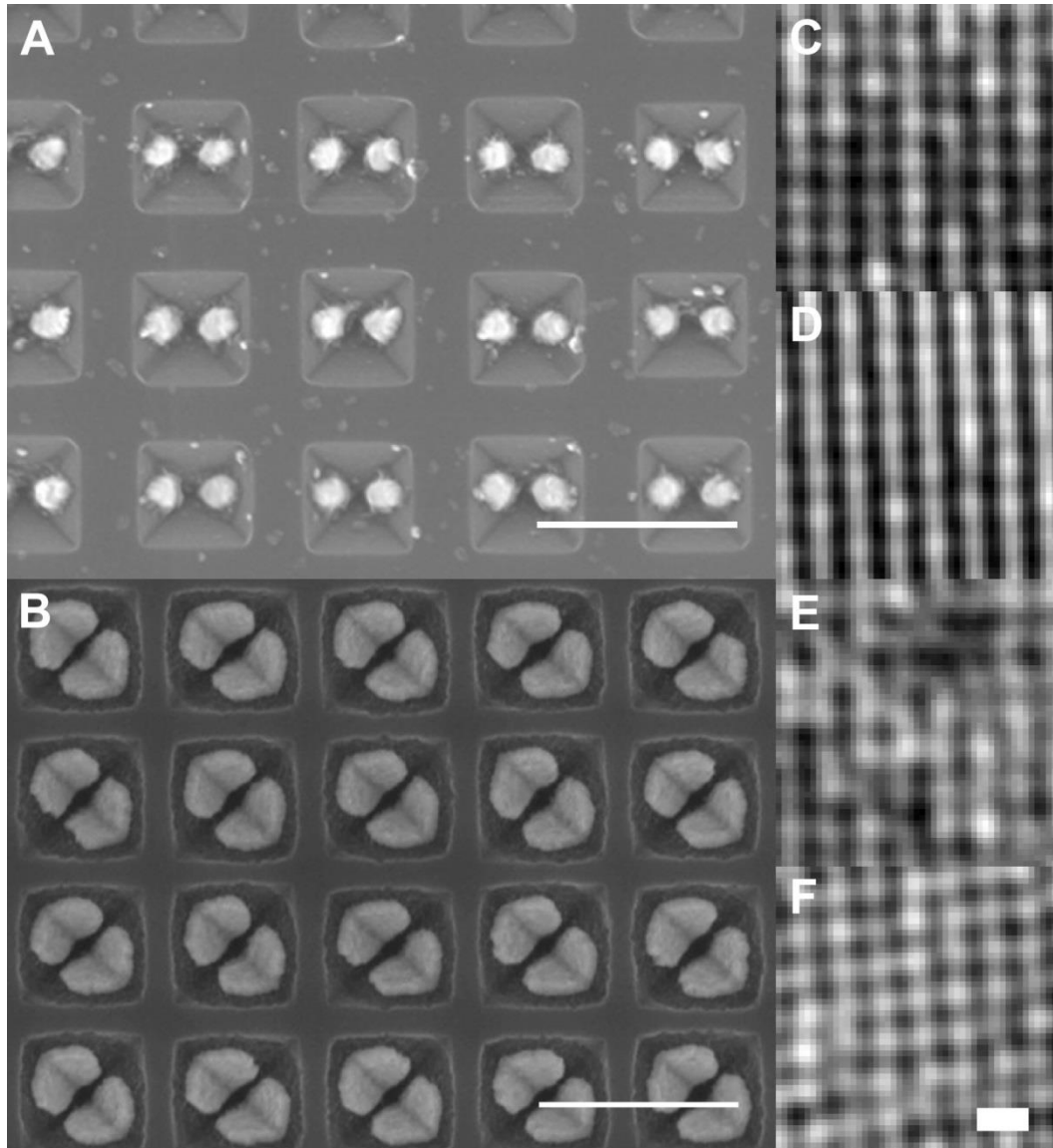


**Figure 5.** SEM and rDIC images of nanostructures fabricated in silicon wafer templates. A SEM of nanoparticle dimers within the template (A) and SEM of bowtie nanostructures in the template (B). rDIC image of empty template (C), nanoparticle dimers (D), bowtie nanostructures (E), and nano-pyramids (F). rDIC images are the sum of 20 images taken with 50 ms exposure. All scale bars represent 500 nm.

## CHAPTER 6: GENERAL CONCLUSIONS

The work presented within centers upon optical microscopy technique development for single-particle tracking using TIRF and TIRS microscopy. The construction of a benchtop reflected-mode DIC microscope was also described along with its advantages regarding plasmonic nanostructure studies.

First, a new type of imaging probe called “non-blinking” quantum dots (NBQDs) were implemented into 3D single-particle tracking under a SA-TIRF microscope. While there currently is no perfect imaging probe, NBQDs provide much more stable fluorescence signals compared to both organic dyes and traditional quantum dots.

The SA-TIRF microscope configuration has significant advantages when localizing fluorescent probes. For one, TIRF techniques provide a significant signal-to-noise ratio improvement compared to other techniques for studying system near surfaces. Also, when studying stationary probes, the evanescent field can be adjusted with such precision that the axial position of the probes can be determined with sub-10-nm accuracy. Lastly, when studying dynamic systems the evanescent field can be adjusted to accentuate the change in fluorescence intensity, making it easier to resolve motion in all three dimensions.

To dynamically track both position and orientation, a technique utilizing TIRS microscopy applied AuNRs as three-dimensional orientation probes. AuNRs have the advantage of being anisotropic dipole emitters giving them a directional component. AuNRs also do not succumb to fluorescence bleaching or intermittency while being easy to functionalize. Instead of using image-recognition methods within either DIC patterns or defocused scattering, the intensity of localized surface plasmon resonance along the short and long axis was translated into in-plane and out-of-plane particle orientation angles, respectively. Assuming the individual particles will achieve both maximum and minimum in-plane and out-of-plane angles during the observation period, we can dynamically track the 3D motions of many surface bound particles.

While the previous TIRS microscopy technique works well for particles with a high degree of mobility, it cannot decipher any orientation information for static nanoparticles. With that in mind, Chapter 4 describes a technique to determine the out-of-plane orientation using TIRS microscopy. By rotating the incoming polarization direction relative to the substrate plane at a wavelength corresponding to the SPR wavelength of the particles, we were able to calculate



the out-of-plane angle by fitting the data with simulations. The technique is simple to administer and can determine the orientation of all particles in the observation area given enough lateral separation. While this approach can be sped up, it is not ideal for dynamic systems.

Finally, the design of a laser-illuminated Nomarski differential interference contrast microscope in reflected mode is described. The system provides a convenient way to study the optical properties of nanoparticles and nanostructures synthesized on reflective substrates such as silicon wafers. The system is adaptable to the addition of extra laser lines through the use of dichroic mirrors, and is adaptable for dual-modality imaging.

While there is currently no system that can divulge all the optical and orientation information for all types of imaging probes, this thesis has given examples of four techniques capable of determining combinations of position, orientation, and optical properties for various probes in unique environments.

### **Future Work**

TIRS microscopy has proven itself to be an excellent technique to track the movement and orientation of metallic nanoparticles, but there are still a few limitations that need to be overcome. Determining the polar angle of static gold nanorods by rotating the incoming polarization is done by fitting a simulated curve the data. The precision of the polar angle determination is partially dependent on the in-plane orientation of the particle. By directing a second beam to be rotated perpendicular to the first beam, by the addition of a pyramidal prism, or by rotating the sample by  $90^\circ$ , the precision of the angle determination can be increased for both focused and defocused imaging.

The ability of the polarization rotation under TIRS microscopy to identify single particles compared to aggregates, or multiple particles within the diffraction limited area, has exciting potential with regard to particle mapping and self-assembly. Utilizing the ability to control the depth of the evanescent field and the combination of s-pol and p-pol light, it may be possible to isolate particles from each other and determine their individual orientations.

The super-localization accuracy of gold nanorods while simultaneously tracking the 3D orientation under TIRS microscopy fluctuates depending on the orientation of the nanorod. To compensate for this, a third laser line can be added to track on the position of the particle. Using non- or circularly-polarized light split into orthogonal sample illumination the nanorod will

deliver a consistent scattering signal regardless of the orientation. The signal can be separated by a dichroic mirror and sent to a separate camera.

Many lab-on-chip devices investigate nanomotors and nanomachines. Reflective DIC is an ideal way to study the movement and interaction of nanomotors and nanomachines within engineered environments. The use of dichroic mirrors allows for the simple “stacking” of additional laser lines that can be used to monitor and track different aspects of the environment. Other dynamic phenomena such as particle self-assembly or structure stability can also be monitored.

Due to the reflective nature of the substrate and the potential interference generated from the substrate, reflective DIC microscopy may have useful ways for determining axial position in much the same way as fluorescence interference contrast (FLIC) microscopy. This phenomenon could be used to add another aspect of optical tomography to the DIC microscope.

In addition to particle and structure studies, the microscope is adaptable to working in the ultra-violet (UV) range of the electromagnetic spectrum. A laser, LED, or lamp source can be adapted to produce the needed illumination. Many organic molecules absorb in the UV making it an ideal way to study polymer materials in dynamic processes such as self-assembly or structure transitions. Using shorter wavelengths of light also increases the lateral resolution, enabling UV-rDIC to be a possible alternative to techniques such as TEM and SEM for characterizing polymer films.

## ACKNOWLEDGEMENTS

There are a great many people who deserve a great deal of thanks, but first on my list is my major advisor Prof. Ning Fang. Prof. Fang took me into his research group as part of his first official class of graduate students at Iowa State. There is an extra level of understanding that goes into accepting a position with a new faculty member, and I appreciate the level of trust Prof. Fang placed in me to work hard and produce results during such a fast-paced part of his career. Dr. Fang managed to allow me the freedom in the lab to both prove myself right on an idea, but also equal in value, to prove myself wrong. It has been extremely enjoyable to be a part of his lab and to share ideas and results with him over the years.

I'd like to thank my Program of Study Committee; Dr. Javier Vela, Dr. Emily Smith, Dr. R.S. Houk, and Dr. Edward Yu, first, for passing me during my preliminary oral examination. Without which, quite literally, (almost) none of this would have happened. Secondly, throughout the years they were all quite approachable for any of my questions and helpful in many other ways. Dr. Yu allowed me into his lab to express and purify the kinesin protein many times while trying to complete the NBQD super-localization project. Dr. Houk lectured a valuable class from which I applied much of the knowledge learned during those early mornings and he managed to return a favor by (only briefly) napping during my prelim. Dr. Smith also lectured an indispensable class on instrumentation that I will continually pull from throughout my career. She also was gracious enough to lend various equipment and optics from her lab over the years that made life significantly easier. Lastly, Dr. Vela was like a second advisor offering up many insights into the projects on hand and into the larger picture of life after graduate school.

Members of the Fang research group also deserve many thanks. I thank my classmates Yan Gu and Anthony Stender for being a bit of a support group as we jumped into being part of Ning's first official class of students. Both Yan and Anthony are easy to work with and are always willing to offer insight or a new perspective on a project. I wish them the best on their future endeavors. Former group members Dr. Wei Sun and Dr. Gufeng Wang were indispensable in dispensing their knowledge, without which early lab life would have seemed infinitely more complex. I want to thank all the current group members; Rui Han, Ji Won Ha, Ashley Augspurger, Bin Dong, Kuangcai Chen, Amanda Nguy, and Nick Bormann who have all made it easier to get up in the morning and walk into the lab. Without everyone's endearing personalities, these years may truly have felt like a grind.

My science friends, of whom we have shared many gripes and triumphs, also deserve some thanks. It would have been lonely drinking all those beers by myself. Let's do it again sometime.

Finally, I'd like to thank my family. Though I'm sure it was no easy task, they managed to instill in me the value of hard work, education, and free-thought. Without any of these I would not have come as far as I have. For these, and many other reasons, I am always grateful.

This work was performed at the Ames Laboratory under contract number DE-AC02-07CH11358 with the U.S. Department of Energy. The document number assigned to this thesis/dissertation is IS-T 3095.